SpringerBriefs in Applied Sciences and Technology

Nonlinear Circuits

SpringerBriefs in Nonlinear Circuits promotes and expedites the dissemination of substantive new research results, state-of-the-art subject reviews and tutorial overviews in nonlinear circuits theory, design, and implementation with particular emphasis on innovative applications and devices. The subject focus is on nonlinear technology and nonlinear electronics engineering. These concise summaries of 50–125 pages will include cutting-edge research, analytical methods, advanced modelling techniques and practical applications. Coverage will extend to all theoretical and applied aspects of the field, including traditional nonlinear electronic circuit dynamics from modelling and design to their implementation.

Topics include but are not limited to:

- nonlinear electronic circuits dynamics;
- Oscillators;
- cellular nonlinear networks;
- arrays of nonlinear circuits;
- chaotic circuits;
- system bifurcation;
- chaos control;
- active use of chaos;
- nonlinear electronic devices;
- memristors;
- circuit for nonlinear signal processing;
- wave generation and shaping;
- nonlinear actuators;
- nonlinear sensors;
- power electronic circuits;
- nonlinear circuits in motion control;
- nonlinear active vibrations;
- educational experiences in nonlinear circuits;
- nonlinear materials for nonlinear circuits; and
- nonlinear electronic instrumentation.

Contributions to the series can be made by submitting a proposal to the responsible Springer contact, Oliver Jackson (oliver.jackson@springer.com) or one of the Academic Series Editors, Professor Luigi Fortuna (luigi.fortuna@dieei.unict.it) and Professor Guanrong Chen (eegchen@cityu.edu.hk).

More information about this series at http://www.springer.com/series/15574

Debabrata Biswas · Tanmoy Banerjee

Time-Delayed Chaotic Dynamical Systems

From Theory to Electronic Experiment

Springer

Debabrata Biswas
Department of Physics
The University of Burdwan
Burdwan, West Bengal
India

Tanmoy Banerjee
Department of Physics
The University of Burdwan
Burdwan, West Bengal
India

ISSN 2191-530X ISSN 2191-5318 (electronic)
SpringerBriefs in Applied Sciences and Technology
ISSN 2520-1433 ISSN 2520-1441 (electronic)
SpringerBriefs in Nonlinear Circuits
ISBN 978-3-319-70992-5 ISBN 978-3-319-70993-2 (eBook)
https://doi.org/10.1007/978-3-319-70993-2

Library of Congress Control Number: 2017958604

LabVIEW™ is a trademark of National Instruments Corporation, 11500 N Mopac Expwy, Austin, TX 78759-3504, USA, http://www.ni.com/

© The Author(s) 2018
This work is subject to copyright. All rights are reserved by the Publisher, whether the whole or part of the material is concerned, specifically the rights of translation, reprinting, reuse of illustrations, recitation, broadcasting, reproduction on microfilms or in any other physical way, and transmission or information storage and retrieval, electronic adaptation, computer software, or by similar or dissimilar methodology now known or hereafter developed.
The use of general descriptive names, registered names, trademarks, service marks, etc. in this publication does not imply, even in the absence of a specific statement, that such names are exempt from the relevant protective laws and regulations and therefore free for general use.
The publisher, the authors and the editors are safe to assume that the advice and information in this book are believed to be true and accurate at the date of publication. Neither the publisher nor the authors or the editors give a warranty, express or implied, with respect to the material contained herein or for any errors or omissions that may have been made. The publisher remains neutral with regard to jurisdictional claims in published maps and institutional affiliations.

Printed on acid-free paper

This Springer imprint is published by Springer Nature
The registered company is Springer International Publishing AG
The registered company address is: Gewerbestrasse 11, 6330 Cham, Switzerland

Debabrata Biswas: To my Parents.

Tanmoy Banerjee: To my teacher,
Professor Bishnu Charan Sarkar,
a fascinating teacher,
a thoughtful researcher,
and a wonderful human being.

Preface

Time delays are omnipresent in nature. Delays arise in various natural and man-made systems due to the finite speed of signal propagation, finite response time, and switching speed. The presence of time delay in a dynamical system makes it infinite dimensional and if the system is nonlinear it may give rise to many interesting phenomena, like bifurcation, chaos, and multistability. Many of the natural phenomena, such as blood production in patients with leukemia (the well known Mackey–Glass model), optical systems (e.g., the Ikeda system), El Niño or southern oscillation (ENSO), population dynamics, and neural networks have been successfully modeled by considering time delay in their dynamics. Although a large number of time-delayed systems are reported in the literature where delay differential equations are used for mathematical modeling, only a few practical implementations of those systems are reported. A systematic *wishful* design of chaotic time-delayed system is important from the fundamental interest—these systems can contribute to improve our understanding of the intricate and subtle dynamical behaviors of isolated time-delayed systems, subsequently, it also offers an excellent opportunity for the researchers to explore the collective behaviors of coupled time-delayed systems under natural experimental setups. Also, from the application point of view, these studies can be extended to exploit chaotic time-delayed system in several engineering applications.

Motivated by the above-mentioned reasons, in this book, we describe a systematic design principle of chaotic time-delayed dynamical systems and discuss their collective behaviors, such as synchronization and oscillation suppression. We describe how a proper choice of nonlinearity leads to chaos and hyperchaos even in a first-order time-delayed system. The occurrence of chaos and the efficacy of the considered design techniques are supported by rigorous theoretical studies, numerical characterization, and experimental demonstrations with electronic circuits. To extend our knowledge of nonlinear time-delayed system, we study the coupled dynamics of these systems and report some novel collective phenomena related to synchronization and oscillation suppression. This book actually provides a *bridge* between two broad topics, namely the design technique of chaotic time-delayed systems and the collective phenomena shown by these systems when coupled with each other through a proper physical coupling scheme.

Apart from rigorous theory and experiments, for an entry level researcher, we also provide two brief, yet effective, tutorials on the numerical package XPPAUT and the experimental technique of data acquisition through LabVIEW.

Acknowledgements: We convey our sincere thanks to Prof. Syamal K. Dana for insisting us to write this book. It is his constant encouragement that makes this book possible. We are indebted to Prof. B. C. Sarkar for his insightful suggestions and comments on several topics covered in this book. We also acknowledge the support from our group members of the *Chaos and Complex Systems Research Laboratory*, Department of Physics, University of Burdwan. We thankfully acknowledge the American Institute of Physics (AIP) and Springer Science for providing permissions to reuse our published works. We also acknowledge World Scientific Publishing for allowing us to use some of the figures and results from one of our previous publications. Thanks are also due to Mr. Oliver Jackson, Editor (Engineering), Springer, for his constant input to improve the quality of this book. Finally, we are grateful to our family members for their sacrifice, constant support, and encouragement.

Burdwan, India
July 2017

Debabrata Biswas
Tanmoy Banerjee

Contents

Chapter 1
Introduction

For the last few decades, much emphasis has been imposed on exploring the dynamics of systems having intrinsic time delays. Time delays are ubiquitous in nature and have been considered in various fields including physics, biology, mathematics, engineering, and ecology [7, 70]. A plethora of natural and man-made systems have inherent time delay and are mathematically modeled by delay differential equations (DDEs); examples include blood production in patients with leukemia [79] (Mackey–Glass model), optical bistable resonator (Ikeda system) [56], population dynamics [150], physiology [94], El Niño/southern oscillation (ENSO) [22], neural networks [76], and control systems [101, 114]. An ever-increasing attention toward the time-delayed dynamical systems can be attributed to the following facts:

(i) Time delay arises inherently in natural and artificial systems due to finite signal transmission times, limited switching speeds, and memory effects.
(ii) The presence of time delay in a dynamical system makes the system infinite dimensional and may lead to instability and oscillatory behavior [70]. Further, time delay in nonlinear dynamical systems may give rise to various complex phenomena, like bifurcation, chaos and hyperchaos, and multistability.
(iii) Coupled nonlinear time-delayed systems often show novel behaviors like synchronization [96], amplitude death [104], and chimera states [91, 113], understanding of which is important both from the fundamental and the application point of view. Since in most of the physical systems we are dealing with the coupled time-delayed oscillators, therefore, collective behavior of coupled time-delayed systems deserves systematic studies.
(iv) Infinite dimensionality of time-delayed systems offers a great opportunity to the researchers to harness the richness of hyperchaos. As a simple time-delayed system with suitable nonlinearity can produce a hyperchaotic signal with a large number of positive Lyapunov exponents, thus they have been identified as good

D. Biswas and T. Banerjee, *Time-Delayed Chaotic Dynamical Systems*, SpringerBriefs in Nonlinear Circuits,
https://doi.org/10.1007/978-3-319-70993-2_1

candidates for secure communication systems [68, 98]. Apart from communication systems, chaotic and hyperchaotic circuits have important applications in chaos-based noise generators [5], improvement of sensors [40] and of motion capabilities in robotics [25], etc. For these reasons, efforts are on to design *simple* and *well-characterized* time-delayed systems that can produce chaos and hyperchaos [128, 139, 153].

Although a large number time-delayed systems have been reported in the literature where DDEs are used to mathematically model the systems, only a few practical implementations of those systems are reported. This is because of the fact that most of the systems are not wishfully designed for electronic circuit implementation but originally they were proposed for mathematically model a particular natural phenomenon. For example, the first and most studied nonlinear time-delayed system, the Mackey–Glass (MG) system [79], was originally proposed in 1977 to model the blood production in patients with leukemia; since then, the MG system has become the test bench for studying the dynamics of nonlinear time-delayed system. However, the first successful experimental electronic implementation of the MG system was reported 17 years later, in 1995 [89]. This long waiting time can be attributed to the fact that the nonlinearity in the MG system has a closed-form mathematical function that has a specific bimodal (one-humped) form, which is difficult to emulate in electronic circuit. Similar arguments also apply for one more popular nonlinear time-delayed system, namely the Ikeda system [56].

Later on, researchers tried to "wishfully" design nonlinear time-delayed systems that are easy to implement in electronic circuit. In this context, several nonlinear time-delayed electronic circuits and systems have been reported in the literature [26, 77, 78, 87, 134–136, 145]. However, all the systems and circuits suffer from a common problem, which is, in all those systems, the piecewise linear (PWL) nonlinearity was used, which leads to approximate analysis and circuit design of the original system. Further, an exact analysis of those circuits needs a describing function representation for the nonlinearity that makes the analysis difficult [26]. Therefore, the search for a delay dynamical system with a nonlinearity having a closed-form mathematical function, and at the same time, that can be implemented easily with electronic circuits is important and deserves a systematic study.

Apart from the design issue, the next important problem is to study the collective behavior of nonlinear time-delayed systems. The two most important cooperative phenomena in the context of coupled oscillators are synchronization [96] and oscillation suppression [63]. Despite a large amount of studies have been reported on these topics in non-delayed dynamical systems, research on the collective behavior of time-delayed chaotic systems is relatively less explored. Moreover, the discovery of new collective behaviors, like the *chimera* state [91, 113] has revitalized the research on the cooperative phenomena in coupled oscillators in general.

1.1 Time-Delayed Dynamical Systems

At first we describe a functional differential equation (FDE) [61] as

$$\dot{x}(t) = f\big(t, x(t+\hat{s})\big), \quad -\tau < \hat{s} < 0, \tag{1.1}$$

where $\big(f : \mathscr{R} \times Q[-\tau, 0] \to \mathscr{R}^n\big)$. The FDEs are generalization of ordinary differential equations (ODEs) of the form

$$\dot{x}(t) = g\big(t, x(t)\big), \tag{1.2}$$

with $\big(g : \mathscr{R} \times \mathscr{R}^n \to \mathscr{R}^n\big)$, if at time t the velocity $\dot{x}(t)$ of a process depends on both the current state $x(t) \in \mathscr{R}^n$ and on the pre-history $x(t+s)$, $-\tau < s < 0$. The delay differential equations (DDEs) are a class of FDEs, whose general form is given by [73]

$$\dot{x}(t) = f\big(t, x(t), x(t-\tau_i), \mu\big), \tag{1.3}$$

where $\tau_i \in \mathscr{R}^+$ are all positive constants, called the delay time and $\mu \in \mathscr{R}$. This is an example of a class of the DDE. The right-hand side of the above equation depends on the history of the system for some range of the past. For the case of finite-dimensional system, a finite number of initial conditions are required to solve the equation. On the other hand for the case of DDEs, one requires the initial conditions at each point of the delay line back to $t = -\tau$ from $t = 0$. Since a straight line, whatever be its length, may be considered as a collection of infinite number of points, hence, in the case of DDEs one requires infinite number of initial conditions. Thus, it may be said that, instead of initial conditions, one requires *initial function* to solve a DDE. This initial function actually determines the characteristics of the system prior to $t = 0$. For systems with multiple delays, the initial function must cover the range of the largest delay, i.e., $\max\{\tau_i\}$.

To have better understanding, we consider the following form of DDE:

$$\dot{x}(t) = f\big(x(t), x(t-\tau)\big). \tag{1.4}$$

Here, the initial function $x(t)|_{init} \equiv \varphi_x$ (say) must be defined in the range $-\tau \leq t \leq 0$. If the initial function be like this, then the history of the system for the largest delay ($\max\{\tau_i\}$) can be incorporated in the solution [110].

Depending upon the occurrence of delay, there are mainly three types of delay differential equations, namely

(i) Retarded or Lag delay differential equation,
(ii) Neutral delay differential equation, and
(iii) Future delay differential equation.

The following are the simplified generic forms:

(i) The *retarded* or *lag* delay differential equations:

$$\frac{dx(t)}{dt} = f\Big(x(t), x(t-\tau_i)\Big), \tag{1.5}$$

(ii) The *neutral* delay differential equations:

$$\frac{dx(t-\tau_i)}{dt} = f\Big(x(t), x(t+\tau_i)\Big), \tag{1.6}$$

(iii) The *future* delay differential equations:

$$\frac{dx(t)}{dt} = f\Big(x(t), x(t+\tau_i)\Big), \tag{1.7}$$

where $i = 1, 2, 3, \ldots, n$. We shall consider the retarded type of delay differential equation (Eq. (1.5)) throughout the book.

Depending upon the nature of the delay(s) involved in the DDEs, the DDEs can be grouped as (i) DDEs having a *single discrete delay*, (ii) DDEs having *multiple discrete delays*, (iii) DDEs having *distributed delays*, (iv) DDEs having *state-dependent delays*, and (v) DDEs having *time-dependent delays*. In the following, we give a brief account of all types of delay differential equations.

1.1.1 Delay Differential Equations with Single Discrete Delay

DDEs having only one delay (also constant in this case) can be given in general as follows:

$$\dot{x} = f\big(t, x(t), x(t-\tau)\big), \tag{1.8}$$

where the symbols have their usual meaning as stated formerly. This type of system arises in many cases including biology [79], optics [56], economics [133], and ecology [39].

1.1.2 Delay Differential Equations with Multiple Discrete Delays

DDEs having multiple discrete delays are represented by the following equation:

$$\dot{x} = f\big(t, x(t), x(t-\tau_i)\big), \tag{1.9}$$

where $i = 0, 1, 2, \ldots, n$ are integers.

In case of *discrete-time* systems, the equation becomes [129]

$$x(k+1) = A_0 x(t) + \sum_{j=1}^{N} A_j x(k - \tau_j), \tag{1.10}$$

where $0 < \tau_1 < \tau_2 \cdots < \tau_N$. It is seen from Eqs. (1.9) and (1.10) that the multiple discrete time-delayed systems possess many delay terms in its representative equation. The delays play important role in the systems. The appearance of multiple discrete delays is a common fact in the biological systems [24, 111, 126], control systems [31, 50, 109, 129], population dynamics [65], economics [6, 58], etc.

1.1.3 Delay Differential Equations with Distributed Delays

There may arise the case where the delay is not a fixed quantity but it has some functional behavior. This type of delay comes in many systems like physiology, population dynamics, and engineering [86]. The general form of the systems having distributed delay (retarded type) is as follows:

$$\dot{x} = f\left(t, x(t), \int_0^{\infty} g(\tau) x(t-\tau) d\tau\right), \tag{1.11}$$

where $g(\tau)$ is a function of τ.

1.1.4 Delay Differential Equations with State-Dependent Delay

For the study of some realistic models, it is necessary to take the delay as a function of the time as well as the state itself [52]. The system is delayed in time with certain functional relationships upon the state of the system. Reference [75] studied one such state-dependent delay equation. The equation is given by

$$\frac{dx}{dt} = f\Big(t, x\big(t - \tau\big(t, x(t)\big)\big)\Big). \tag{1.12}$$

It may be noted from the above equation that the delay term depends on the state of the system (i.e., τ is a function of $x(t)$). The main application of the state-dependent delay arises in the population growth model [75] and some evidences may be found in Ref. [80], where the milling process is considered.

1.1.5 *Delay Differential Equations with Time-Dependent Delay*

The general form of the time-dependent (time-varying) delay differential equation is given by

$$\frac{dx}{dt} = f\Big(t, \mu, x\big(t - \tau(t)\big)\Big), \tag{1.13}$$

where f is a function and p is any parameter. It may be noted that the delay term depends explicitly on time.

1.2 A Brief Survey on Nonlinear Time-Delayed Systems

In this section, we provide a brief and sketchy review on the research on nonlinear intrinsic time-delayed systems. Our review is based on the three broad categories, namely (i) Models with intrinsic time delay, (ii) Time-delayed electronic circuits, and (iii) Synchronization of time-delayed systems.

1.2.1 *Models with Time Delay*

Here, we discuss a few important models (without claiming to be complete), which are widely studied in the literature. The modeling of an important physiological control system was reported by Mackey and Glass [79]. In the paper, "*Oscillation and chaos in physiological control system*", the authors considered delay differential equation with polynomial nonlinearity to model two diseases. First, they consider a respiratory disease, whose dynamics is explained by a DDE. Second, the dynamics of chronic granulocytic leukemia (CGL), which occurs due to the delay between the initiation of cellular production in the bone marrow and release of mature cells into the blood; if this delay increases, the population of mature circulating cells oscillates chaotically and the case is called "leukemia". The next milestone in this field is the Ikeda system [56, 57]. The study of the system revealed that, depending upon the intensity of incident light, the transmitted light in a ring cavity containing nonlinear dielectric medium may lose stability and as a result, periodic or non-periodic states emerge. The nonlinearity involved in the Ikeda system is $\sin(\cdot)$ (sinusoidal)-type nonlinearity. Later, another physiological model is given by Villasana et al. [140], who used DDE to present a competition model of tumor growth that includes the immune system response and a cycle-phase-specific term. The oceanographic model is reported by Boutle et al. [22]. The authors successfully used the delayed-action oscillator to model the effect of El Niño. They discussed the topics such as the influence of the annual cycle, global warming, stochastic influences due to weather conditions and off-equatorial heat sinks, etc., using this delayed model. Next important work in this field is due to Yongzhen et al. [150]. In the paper, they considered the delay model of predator–prey with parasitic infection. The effect of parasitic infection on prey is modeled through the delay differential equation. This is an eco-epidemic system. The physiological model of artificial pancreas with time-delayed insulin secretion effect is considered by Pei et al. [94]. They showed that, depending upon the insulin secretion delay, the system may show double Hopf bifurcation for a smaller technological delay. A number of important works on time-delayed neural model may be found in Refs. [28, 41, 74, 142]. Another important application of the time-delayed systems is in the control systems. Several works on the control system with time delay may be found in Refs. [8, 30, 88, 99, 101, 114] and references therein.

1.2.2 Time-Delayed Electronic Circuits

The first breakthrough in time-delayed chaotic electronic circuit was due to Namajũnas et al. [89] in 1995. In the paper, entitled "*An electronic analog of Mackey-Glass system*", they implemented the time-delayed system that is topologically equivalent to that of the Mackey–Glass system [89]. They implemented the nonlinearity of the system by coupling two complementary junction field-effect transistors (JFETs). The delay part was implemented using the LCL filter sections.

Later, Lu and He [77, 78] reported a time-delayed chaotic system with a proper piecewise linear (PWL) nonlinearity and LCL delay blocks. Tamaševičius et al. [134] reported a time-delayed system with a PWL nonlinearity. In Ref. [143], Wang et al. reported a time-delayed chaotic circuit which consists of PWL nonlinearity and LCL delay blocks. Tamaševičius et al. [135] considered an inverted N-shaped nonlinearity, which is realized by a circuit with a PWL nonlinearity. Later on in the same year, Yalçin and Özoguz [145] reported another time-delayed electronic circuit that is able to show n-scroll chaotic attractors. Kilinç et al. [60] considered time-delayed system which contains the hysteresis function as the nonlinearity. The system showed n-scroll chaotic attractor. Voss [141] proposed a time-delayed chaotic circuit that contains the bucket-brigade device (BBD) digital delay block. This type of BBD delay was used later in Refs. [4, 102]. Later, Buscarino et al. [27] designed a time-delayed chaotic circuit with a PWL nonlinearity using a second-order low-pass Bessel filter as the delay block. Banerjee et al. [13] reported a chaotic time-delayed system using a closed-form mathematical function as the nonlinearity; this nonlinear function is also easy to implement in electronic circuit. Further, they used an active all-pass filter as the delay block, which was used widely later in producing time delay in electronic circuits [1, 97]. Several other multi-scroll [12, 20] and single-scroll [21] hyperchaotic time-delayed systems and their circuit implementations have been reported by the same authors.

1.2.3 Synchronization of Time-Delayed Systems

Although synchronization of chaos was discovered by Pecora and Carrol [93] in 1990, the first study on chaos synchronization in intrinsic time-delayed systems was reported much later (1998) by Pyragas [100]. Pyragas considered Mackey–Glass (MG) systems under the unidirectional coupling scheme and showed that the coupled systems synchronize under certain coupling conditions. Later, Pyragas [98] reported secure communication exploiting synchronization of time-delayed systems. Yalçin et al. [146] reported the synchronization in master–slave configuration in Lur'e system with time delay. Masoller et al. [82–84] showed the anticipating synchronization of coupled time-delayed systems. Shahverdiev et al. [123] reported the lag synchronization in delay-coupled intrinsic time-delayed systems. Multiple time-delayed system synchronization was also reported by Sahaverdiev [122].

Synchronization in linearly coupled time-delayed system was reported by Chen et al. [29]. Yu [151] reported the global synchronization of chaotic time-delayed systems coupled in bidirectional coupling scheme. Han et al. [53] studied the effect of parameter mismatch on anticipating synchronization of chaotic systems with time delay in the framework of the master–slave configuration. Senthilkumar et al. [118] studied the inverse synchronization in coupled time-delayed systems. They showed the system to experience inverse anticipatory, inverse complete, and inverse lag synchronization. Projective synchronization in multiple time-delayed Rössler system is reported in [45]. Senthilkumar et al. [119, 120] showed the phase synchronization and transition from phase synchronization to complete synchronization in time-delayed systems with nonlinear time delay coupling. Synchronization in time-delayed systems mediated by a common noise was reported in Ref. [117]. Ghosh et al. [46, 48] reported the generalized synchronization and design of coupling for obtaining desired synchronization in time-delayed systems. Yao et al. [149] reported the role of time delay coupling in the time-delayed system coupled through repulsive coupling scheme. Refs. [131, 132] reported the global phase synchronization in an array of coupled time-delayed system. Synchronization through environmental coupling in hyperchaotic time-delayed systems and their experimental observations was reported by Banerjee and Biswas [11]. Also, the authors discovered a new synchronization transition route to amplitude death in chaotic time-delayed systems [10].

1.3 Topics Covered in This Book

In this book, we cover the following two broad issues related with the chaotic time-delayed systems:

First, we provide a systematic procedure to design time-delayed chaotic oscillators whose nonlinearity is expressed in terms of a closed-form mathematical function, and at the same time, that is easy to implement in hardware level using off-the-shelf electronic circuit elements. Then, we characterize the system *analytically* and numerically. Finally, we describe the detailed experimental implementation of the system in electronic circuit.

Second, as a natural extension, we discuss the collective behavior of the proposed chaotic time-delayed systems and circuits. Under collective behaviors, we first discuss the synchronization phenomena of the coupled time-delayed systems and then discuss another collective behavior, namely oscillation quenching state and the associated transitions. Apart from theoretical and numerical analyses, we verify all the collective behaviors through electronic circuit level experiments: it is an important step as it provides a useful mean of understanding collective behaviors of time-delayed systems in the real-world situation, i.e., in the presence of noise, parameter mismatch, and fluctuations.

Chapter 2
First-Order Time-Delayed Chaotic Systems: Design and Experiment

In this chapter, we discuss the design principle of chaotic time-delayed systems with (i) a bimodal nonlinearity and (ii) an unimodal nonlinearity. Both the nonlinearities are represented by *closed-form mathematical functions* (unlike PWL nonlinearity). We carry out rigorous stability analysis to identify the Hopf bifurcation through which limit cycle oscillations are born. Next, we simulate the system models numerically to show that with the variation of delay and other system parameters, the systems show chaos. Complexity of the systems is characterized by Lyapunov exponents and Kaplan–Yorke dimension. Finally, we discuss in detail how both the systems can be implemented in experiment using electronic circuits.

2.1 Chaotic Time-Delayed System with Bimodal Nonlinearity: System Description

We consider the following first-order nonlinear retarded-type delay differential equation with a single constant scalar delay

$$\dot{x}(t) = -ax(t) + bf(x_\tau), \tag{2.1}$$

where $a > 0$ and b are system parameters. Also, $x_\tau \equiv x(t-\tau)$, where $\tau \in \mathscr{R}^+$ is a constant time delay. Now, we define the following closed-form mathematical function for the nonlinearity:

$$f(x_\tau) = -nx_\tau + m\tanh(lx_\tau), \tag{2.2}$$

where n, m, and l are all positive system parameters and they are restricted by the following constraint $n < ml$ to maintain the bimodal nature of the nonlinearity. It can be seen that the nonlinear function is constituted by the weighted superposition

D. Biswas and T. Banerjee, *Time-Delayed Chaotic Dynamical Systems*, SpringerBriefs in Nonlinear Circuits,
https://doi.org/10.1007/978-3-319-70993-2_2

Fig. 2.1 Nonlinearity with the function $f(x_\tau) = -nx_\tau + m\tanh(lx_\tau)$ with "N1": $n = 2.2$, $m = 1$, $l = 10$; "N2": $n = 3$, $m = 1$, $l = 8$, "N3": $n = 1.5$, $m = 1.2$, $l = 8$. Dashed curve is for $n = 4$, $m = 1$, $l = 3$, which shows that for $n > ml$ the nonlinearity does not show the bimodal nature

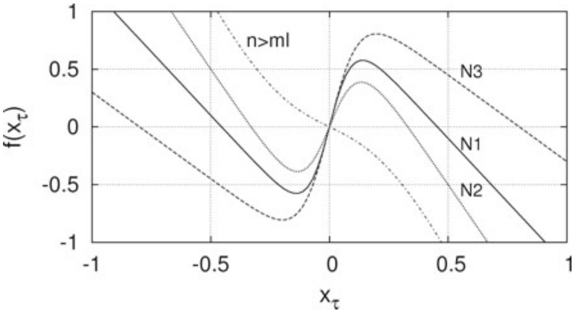

of two functions, namely the linear proportionality function and the nonlinear $\tanh(\cdot)$ function. Further, $f(x_\tau)$ is an odd-symmetric function, i.e., $f(-x_\tau) = -f(x_\tau)$.

Figure 2.1 shows the nature of the nonlinearity produced by $f(x_\tau)$ for different values of n, m, and l. The nonlinearity shows a hump in the first and the third quadrants. The condition $n < ml$ ensures this bimodal nature of the nonlinear function. Tamaševičius et al. [135] used almost similar form of the nonlinearity with piecewise linear (PWL) function; but unlike their system, here Eq. (2.2) has a closed-form mathematical function that does not show sharp corners in the turning points. The nonlinear functions of Fig. 2.1 shows that positive slope continuously changes to the negative slope through a zero slope region. The PWL function is unable to represent this behavior. Also, in the electronic circuit experiment, it is hard to realize a sharp transition from positive to negative slope due to the nonideal characteristics of the practical circuit components (see e.g., [135]). Therefore, the closed-form mathematical model of the nonlinearity used here is suitable for the electronic circuit implementation. Also, Eq. (2.2) provides a large number of choices of n, m, and l for which the bimodal nature will be preserved. Further, Ref. [135] considered only positive values of b, but here we consider both positive and negative values of b.

2.2 Stability and Bifurcation Analysis

2.2.1 *Positive* b

The stability of the system is analyzed by rewriting Eq. (2.1) in the following form:

$$\dot{x} = g\big(x(t), x_\tau\big) = -ax(t) + bf(x_\tau). \tag{2.3}$$

The equilibrium condition implies $\dot{x} = 0$ and $x(t) = x_\tau = x^*$ (say), i.e., $g(x^*, x^*) = -ax^* + bf(x^*) = 0$, which gives

$$\tanh(lx^*) = \frac{a + nb}{mb}x^*. \tag{2.4}$$

Close inspection reveals that Eq. (2.4) has a fixed point $x^* = 0$ for $l \leq \frac{a+nb}{mb}$, i.e., we have a single trivial fixed point at $x^* = 0$ for

$$b \leq \frac{a}{-n+ml}. \tag{2.5}$$

For $b > \frac{a}{-n+ml}$, Eq. (2.4) has three fixed points, namely $x^* = (-p1, 0, p1)$. Here, $\pm p1$ are the nontrivial fixed points whose values are determined by the system parameters.

Let us now examine the stability of each fixed point. From Eq. (2.3), one gets

$$J_0 = \frac{\partial g(x, x_\tau)}{\partial x} = -a, \tag{2.6}$$

and

$$J_\tau\Big|_{x_\tau=x^*} = \frac{\partial g(x, x_\tau)}{\partial x_\tau}\Bigg|_{x_\tau=x^*} = b\big[-n + ml\ \mathrm{sech}^2(lx^*)\big]. \tag{2.7}$$

The *characteristic equation* of the system is given by $J_0 + J_\tau e^{-\lambda\tau} - \lambda = 0$, which gives

$$\lambda = -a + b\big[-n + ml\ \mathrm{sech}^2(lx^*)\big]e^{-\lambda\tau}. \tag{2.8}$$

Stability for $\tau = 0$

For the case of $\tau = 0$, the characteristic equation takes the following form:

$$\lambda = J_0 + J_\tau. \tag{2.9}$$

Taking $\lambda = \mu + i\nu$, and comparing real and imaginary parts in both sides of the above equation, one gets

$$\mu = -a + b\big[-n + ml\ \mathrm{sech}^2(lx^*)\big], \text{ and } \nu = 0. \tag{2.10}$$

Asymptotic stability will occur when all the roots of the characteristic equation have negative real parts (i.e., negative μ); from Eq. (2.10), we get the condition of stability as

$$b\big[-n + ml\ \mathrm{sech}^2(lx^*)\big] < a. \tag{2.11}$$

Equation (2.11) imposes the first condition for choosing the system parameters to achieve asymptotic stability of the system for $\tau = 0$. Let us now examine the case for $x^* = 0$; from Eq. (2.11), we have the condition for stability as $b < -n+ml$, which is interestingly identical with Eq. (2.5). Thus, one can conclude that, for $b < -n+ml$, $x^* = 0$ is the only stable fixed point for any $\tau \geq 0$, but beyond that, $x^* = 0$ becomes unstable through a *supercritical pitchfork bifurcation* and two nontrivial fixed points ($\pm p1$) emerge. Next, we have to examine the stability of the nontrivial fixed points ($\pm p1$).

Stability for $\tau \neq 0$
Hopf bifurcation will appear if at least one of the eigenvalues crosses the imaginary axis from left, and enter the right half plane. Thus, if μ varies from left to right, we can say that $\mu < 0$ represents a stable state, $\mu > 0$ is bifurcated state, and $\mu = 0$ is the bifurcation point. At the emergence of Hopf bifurcation, we assume $\mu = 0$; thus using $\lambda = i\nu$, we get

$$\begin{aligned} J_0 + J_\tau e^{-i\nu\tau} - i\nu = 0, \\ J_0 + J_\tau \cos(\nu\tau) - i\{J_\tau \sin(\nu\tau) + \nu\} = 0. \end{aligned} \tag{2.12}$$

Now equating the real and imaginary parts on both sides of the above equation, we get

$$J_\tau \cos(\nu\tau) = -J_0, \tag{2.13}$$

$$J_\tau \sin(\nu\tau) = -\nu. \tag{2.14}$$

Equations (2.13) and (2.14) lead to give $\nu = \sqrt{J_\tau^2 - J_0^2}$. This is possible only for $|J_\tau| \geq |J_0|$, i.e.,

$$\left|b[-n + ml\ \mathrm{sech}^2(lx^*)]\right| \geq \left|-a\right|. \tag{2.15}$$

Again from Eq. (2.13), we get

$$\nu\tau = \cos^{-1}\left(-\frac{J_0}{J_\tau}\right), \tag{2.16}$$

which leads to

$$\tau_{k1} = \frac{\left[\cos^{-1}\left(-\frac{J_0}{J_\tau}\right) + 2k\pi\right]}{\sqrt{{J_\tau}^2 - {J_0}^2}}, \qquad \text{for } J_\tau < 0, \tag{2.17a}$$

$$\tau_{k2} = \frac{\left[\left\{2\pi - \cos^{-1}\left(-\frac{J_0}{J_\tau}\right)\right\} + 2k\pi\right]}{\sqrt{{J_\tau}^2 - {J_0}^2}}, \quad \text{for } J_\tau > 0, \tag{2.17b}$$

where $k = 0, 1, 2, \ldots$ Now we set $\nu_0 = \sqrt{{J_\tau}^2 - {J_0}^2}$. Let $\lambda_k(\tau) = \mu_k(\tau) + i\nu_k(\tau)$ be a root of Eq. (2.1) near $\tau = \tau_k$ satisfying $\mu_k(\tau_k) = 0$ and $\nu_k(\tau_k) = \nu_0$. We have

$$\lambda = J_0 + J_\tau e^{-\lambda\tau}, \tag{2.18a}$$

$$\lambda = -a + b[-n + ml\ \mathrm{sech}^2(lx^*)]e^{-\lambda\tau}. \tag{2.18b}$$

We put

$$s = b[-n + ml\ \mathrm{sech}^2(lx^*)]. \tag{2.19}$$

Differentiating both sides of Eq. (2.18b) with respect to τ, we get

$$\begin{aligned} \frac{d\lambda}{d\tau} &= se^{-\lambda\tau}\left(-\lambda - \tau\frac{d\lambda}{d\tau}\right), \\ \frac{d\lambda}{d\tau} &= \frac{-\lambda se^{-\lambda\tau}}{1 + \tau se^{-\lambda\tau}}. \end{aligned} \tag{2.20}$$

Again, from equation Eq. (2.19), we have $se^{-\lambda\tau} = \lambda + a$, we put this in the above and get

$$\frac{d\lambda}{d\tau} = \frac{-\lambda(\lambda + a)}{1 + \tau(\lambda + a)}.$$

Now, at $\tau = \tau_k$; $\lambda = i\nu_0$, as $\mu_k(\tau_k) = 0$ there, hence,

$$\left.\frac{d\lambda}{d\tau}\right|_{\tau=\tau_k} = \frac{{\nu_0}^2 - i\nu_0 a}{(1 + \tau a) + i\tau\nu_0}. \tag{2.21}$$

Equating the real parts on both sides, we get

$$\mu'(\tau_k) = \frac{{\nu_0}^2}{(1 + \tau a)^2 + \tau^2\nu_0^2}.$$

Thus,

$$\mu'(\tau_k) > 0. \tag{2.22}$$

For all values of above-mentioned x^*, Eq. (2.22) is valid. So we conclude that the stable state lies between $\tau = 0$ and τ_{01}.

Now, let us investigate the stability of the system for the following parameter set: $a = 1$, $n = 2.2$, $m = 1$, and $l = 10$ (as we have used in "N1" of Fig. 2.1). Figure 2.2 shows the first six stability curves τ_{ki} $(i = 1, 2)$ (Using Eq. (2.17)) in the $b - \tau$ parameter space. In the figure, τ_{k1} and τ_{k2} are represented by solid lines and dotted lines, respectively. Since $\mu'(\tau_k) > 0$ for any $k = 0, 1, 2\ldots$, thus, stability zone cannot be situated between two consecutive τ_{ki} curves. So we conclude that the stable island lies between $\tau = 0$ and τ_{01} curves. The shaded region in the figure represents the stable zone, and τ_{01} curve represents the Hopf bifurcation curve. Let us now summarize the stability scenario of the system for $b \geq 0$: (i) $x^* = 0$: for this fixed point, the condition of stability reads $b < \frac{1}{-n+ml}$ for any $\tau \geq 0$. Beyond this value of b, for any $\tau \geq 0$, the trivial fixed point $x^* = 0$ becomes unstable through a pitchfork bifurcation and $\pm p1$ fixed points emerge. (ii) $x^* = \pm p1$: These two nontrivial fixed points come into play for $b \geq \frac{1}{-n+ml}$. Since at these fixed points $|J_\tau| > |-a|$, thus

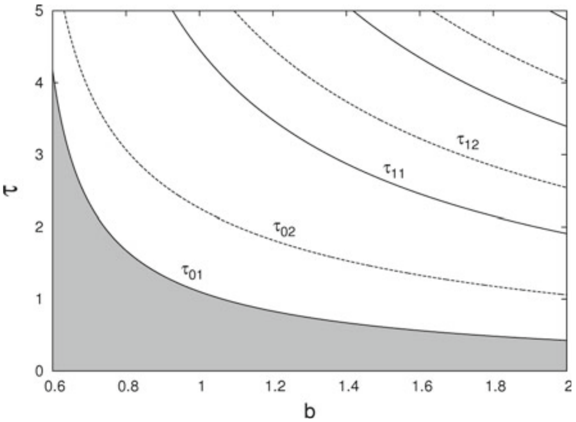

Fig. 2.2 Stability zone in the b–τ $(b > 0)$ parameter space with parameters $a = 1$, $n = 2.2$, $m = 1$, and $l = 10$. Shaded region indicates the zone of stable fixed point

the system depicts a stable fixed point for the delay τ, in $0 \leq \tau < \tau_{01}$. Beyond $\tau = \tau_{01}$, Hopf bifurcation occurs and a stable limit cycle appears.

Next, we study the direction of Hopf bifurcation and the stability of the bifurcating solutions for $x^* = \pm p1$ at $\tau = \tau_{01}$. Using the techniques described by Wei [144], let us define

$$D = \frac{1}{1 + \tau_{01} a - i\tau_{01}\nu_0}. \tag{2.23}$$

We can obtain the following coefficients:

$$\begin{aligned}
g_{20} &= \bar{D} b \tau_{01} f''(x^*) e^{-2i\tau_{01}\nu_0}, \\
&= -2\bar{D} b \tau_{01} m l^2 \operatorname{sech}^2(lx^*) \tanh(lx^*) e^{-2i\tau_{01}\nu_0}, \\
g_{11} &= \bar{D} b \tau_{01} f''(x^*), \\
&= -2\bar{D} b \tau_{01} m l^2 \operatorname{sech}^2(lx^*) \tanh(lx^*), \\
g_{02} &= \bar{D} b \tau_{01} f''(x^*) e^{2i\tau_{01}\nu_0}, \\
&= -2\bar{D} b \tau_{01} m l^2 \operatorname{sech}^2(lx^*) \tanh(lx^*) e^{2i\tau_{01}\nu_0},
\end{aligned} \tag{2.24}$$

$$\begin{aligned}
g_{21} &= \bar{D} b \tau_{01} \Big[f''(x^*)\{e^{-i\tau_{01}\nu_0} W_{11}(-1) + e^{i\tau_{01}\nu_0} W_{20}(-1)\} + f'''(x^*) e^{-i\tau_{01}\nu_0} \Big], \\
&= -2ml^2 \bar{D} b \tau_{01} \operatorname{sech}^2(lx^*) \Big[\{e^{-i\tau_{01}\nu_0} W_{11}(-1) + e^{i\tau_{01}\nu_0} W_{20}(-1)\} \tanh(lx^*) \\
&\qquad - l\{2 - 3\operatorname{sech}^2(lx^*)\} e^{-i\tau_{01}\nu_0} \Big],
\end{aligned}$$

where

$$\begin{aligned}
W_{20}(-1) &= -\frac{g_{20}}{i\tau_{01}\nu_0}e^{-i\tau_{01}\nu_0} - \frac{\bar{g}_{02}}{3i\tau_{01}\nu_0}e^{i\tau_{01}\nu_0} + E_1 e^{-2i\tau_{01}\nu_0},\\
W_{11}(-1) &= \frac{g_{11}}{i\tau_{01}\nu_0}e^{-i\tau_{01}\nu_0} - \frac{\bar{g}_{11}}{i\tau_{01}\nu_0}e^{i\tau_{01}\nu_0} + E_2,\\
E_1 &= \frac{bf''(x^*)e^{-2i\tau_{01}\nu_0}}{2i\nu_0 + a - bf'(x^*)e^{-2i\tau_{01}\nu_0}},\\
&= \frac{-b\{2ml^2\,\mathrm{sech}^2(lx^*)\tanh(lx^*)\}e^{-2i\tau_{01}\nu_0}}{2i\nu_0 + a - b\big[-n + ml\,\mathrm{sech}^2(lx^*)\big]e^{-2i\tau_{01}\nu_0}},
\end{aligned}$$

and

$$\begin{aligned}
E_2 &= \frac{bf''(x^*)}{a - bf'(x^*)},\\
&= \frac{-2bml^2\,\mathrm{sech}^2(lx^*)\tanh(lx^*)}{a - b\big[-n + ml\,\mathrm{sech}^2(lx^*)\big]}.
\end{aligned}$$

Because each g_{ij} in equation set (2.24) is expressed by the parameters and delay, we can compute the following quantities:

$$\begin{aligned}
c_1(0) &= \frac{i}{2\tau_{01}\nu_0}\left(g_{11}g_{20} - 2|g_{11}|^2 - \frac{|g_{02}|^2}{3}\right) + \frac{g_{21}}{2},\\
\mu_2 &= -\frac{\mathrm{Re}(c_1(0))}{\mathrm{Re}(\lambda'(\tau_{01}))},\\
\beta_2 &= 2\mathrm{Re}(c_1(0)),\\
T_2 &= -\frac{\mathrm{Im}(c_1(0)) + \mu_2\mathrm{Im}(\lambda'(\tau_{01}))}{\nu_0}.
\end{aligned} \tag{2.25}$$

The parameter μ_2 determines the direction of the Hopf bifurcation: if $\mu_2 > 0$ ($\mu_2 < 0$), then the Hopf bifurcation is *supercritical (subcritical)* and the bifurcating periodic solutions exist for $\tau > \tau_{01}$ ($\tau < \tau_{01}$). β_2 determines the stability of bifurcating periodic solutions: the bifurcating periodic solutions are orbitally asymptotically *stable (unstable)* if $\beta_2 < 0$ ($\beta_2 > 0$). Finally, T_2 determines the period of bifurcating periodic solutions: the period *increases (decreases)* if $T_2 > 0$ ($T_2 < 0$).

To test the validity of our analysis, let us use the following parameter values: $a = 1, n = 2.2, m = 1$, and $l = 10$. For $b = 1$, we have $p1 = 0.31$, $J_0 = -a = -1$, and $J_\tau = b[-n + ml\,\mathrm{sech}^2(\pm lp_1)] = -2.121$. Thus, we see that $|J_\tau| > |J_0|$ (satisfying Eq. (2.16)). Also, at these parameter values, we have $\tau_{01} = 1.102$ (from Eq. (2.17)). Thus, we expect that at $b = 1$ and $\tau_{01} = \tau_H = 1.102$, the fixed point losses its stability through Hopf bifurcation. Further, at these parameter values, we have $g_{11} = -0.421 + 0.413i$, $g_{20} = 0.582 + 0.095i$, $g_{02} = -0.11 - 0.58i$, $g_{21} = -11.622 - 3.812i$, $E_1 = -0.217 - 0.082i$, $E_2 = -0.525$, $W_{20} = 0.519 - 0.302i$,

$W_{11} = -0.354$, and $c_1(0) = -5.86 - 2.172i$. Using these set of values in Eq. (2.25), we have $\mu_2 = 14.524 > 0$; that means the resulting bifurcation is a *supercritical* Hopf bifurcation. Also, since $\beta_2 = -11.72 < 0$, thus the bifurcating periodic solutions are orbitally asymptotically stable. Finally, $T_2 = 11.142 > 0$ indicates that the period of the limit cycle increases with increasing τ.

2.2.2 *Negative* b

Let us define $b = -b_1$, where $b_1 > 0$. For negative b, we have

$$ax^* = -b_1 f(x^*). \tag{2.26}$$

This gives the following equation: $\tanh(lx^*) = -\frac{a-nb_1}{mb_1}x^*$. Again a close observation reveals that for $b_1 \leq \frac{a}{n}$, one has only one trivial fixed point, which is $x^* = 0$; beyond this value of b, there exists three equilibrium points, namely $x^* = q1,\ 0,$ and $-q1$. Using the similar arguments of the previous subsection, we can show that the nontrivial fixed points (i.e., $\pm q1$) are unstable for any $\tau \geq 0$. For the trivial fixed point (i.e., $x^* = 0$), we can derive the following equations:

$$J_0 = -a, \quad \text{and} \quad J_\tau = -b_1[-n + ml]. \tag{2.27}$$

Now, the *characteristic equation* is given by

$$\lambda = -a - b_1[-n + ml]e^{-\lambda\tau}. \tag{2.28}$$

Stability for $\tau = 0$ can be found as $a > -b_1[-n + ml]$. Also, for $\tau \neq 0$, from the condition $|J_\tau| \geq |J_0|$, we have the condition of stability: $\left|b_1[-n+ml]\right| \geq |-a|$. Next, similar as the previous section, we can have the set of curves from the expressions of τ_{k1} and τ_{k2} given by Eq. (2.17) with the values of J_0 and J_τ given by Eq. (2.27). These set of curves are shown in Fig. 2.3. We can show that Eq. (2.22) holds good for negative b also; thus, we conclude that, for negative b, the stability zone lies between the curves $\tau = 0$ and τ_{01} in the figure.

To test the validity of our analysis, let us use the following parameter values: $a = 1$, $n = 2.2$, $m = 1$, and $l = 10$. For $b = -1$, we get $J_0 = -a = -1$ and $J_\tau = -b_1[-n + ml\ \text{sech}^2(lx^*)] = -7.8$ ($x^* = 0$). Thus, we see that $|J_\tau| > |J_0|$ (satisfying Eq. (2.11)). Also, at these parameter values, we have $\tau_{01} = 0.22$ (from Eq. (2.17)). Thus, we expect that at $b = -1$ and $\tau_{01} = \tau_H = 0.22$, the fixed point losses its stability through Hopf bifurcation. Further, at these parameter values, we have $g_{11} = g_{20} = g_{02} = 0$, $g_{21} = -184.934 - 99.586i$, $E_1 = E_2 = 0$, $W_{20} = W_{11} = 0$, and $c_1(0) = -92.467 - 49.793i$. Using these set of values in Eq. (2.25), we have $\mu_2 = 6.761 > 0$; that means the resulting bifurcation is a *supercritical* Hopf bifurcation. Also, $\beta_2 = -184.934 < 0$ indicates that the bifurcating periodic

Fig. 2.3 Stability zone in the b–τ ($b < 0$) parameter space with parameters $a = 1$, $n = 2.2$, $m = 1$, and $l = 10$. Shaded region indicates the zone of stable fixed point

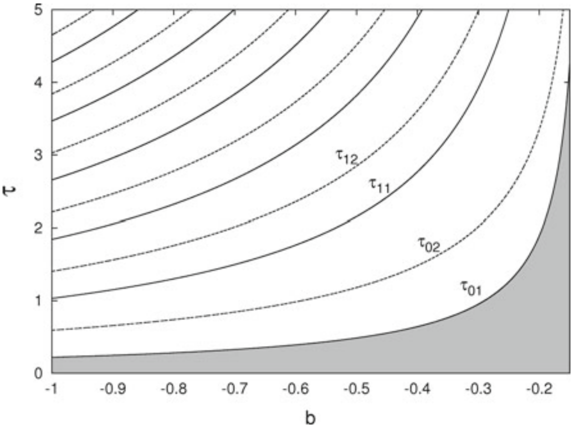

Fig. 2.4 Full stability diagram in $b - \tau$ space, with parameters $a = 1$, $n = 2.2$, $m = 1$, and $l = 10$. The shaded region represents the zone of stable fixed point

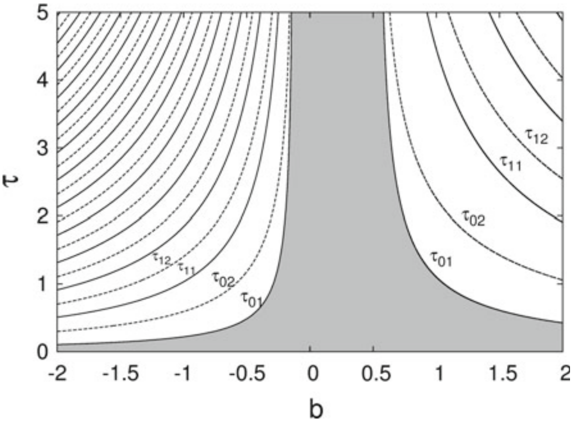

solutions are orbitally asymptotically stable. Finally, we have $T_2 = 28.635 > 0$; thus, the period of the limit cycle increases with increasing τ. To sum up the whole scenario of the stability, we present the stability diagram in $b - \tau$ space in Fig. 2.4. The shaded region in the figure represents the zone of stable fixed points of the system.

2.3 Numerical Studies

System Eq. (2.1) is solved numerically using XPPAUT [35] with the fourth-order Runge–Kutta algorithm with step size $h = 0.005$. A constant initial function $\phi(t) = 0.8$ for $t \in [-\tau, 0]$ is used. We also verify that several other initial functions also give similar results. Care has been taken to allow the system to settle to the steady state by excluding a large number of transients.

2.3.1 Varying τ with Constant b

At first, we vary the time-delay τ with constant b. For all the numerical simulations, we consider the following system parameters: $a = 1, n = 2.2, m = 1$, and $l = 10$. As suggested by the stability diagram Fig. 2.4, in the following, we take two exemplary values of b: $b = 1$ and $b = -1$.

(i) $b = 1$: For $\tau \geq 1.102$, the fixed point loses its stability through Hopf bifurcation, which is in accordance with analysis of the previous section. At $\tau = 1.65$, limit cycle of period-1 becomes unstable and a period-2 (P2) cycle appears. Further, period doubling occurs at $\tau = 1.79$ (P2 to P4). Through a period-doubling sequence, the system enters into the chaotic regime at $\tau = 1.84$. With further increase of τ, at $\tau = 2.60$, the system shows the emergence of hyperchaos. The system shows a double scroll at $\tau \approx 3.24$. Phase-plane representation in the representative $x(t) - x(t - \tau)$ plane for different τ is shown in Fig. 2.5, which shows the following characteristics: period-1 ($\tau = 1.40$), period-2 ($\tau = 1.72$), chaos ($\tau = 1.94$), and double-scroll hyperchaos ($\tau = 3.52$).

(ii) $b = -1$: The fixed point loses its stability through Hopf bifurcation at $\tau = 0.22$ which again agrees with the analysis. Pitchfork bifurcation of the limit cycle occurs at $\tau = 1.3$. Period-2 and period-4 occurs at $\tau = 1.84$ and 1.99, respectively. Chaos appears at $\tau \approx 2.05$. Double scroll occurs at $\tau \approx 2.38$. Finally, hyperchaos occurs at $\tau \approx 3.39$. All the behaviors in phase space are

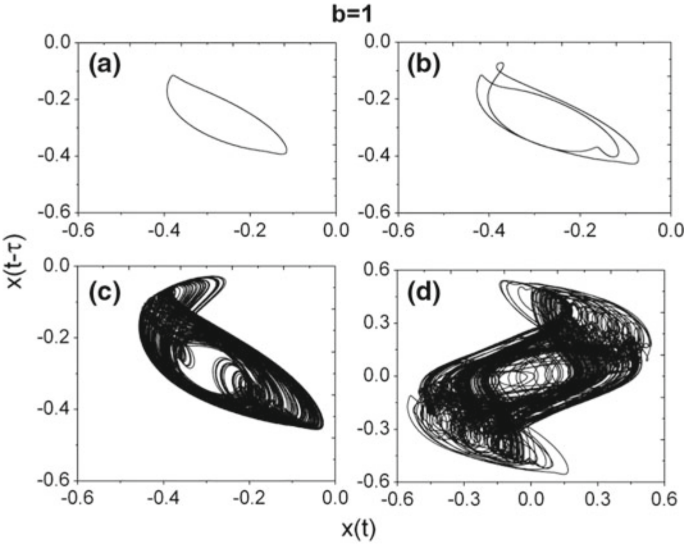

Fig. 2.5 Phase-plane plot in $x(t)$–$x(t - \tau)$ space for different τ ($b = 1$): **a** $\tau = 1.40$ (period-1), **b** $\tau = 1.72$ (period-2), **c** $\tau = 1.94$ (chaos), **d** $\tau = 3.52$ (double-scroll hyperchaos) (other parameters are $a = 1$, $n = 2.2$, $m = 1$, and $l = 10$)

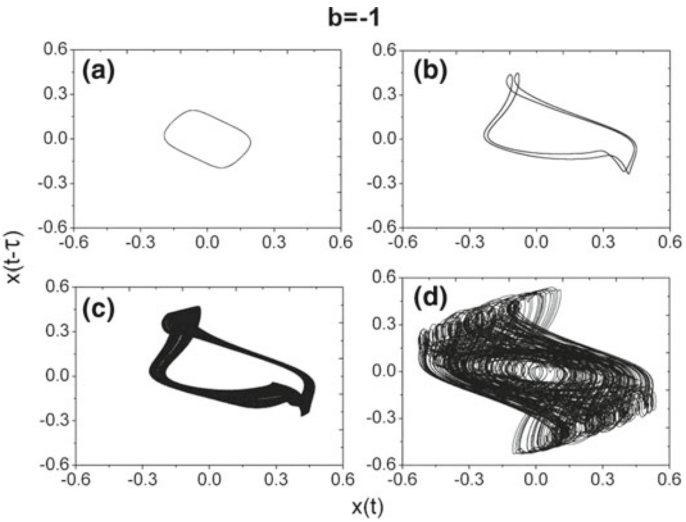

Fig. 2.6 Phase-plane plot in x–$x(t-\tau)$ space for different τ ($b=-1$): **a** $\tau=0.52$ (period-1), **b** $\tau=1.876$ (period-2), **c** $\tau=2.17$ (chaos), **d** $\tau=3.5$ (double-scroll hyperchaos) (other parameters are $a=1$, $n=2.2$, $m=1$, and $l=10$)

shown in Fig. 2.6. The representative real-time plots of the system for $b=0.96$ and $b=-0.96$ with $\tau=4$ is shown in Fig. 2.7.

These observations are summarized through a bifurcation diagram with τ as the control parameter. Bifurcation diagrams are obtained by plotting the local maxima of x, excluding a large number of transients ($\sim 10^6$). Figure 2.8A(a) and B(a) shows the bifurcation diagram of x with τ for $b=1$ and $b=-1$, respectively. Clearly, they show a period-doubling route to chaos. For quantitative measure of the system dynamics, we compute the first eight Lyapunov exponents using the algorithm proposed in [37]. Figure 2.8A(b) and B(b) shows the spectrum of Lyapunov exponents (LEs) in the τ parameter space. They agree well with the bifurcation diagrams. Figure 2.8A(c), B(c) show the corresponding Kaplan–Yorke dimensions (D_{KY}) with different τ. The presence of a strange attractor, multiple LEs, and higher values of D_{KY} (>3) ensures [72] that hyperchaos occurs for $\tau \approx 2.68$ ($b=1$) and $\tau \approx 3.25$ ($b=-1$).

2.3.2 Varying b *with Constant* τ

Next, we keep the delay fixed at $\tau=4$ and vary b to explore the system dynamics.

(i) $b>0$: Starting from $b=0$, if we increase b, at $b \approx 0.128$, the trivial fixed point $x=0$ losses stability through pitchfork bifurcation and nontrivial fixed points

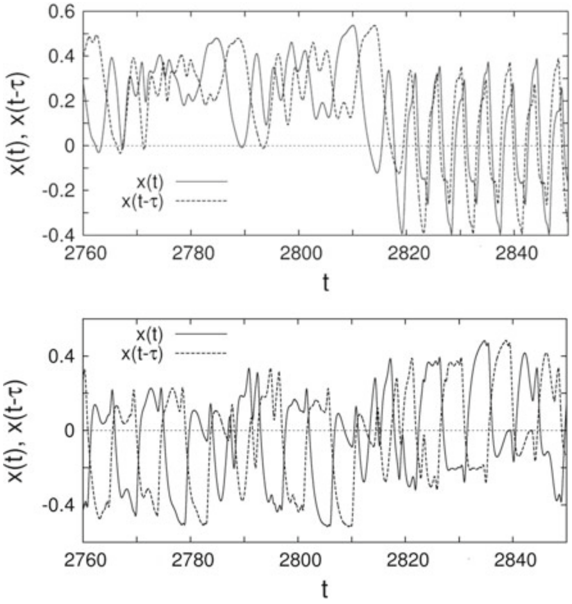

Fig. 2.7 Real-time plot in $x, x(t-\tau) - t$ for $b = 0.96$ (upper panel) and $b = -0.96$ (lower panel), $\tau = 4$ (other parameters are $a = 1$, $n = 2.2$, $m = 1$, and $l = 10$)

arise. Nontrivial fixed points become unstable through Hopf bifurcation and limit cycle appears at $b \approx 0.62 = b_{H+}$. At $b \approx 0.75$, limit cycle of period-1 becomes unstable and a period-2 (P2) cycle appears. Further, period doubling occurs at $b \approx 0.777$ (P2 to P4). Through a period-doubling cascade, the system enters into the chaotic regime at $b \approx 0.786$. With further increase in b, at $b \approx 0.9$, the system shows the hyperchaotic behavior. Double scroll appears at $b \approx 0.985$. Finally, the system equation shows diverging behavior for $b > 1$, indicating boundary crises.

(ii) $b < 0$: For $b \leq -0.156$, the trivial fixed point losses stability through Hopf bifurcation and gives birth to a limit cycle. Pitchfork bifurcation of limit cycle is observed at $b \approx -0.62$. Period-2 limit cycle appears at $b \approx -0.77$, and period-4 oscillation occurs at $b \approx -0.795$. At $b \approx -0.807$, we observe chaotic behavior. Double scroll hyperchaos is observed at $b \approx -0.98$. Phase-plane representation in the representative $x(t) - x(t-\tau)$ plane for different b is shown in Fig. 2.9, which shows the following characteristics: period-1 ($b = 0.70$), period-2 ($b = 0.76$), chaos ($b = 0.82$), and double scroll ($b = 0.99$); period-1 ($b = -0.2$), period-2 ($b = -0.78$), chaos ($b = -0.82$), and double scroll hyperchaos ($b = -1$).

As before, these observations are summarized through a bifurcation diagram with b as the control parameter. Figure 2.10a shows the bifurcation diagram of x with b. At $b_{H+} = 0.62$ and $b_{H-} = -0.156$, limit cycles emerge through Hopf bifurcation. Figure 2.10b shows the first eight LEs; it can be seen that for $b > 0.9$ and $b < -0.93$ we have two positive LEs indicating the occurrence of hyperchaos. This fact is

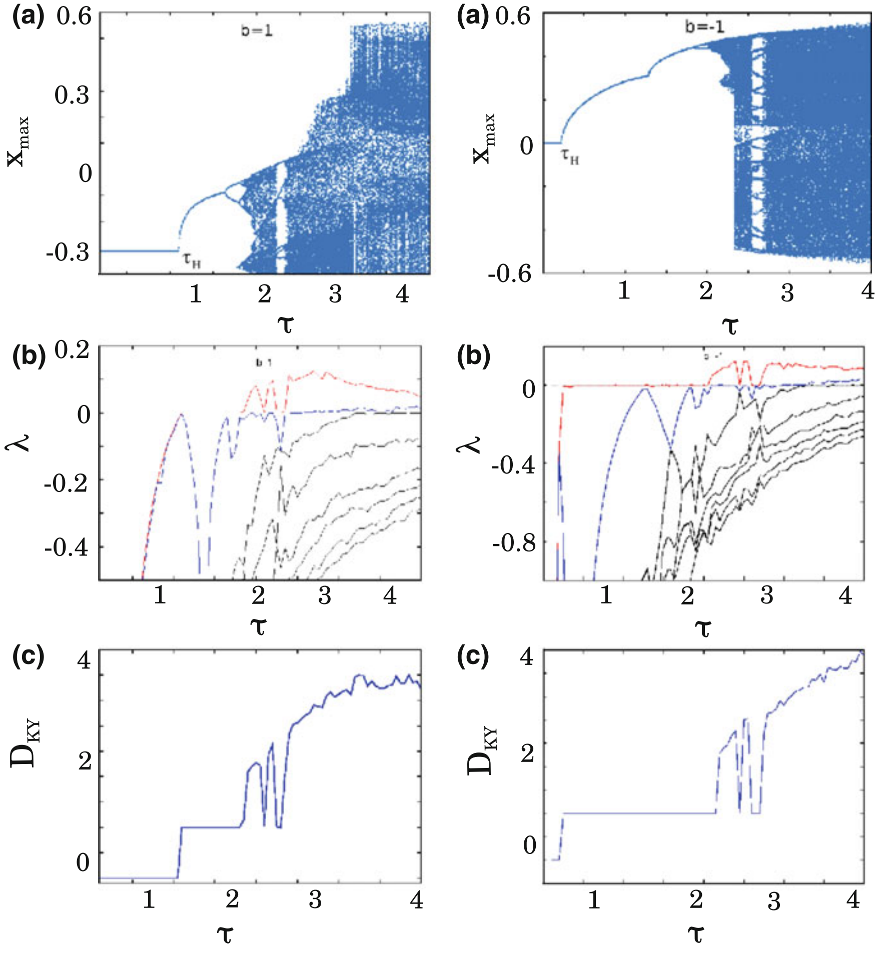

(A) b=1 (B) b=-1

Fig. 2.8 (A) $b = 1$:**a** Bifurcation diagram of x with τ as the control parameter. τ_H indicates the Hopf bifurcation point. **b** The first eight Lyapunov exponents (λ) with τ; First two LEs become positive for $\tau \geq 2.68$ indicating hyperchaos. **c** The corresponding Kaplan–Yorke dimension (D_{KY}).(B) $b = -1$: **a** Bifurcation diagram of x with τ as the control parameter. **b** The first eight Lyapunov exponents (λ) with τ; First two LEs become positive for $\tau \geq 3.25$ indicating hyperchaos. **c** The corresponding Kaplan–Yorke dimension (D_{KY}) (other parameters are same as in Fig. 2.5)

supported by Fig. 2.10c, which plots D_{KY} with b. It is noteworthy that to obtain hyperchaos we do not need to make τ large; a suitable choice of b with a moderate value of τ is sufficient to observe hyperchaos.

It is interesting to note that the nonlinearity of the system solely depends on the control parameters n, m, and l (see Fig. 2.1). The variation of these parameters changes the structure of the nonlinearity but the nature of the nonlinearity is kept

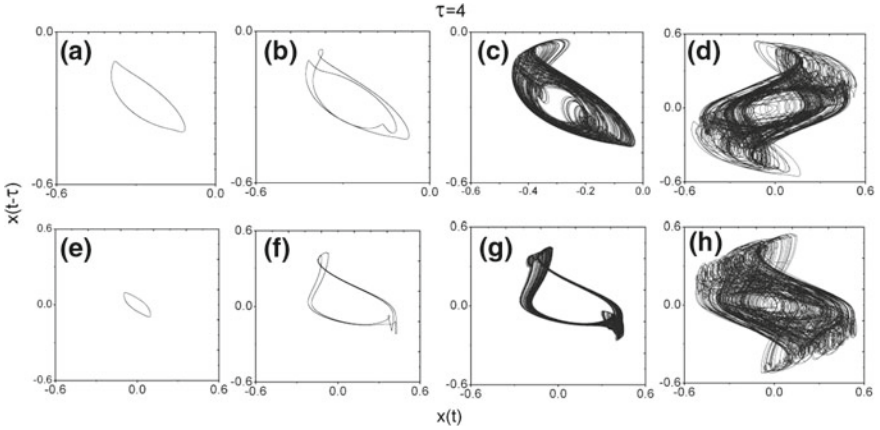

Fig. 2.9 Phase-plane plot in $x(t)$–$x(t-\tau)$ space for different b ($\tau = 4$): **a** $b = 0.7$ (period-1), **b** $b = 0.76$ (period-2), **c** $b = 0.82$ (chaos), **d** $b = 0.99$ (double scroll hyperchaos), **e** $b = -0.2$ (period-1), **f** $b = -0.78$ (period-2), **g** $b = -0.82$ (chaos), and **h** $b = -1$ (double scroll) (other parameters are $a = 1$, $n = 2.2$, $m = 1$, and $l = 10$)

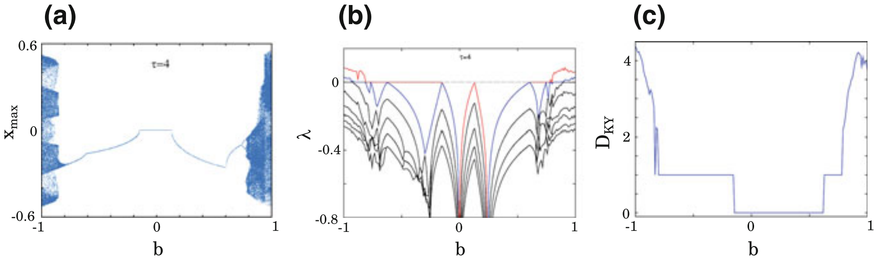

Fig. 2.10 **a** Bifurcation diagram of x with b as the control parameter. **b** The first eight Lyapunov exponents (λ) with b; First two LEs become positive for $b \geq 0.9$ and $b \leq -0.92$ indicating hyperchaos. **c** The corresponding Kaplan–Yorke dimension (D_{KY}). Parameter values are same as in Fig. 2.9

unaltered by keeping the condition $n < ml$ to have the double hump in the nonlinearity. In Fig. 2.11, we show the resulting forms of nonlinearity under the variation of each parameter by different shaded colors. The range of parameters is as follows: $n \in [1, 2.4]$ (cyan zone in Fig. 2.11), $m \in [0.5, 1.5]$ (yellow zone in Fig. 2.11), and $l \in [3, 12]$ (red zone in Fig. 2.11). Other parameters are $n = 2.2$, $m = 1$, and $l = 10$ if they are not used as control parameters. It is interesting to note that the change in the form of the nonilearity is also responsible to show the full spectrum of system dynamics.

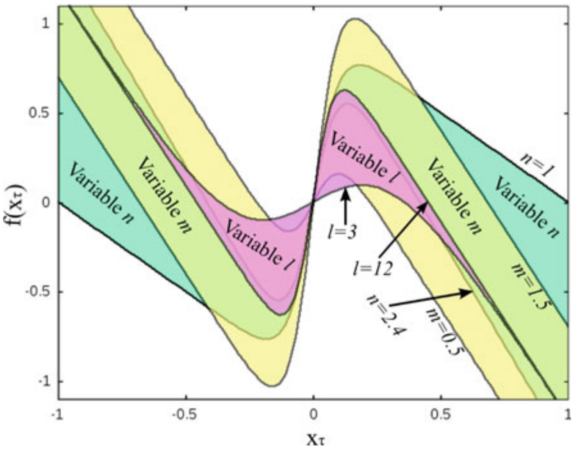

Fig. 2.11 Nonlinear zones for variable control parameters. $n \in [1, 2.4]$ (cyan zone), $m \in [0.5, 1.5]$ (yellow zone), and $l \in [3, 12]$ (red zone). Solid lines are for the parameters $n = 2.2$, $m = 1$, and $l = 10$

2.4 Experimental Studies

The system given by Eq. (2.1) (with the nonlinearity of Eq. (2.2)) is implemented in an analog electronic circuit as shown in Fig. 2.12. Here, $V(t)$ represents the voltage drop across the capacitor C_0 of the low-pass filter section $R_0 - C_0$. Figure 2.12 follows the following circuit equation:

$$R_0C_0\frac{dV(t)}{dt} = -V(t) + bf\big(V(t - T_d)\big). \tag{2.29}$$

Here, $b = \pm\frac{R_7}{R_6}$. Positive (negative) sign is considered if the junction "P" is connected to "A" ("B"). A4 is an unity gain inverting amplifier (i.e., $R_8 = R_9$). A5 and A6 are noninverting unity gain amplifiers acting as voltage buffers. $f\big(V(t - T_d)\big) \equiv f(V_\tau)$ is the nonlinear function representing the output of the nonlinear device (ND) of Fig. 2.12 in terms of the input voltage V_τ. T_D is the time delay produced by a delay block.

Figure 2.12 shows that ND consists of the following parts: The circuit associated with the A1 op-amp is a simple inverting amplifier of gain $\frac{R_2}{R_1}$. The output is a linear function of the input for a certain range of input voltage; for a higher input voltage, the output is saturated to a constant, $\pm V_{sat}$, which is the saturation voltage of op-amp. This nature of the op-amp-based amplifier can best be represented by the following function: $-\beta V_{sat} \tanh\left(w\frac{R_2}{R_1}\frac{V_\tau}{V_{sat}}\right)$. We chose a $\tanh(\cdot)$ function to represent a saturation-type nonlinearity because this particular function is widely considered in bipolar and CMOS IC design. Here, β and w are the scaling factors needed to fit the model with the experimental data; these two parameters depend upon the nonideal nature and asymmetry of the op-amps. In general, for smaller input voltages, $\beta \approx 1$ and $w \approx 1$. A2 acts as a weighted adder that adds V_τ and the output voltage of A1.

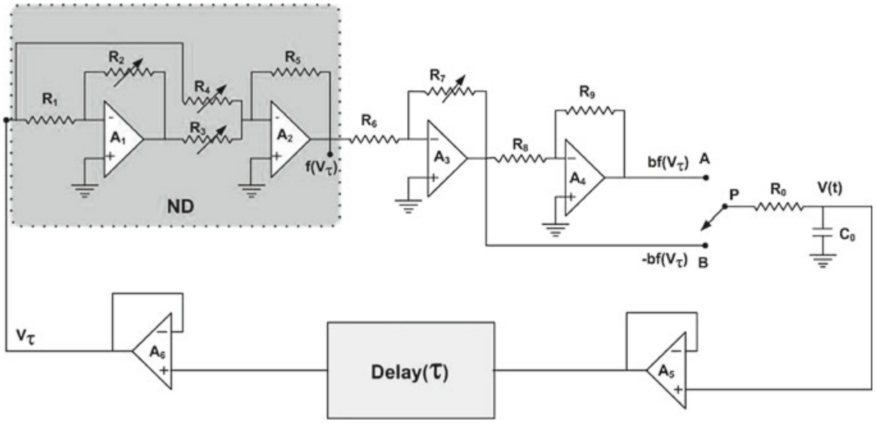

Fig. 2.12 Experimental circuit diagram. ND is the nonlinear device. A1–A6 are op-amps (TL074); low-pass section has $R_0 \approx 1\text{k}\Omega$ and $C_0 \approx 0.1\ \mu\text{F}$. For ND: $R_1 \approx 2.50$ kΩ, $R_2 \approx 20.23$ kΩ, $R_3 \approx 26.28$ kΩ, $R_4 \approx 8.71$ kΩ, $R_5 \approx 10$ kΩ. $R_6 \approx 1$ kΩ, and variable POT for R_7. Other resistors are $R_8 = R_9 \approx 10$ kΩ. Delay block contributes a delay of τ (see Fig. 2.13)

Fig. 2.13 Active first-order all-pass filter. A_0 is a TL074 op-amp. $R_{10} = R_{11} \approx 2.2$ kΩ, $C \approx 10$ nF

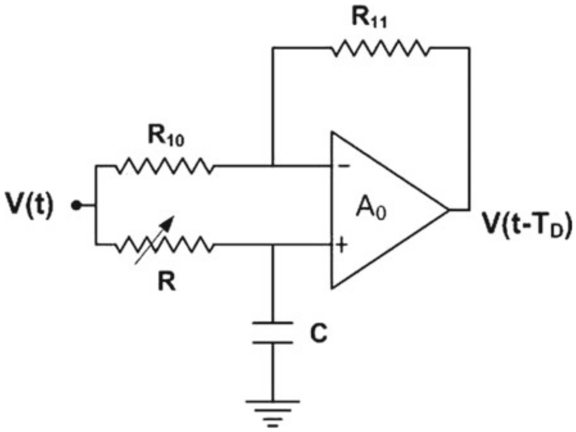

Therefore, we can write the following form of the nonlinearity:

$$f\big(V(t - T_D)\big) = -\frac{R_5}{R_4} V(t - T_D) + \frac{R_5}{R_3} \beta V_{sat} \tanh\left(w \frac{R_2}{R_1} \frac{V(t - T_D)}{V_{sat}} \right). \tag{2.30}$$

The variable delay element is realized by the first-order *all-pass filter* (APF) (Fig. 2.13) [115]. Design of an APF needs a single op-amp (A_0), an $R-C$ combination, which determines the phase shift between the input and output signals; two resistors R_{10} and R_{11} determine the gain of the APF. Thus, the APF has the following transfer function:

$$T(s) = -a_1 \frac{s - \omega_0}{s + \omega_0}, \tag{2.31}$$

with a flat gain $a_1 = \frac{R_{11}}{R_{10}}$, and $\omega_0 = 1/CR$ is the frequency at which the phase shift is $\pi/2$. In the present work, we take $R_{11} = R_{10}$, and thus $a_1 = 1$. Since it has a maximally linear phase response around the frequency ω_0, thus one can approximate that an APF imposes a delay of $T_D \approx RC$ around ω_0 [13]. Thus, i blocks produce a delay of $T_D \approx iRC$ ($i = 1, 2, \ldots$). By simply changing the resistance R, one can vary the amount of delay; thus, one can control the resolution of the delay line easily.

Let us define the following dimensionless variables and parameters: $t = \frac{t}{R_0 C_0}$, $\tau = \frac{T_d}{R_0 C_0}$, $x = \frac{V(t)}{V_{sat}}$, $x_\tau = \frac{V(t-T_D)}{V_{sat}}$, $\frac{R_5}{R_4} = n_1$, $\beta \frac{R_5}{R_3} = m_1$, and $w \frac{R_2}{R_1} = l_1$. Now, the system Eq. (2.29) can be reduced to the following dimensionless first-order, nonlinear delay differential equation:

$$\frac{dx}{dt} = -x(t) + bf\big(x(t-\tau)\big), \tag{2.32}$$

where

$$f\big(x(t-\tau)\big) \equiv f(x_\tau) = -n_1 x_\tau + m_1 \tanh(l_1 x_\tau). \tag{2.33}$$

It can be seen that Eq. (2.32) (along with Eq. (2.33)) is equivalent to Eq. (2.1) (along with Eq. (2.2)) with $a = 1$, and appropriate choice of n_1, m_1, and l_1.

In the hardware experiment, we use IC TL074 (quad JFET op-amp) with ±12 volt power supply. Capacitors (resistors) have 1% (5%) tolerance. For the low-pass section, we choose $R_0 \approx 1$ kΩ and $C_0 \approx 0.1$ μF. For the nonlinear device (ND), the following resistor values are used: $R_1 \approx 2.50$ kΩ, $R_2 \approx 20.23$ kΩ, $R_3 \approx 26.28$ kΩ, $R_4 \approx 8.71$ kΩ, and $R_5 \approx 10$ kΩ. Figure 2.14 shows the experimentally obtained nonlinearity produced by the ND. Qualitatively, it is equivalent to the nonlinear function "N1" of Fig. 2.1. The gain of the noninverting amplifier (A3) that follows the ND is designed with $R_6 \approx 1$ kΩ and variable R_7; R_7 is varied through a potentiometer to change the parameter b. Other resistors are $R_8 \approx 10$ kΩ and $R_9 \approx 10$ kΩ. For the delay section, the APF is designed with the following parameters: $R \approx 10$ kΩ

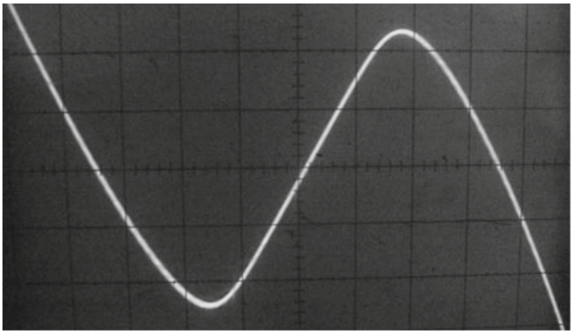

Fig. 2.14 Experimentally obtained nonlinearity produced by nonlinear device of Fig. 2.12. Scale: x-axis: 0.2 v/div and y-axis: 0.5 v/div

(POT), $C \approx 10$ nF, $R_8 \approx 2.2$ kΩ, and $R_9 \approx 2.2$ kΩ. Each APF contributes a delay of $T_D = RC = 0.1$ ms; thus, the dimensionless parameter $\tau = \frac{RC}{R_0 C_0} = 1$, i.e., one needs i blocks to produce a delay $\tau = i$. In the experiment, we vary R to get variable delays. Note that one can also change R_0 to get a variable delay, but in that case the power spectral property of the circuit will also be changed [89].

2.4.1 *Variable* τ*, Fixed* B

(i) *Positive* b: The nodes "A" and "P" of Fig. 2.12 are connected. We fix the value of b with $R_7 \approx 1.57$ kΩ (POT). Now, we vary the delay by varying R. At first to get a small delay, we use only one APF stage. For $R \geq 9.56$ kΩ (approx.), a stable limit cycle appears with frequency 3846 Hz. Next, we use two blocks of APF; $R \approx 10$ kΩ is taken for the first block (contributing ≈0.1 ms delay) and vary R of the second block; at $R = 0.35$ kΩ the limit cycle of period-1 loses its stability and a period-2 oscillation emerges. At $R \approx 6.43$ kΩ, chaotic oscillation occurs in the circuit. Next, we use three blocks of APF; $R \approx 10$ kΩ is taken for the first two blocks (contributing ≈ 0.2 ms delay) and vary R of the third block; the double-scroll hyperchaotic attractor is observed beyond $R \approx 6.84$ kΩ. All the above-mentioned behaviors are shown in Fig. 2.15 (in $V(t)$–$V(t - T_D)$ space), which depicts the experimental phase-plane plots recorded in a real-time oscilloscope (Aplab make, two channel, 60 MHz). It can be seen that the experimental results qualitatively agree well with the numerical simulations.

(ii) *Negative* b: The nodes "B" and "P" of Fig. 2.12 are connected. We fix the value of b with $R_7 = 1.56$ kΩ (POT). The following observations are made: period-1 (frequency 7692 Hz) is observed for single stage, $R \geq 9$ kΩ. Next, we use three blocks of APF: $R \approx 10$ kΩ is taken for the first two blocks (contributing ≈ 0.2 ms delay) and vary R of the third block. The following behaviors are observed: period-2 ($R \geq 2.77$ kΩ), chaos ($R \geq 4.09$ kΩ), and double scroll ($R \geq 9.54$ kΩ). Oscilloscope traces are shown in Fig. 2.16.

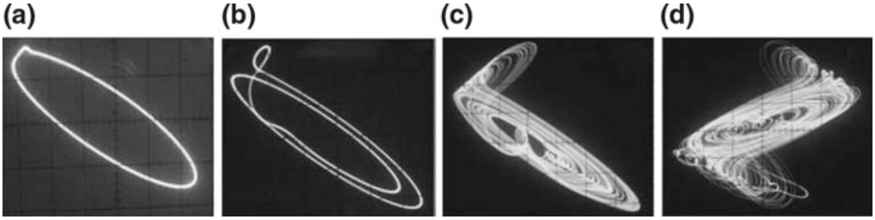

Fig. 2.15 Positive b: The oscilloscope trace of experimentally obtained phase-plane plots in the $V(t)$–$V(t - T_D)$ space for variable τ: **a** Period-1 **b** Period-2 **c** chaos **d** double scroll (for the parameter values see text). **a**–**c** V (x-axis): 0.2 v/div, $V(t - T_D)$ (y-axis): 0.2 v/div. **d** x-axis: 0.5 v/div, y-axis: 0.5 v/div

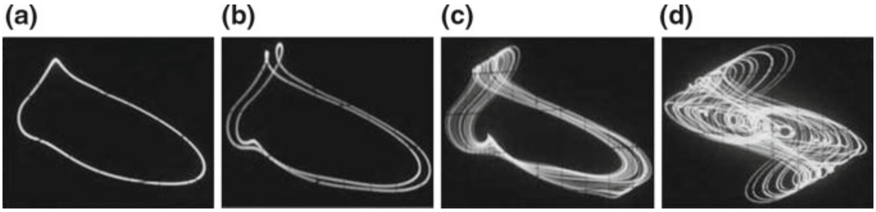

Fig. 2.16 Negative b: The oscilloscope trace of experimentally obtained phase-plane plots in the $V(t)$–$V(t - T_D)$ space for variable τ: **a** Period-1 **b** Period-2 **c** chaos **d** double scroll (for the parameters see text). **a–d** x-axis: 0.5 v/div, y-axis: 0.5 v/div

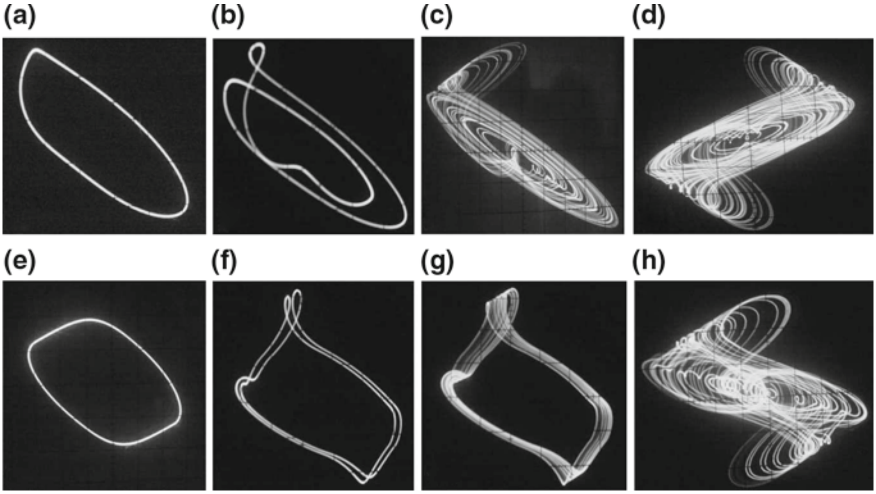

Fig. 2.17 The oscilloscope trace of experimentally obtained phase-plane plots in the $V(t)$–$V(t - T_D)$ space for variable b: "A"–"P" (of Fig. 2.12) are connected (positive b): **a** Period-1 at $R_7 = 1.01$ kΩ **b** Period-2 at $R_7 = 1.12$ kΩ **c** chaos at $R_7 = 1.3$ kΩ **d** double scroll at $R_7 = 1.7$ kΩ. "B"–"P" (of Fig. 2.12) are connected (negative b): **e** Period-1 at $R_7 = 0.75$ kΩ **f** Period-2 at $R_7 = 1.12$ kΩ **g** chaos at $R_7 = 1.30$ kΩ **h** double scroll at $R_7 = 1.45$ kΩ (for other parameters see text). **a–c** x-axis: 0.1 v/div, y-axis: 0.2 v/div. **d** x-axis: 0.5 v/div, y-axis: 0.5 v/div., and **e–g** x-axis: 0.1 v/div, y-axis): 0.2 v/div.; **h** x-axis: 0.5 v/div, y-axis: 0.5 v/div

2.4.2 *Variable* B, *Fixed* τ

(i) *Positive* b: The nodes "A" and "P" of Fig. 2.12 are connected. We set the time delay at $T_D = 0.4$ ms (i.e., $\tau = 4$) by using four APF blocks each having $R = 10$ kΩ. To observe the behavior of the system for different b, we vary R_7. For $R_7 \approx 1$ kΩ (i.e., $b = 1$), the circuit shows a stable limit cycle of frequency 833 Hz. At $R_7 = 1.07$ kΩ (approx.) (i.e., $b \approx 1.07$), the limit cycle of period-1 loses its stability and a period-2 oscillation emerges. Chaotic oscillation appears at $R_7 = 1.17$ kΩ (approx.) (i.e., $b \approx 1.17$). The circuit shows a double scroll for $R_7 > 1.61$ kΩ (i.e., $b \approx 1.61$). These behaviors are shown in Fig. 2.17

(upper row (a)–(d)) which represents the experimental oscilloscope traces in the $V(t) - V(t - T_D)$ space. One can observe the *qualitative* agreement between the numerical results and the experimental observations.

(ii) *Negative b*: The nodes “B” and “P” of Fig. 2.12 are connected. We set the time delay at $T_D = 0.4$ ms (i.e., $\tau = 4$). Following observations are made: period-1 ($R_7 \geq 0.67$ kΩ, $b = 0.67$), period-2 ($R_7 \geq 1.08$ kΩ, $b = 1.08$), chaos ($R_7 \geq 1.09$ kΩ, $b = 1.09$), and double scroll ($R_7 \geq 1.43$ kΩ, $b = 1.43$). All the above- mentioned behaviors are shown in Fig. 2.17 (lower row (e)–(h)) in $V(t)$–$V(t - T_D)$ space depicting the real-time oscilloscope traces. Thus, we see that the experimental results *qualitatively* agree well with the numerical results.

2.5 Time-Delayed System with Unimodal Nonlinearity: System Description

Next, we discuss the design principle of a chaotic time-delayed system with unimodal nonlinearity. The following is the first-order nonlinear retarded-type delay differential equation with a single constant delay

$$\dot{x} = -ax(t) - bf(x_\tau), \tag{2.34}$$

where a and b are the positive parameters. Also, $x_\tau \equiv x(t - \tau)$, where $\tau \in \mathscr{R}^+$ is a constant time delay. The nonlinear function of the above equation is given by the following equation:

$$f(x_\tau) = -0.5n\big(|x_\tau| + x_\tau\big) + m\tanh(lx_\tau), \tag{2.35}$$

where n, m, and l are all positive parameters controlling the nonlinearity.

The first term in the right-hand side of Eq. (2.35) represents the input–output characteristic of a half-wave (HW) rectifier. Thus, the nonlinear function is composed of the weighted superposition of two nonlinear functions, namely “HW” and “tanh(·)” functions. Figure 2.18 shows the nature of the nonlinearity for different values of n, m, and l. The nonlinearity shows a unimodal nature with single hump in the first quadrant, but unlike the nonlinearity of the Mackey–Glass (MG) system [79], it does not vanish asymptotically. There exists a large number of choices of n, m, and l that produce this particular nature of the nonlinearity.

2.6 Stability Analysis

To analyze the stability of the system given by Eq. (2.34), we rewrite it in the following form:

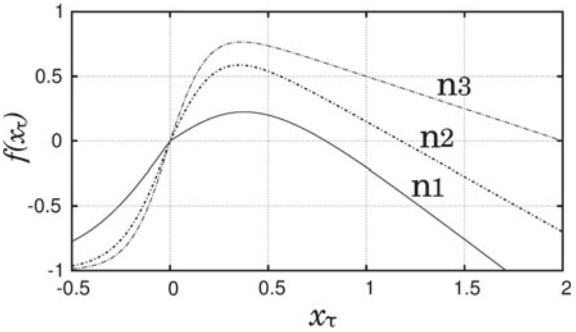

Fig. 2.18 Nonlinear function $f(x_\tau) = -0.5n(|x_\tau| + x_\tau) + m\tanh(lx_\tau)$: (n1) $n = 1.15$, $m = 0.97$, $l = 2.19$; (n2) $n = 0.85$, $m = 1$, $l = 4$; (n3) $n = 0.5$, $m = 1$, and $l = 5$

$$\dot{x} = g\Big(x(t), x_\tau\Big) = -ax(t) - bf(x_\tau). \tag{2.36}$$

The equilibrium condition implies $\dot{x} = 0$ and $x(t) = x_\tau = x^*$ (say), i.e., $g(x^*, x^*) = -ax^* - bf(x^*) = 0$. This gives $ax^* = -bf(x^*)$. This is a *transcendental equation*, which may be solved graphically (or numerically, e.g., Newton–Raphson method). The intersection of the two curves gives the solution, which is $x^* = 0$. Let us now examine the stability of the fixed point $x^* = 0$.

The analysis of stability is same as in Sect. 2.2. The condition of stability for $\tau = 0$ is given by

$$b\Big[-0.5n + ml\Big] > -a. \tag{2.37}$$

The stability condition for $\tau \neq 0$ gives the calculated values of τ as

$$\tau_{k1} = \frac{\Big[\cos^{-1}\Big(-\frac{J_0}{J_\tau}\Big) + 2k\pi\Big]}{\sqrt{{J_\tau}^2 - {J_0}^2}}, \qquad \text{for } J_\tau < 0, \tag{2.38a}$$

$$\tau_{k2} = \frac{\Big[\Big\{2\pi - \cos^{-1}\Big(-\frac{J_0}{J_\tau}\Big)\Big\} + 2k\pi\Big]}{\sqrt{{J_\tau}^2 - {J_0}^2}}, \qquad \text{for } J_\tau > 0, \tag{2.38b}$$

where $k = 0, 1, 2, \ldots$, and J_0 and J_τ are the same as Eqs. (2.6) and (2.7).

The condition of stability of the system reads the following form:

$$\Big|-b(0.5n - ml)\Big| \geq |-a|. \tag{2.39}$$

Also, we get the derivative of the real part of the eigenvalue as

$$\mu'(\tau_k) = \frac{{\nu_0}^2}{(1 + \tau_k a)^2 + \tau_k^2 \nu_0^2}. \tag{2.40}$$

Thus, $\mu'(\tau_k) > 0$ for any $k = 0, 1, 2, \ldots$. Thus, we conclude that the stable state lies between $\tau = 0$ and τ_{01}.

Figure 2.19 shows the first six stability curves τ_{ki} ($i = 1, 2$) (using Eqs. (2.38a) and (2.38b)) in the $b - \tau$ parameter space. We have used the following parameters: $a = 1$, $n = 1.15$, $m = 0.97$, and $l = 2.19$ (as we have used in "n1" of Fig. 2.18). In the figure, τ_{k1} and τ_{k2} are represented by the solid and dotted lines, respectively. Since $\mu(\tau_k) > 0$ for any $k = 0, 1, 2, \ldots$, thus the stability zone cannot be situated between two τ_{ki} curves; so we conclude that the stable island lies between the $\tau = 0$ and the τ_{01} curve. The shaded region in the figure represents the stable zone, and the τ_{01} curve represents the Hopf bifurcation curve.

Further, we analyze the stability of the system using TRACE-DDE package in which *pseudospectral approach* is considered [23]. The package is employed for the calculation of stability zone. In Fig. 2.20a, we show the stability boundary and in Fig. 2.20b the stability surface. This figure closely resembles our analytically obtained results as shown in Fig. 2.19.

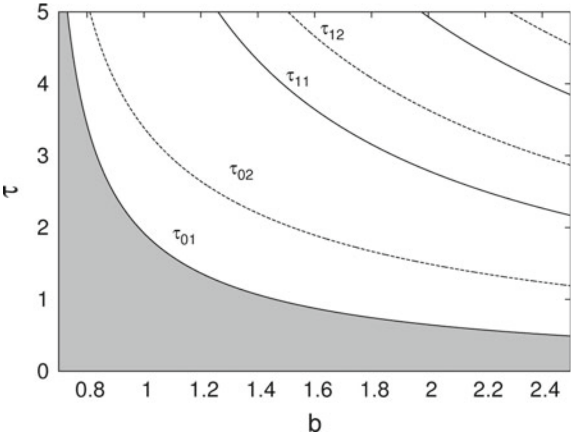

Fig. 2.19 Stability zone in the $b - \tau$ parameter space with parameters $a = 1$, $n = 1.15$, $m = 0.97$, and $l = 2.19$. The shaded region indicates the zone of the stable fixed point

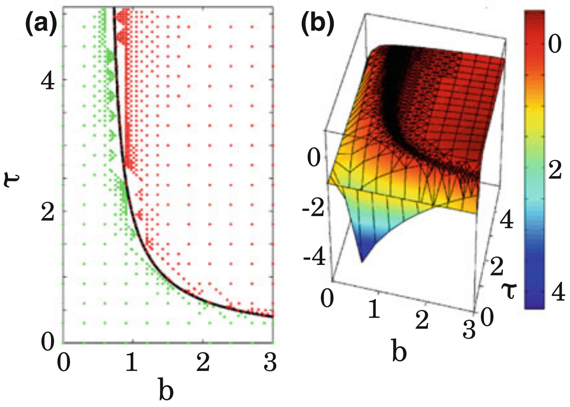

Fig. 2.20 Stability zone in $b - \tau$ parameter space obtained by the numerical package TRACE-DDE: **a** Stability boundary and **b** Stability surface. The parameters are same as in Fig. 2.19

From the aforesaid discussion, it is clear that the system undergoes a Hopf bifurcation to loose its stability. Now, we want to find out the type of Hopf bifurcation occurring in the system and also its stability. For this, we consider the stability and direction of hopf bifurcation as discussed in Sect. 2.2.1. The outcomes of the analysis are as follows: To test the validity of our analysis, let us use the following parameter values: $a = 1$, $n = 1.15$, $m = 0.97$, and $l = 2.19$. For $b = 1.7$, we get $J_0 = -a = -1$ and $J_\tau = -b[-0.5n + ml] = -2.634$. Thus, we see that $|J_\tau| \geq |J_0|$ (satisfying Eqs. (2.37) and (2.39)). Also, at these parameter values, we have $\tau_{01} = 0.805$ (from Eq. (2.38a)). Thus, we expect that at $b = 1.7$ and $\tau_{01} = \tau_H = 0.805$, the fixed point losses its stability through Hopf bifurcation. Further, at these parameter values, we have $g_{11} = g_{20} = g_{02} = 0$, $g_{21} = -9.809 - 3.632i$, $E_1 = E_2 = 0$, $W_{20} = W_{11} = 0$, and $c_1(0) = -4.904 - 1.816i$. Using these set of values in Eq. (2.25), we have $\mu_2 = 5.864 > 0$; that means the resulting bifurcation is a *supercritical* Hopf bifurcation. Also, $\beta_2 = -9.809 < 0$; thus the bifurcating periodic solutions are orbitally asymptotically stable. Finally, since $T_2 = 6.182 > 0$, the period of the limit cycle increases with increasing τ.

2.7 Numerical Studies

The system Eq. (2.34) is integrated numerically using the package XPPAUT [35] (using the fourth-order Runge–Kutta algorithm with a step size $h = 0.005$). We use a constant initial function $\phi(t) = 1$ for $t \in [-\tau, 0]$.

2.7.1 Varying τ *with Constant* b

Guided by the analytical results, at first, we vary the time delay τ keeping b constant at $b = 1.7$. Also, the other parameters are kept at $a = 1$, $n = 1.15$, $m = 0.97$, and $l = 2.19$. We find that for $\tau \geq 0.805$, the fixed point loses its stability through Hopf bifurcation, which is in accordance with the analysis of the previous section. At $\tau \approx 2.23$, limit cycle of period-1 becomes unstable and a period-2 (P2) cycle appears. Further, period doubling occurs at $\tau \approx 2.91$ (P2 to P4) and then at $\tau \approx 3.07$ (P4 to P8). Through a period-doubling sequence, the system enters into the chaotic regime at $\tau = 3.1$. With further increase of τ, at $\tau = 3.60$, the system shows the emergence of hyperchaos.

A phase-plane representation in the representative $x(t) - x(t - \tau)$ plane for different τ is shown in Fig. 2.21, which shows the following characteristics: period-1 ($\tau = 1.90$), period-2 ($\tau = 2.76$), period-4 ($\tau = 2.93$), period-8 ($\tau = 3.07$), chaos ($\tau = 3.17$), hyperchaos ($\tau = 4.78$), and $b = 1.7$.

These observations are summarized through a bifurcation diagram (Fig. 2.22) with τ as the control parameter; clearly, it shows a period-doubling route to chaos. Figure 2.22 (middle panel) shows the spectrum of Lyapunov exponents (LEs) in the

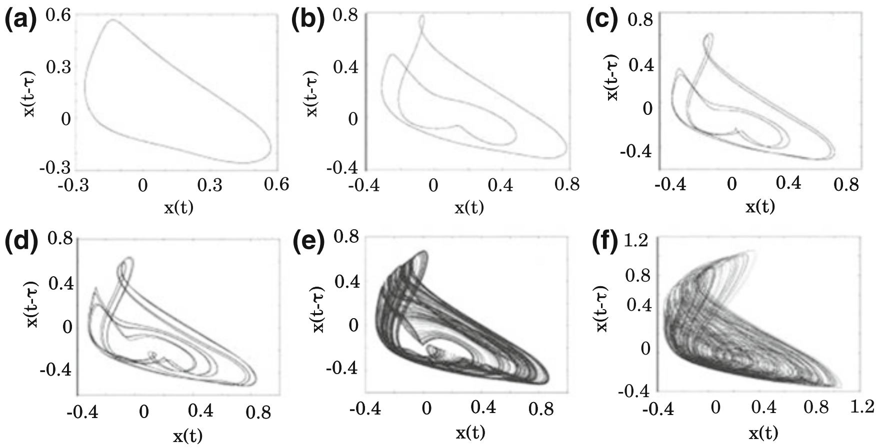

Fig. 2.21 Phase-plane plots in $x - x(t - \tau)$ space for different τ: **a** $\tau = 1.90$ (period-1), **b** $\tau = 2.76$ (period-2), **c** $\tau = 2.93$ (period-4), **d** $\tau = 3.07$ (period-8), **e** $\tau = 3.17$ (chaos), and **f** $\tau = 4.78$ (hyperchaos). Other parameters are $a = 1$, $b = 1.7$, $n = 1.15$, $m = 0.97$, and $l = 2.19$

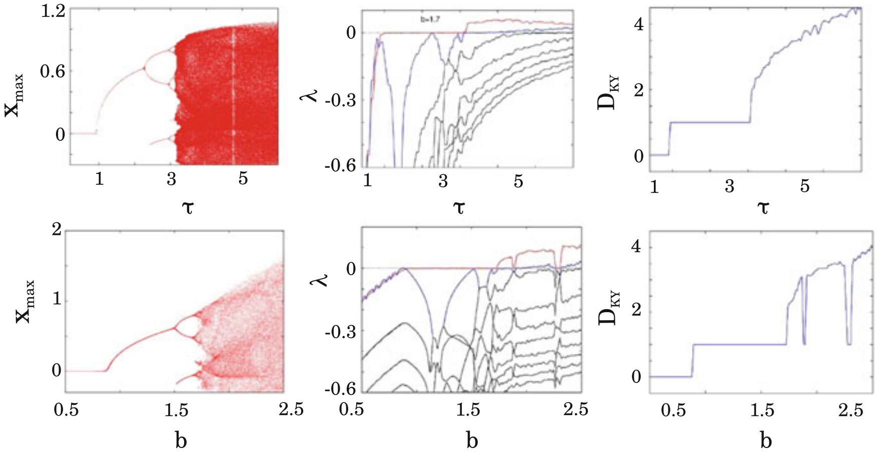

Fig. 2.22 Upper row: Bifurcation diagram of x (*Left panel*) with τ as the control parameter. *Middle* panel shows the first nine Lyapunov exponents (λ) with τ. The first two LEs become positive for $\tau \geq 3.60$, indicating hyperchaos. *Right panel* shows the corresponding Kaplan–Yorke dimension (D_{KY}), ($b = 1.7$). Lower row: Bifurcation diagram of x (*Left panel*) with b as the control parameter. *Middle panel* shows the first ten Lyapunov exponents (λ) with b; the first two LEs become positive for $b \geq 1.9$, indicating hyperchaos. *Right panel* shows the corresponding Kaplan–Yorke dimension (D_{KY}), ($\tau = 3$). Other parameters are $a = 1$, $n = 1.15$, $m = 0.97$, and $l = 2.19$

τ parameter space. The presence of a positive LE *along with the observed strange attractor* and bifurcation diagram indicates the occurrence of a chaotic behavior in the system. Figure 2.22 (right panel) shows the Kaplan–Yorke dimension (D_{KY}) with different τ. The presence of multiple positive LEs and higher values of $D_{KY}(> 3)$ indicates that hyperchaos occurs for $\tau \geq 3.60$.

2.7.2 *Varying* b *with Constant* τ

Next, we keep the delay fixed at $\tau = 3$ and vary b to explore the system dynamics. It is observed that with increasing b, for $b < 0.834 = b_H$, the system shows a fixed point at $x = 0$. For $b \geq b_H = 0.834$, the fixed point loses its stability through Hopf bifurcation, and a stable limit cycle emerges. This is in well agreement with our analytical results of the previous section. At $b = 1.51$, the limit cycle of period-1 becomes unstable and a period-2 (P2) cycle appears. Further period doubling occurs at $b = 1.68$ (P2 to P4) and at $b = 1.73$ (P4 to P8). Through period-doubling bifurcations, the system enters into the chaotic regime at $b = 1.73$. With further increase of b, at $b = 2.1$, the system shows the emergence of hyperchaos. Finally, the system equation shows diverging behavior beyond $b = 2.52$, indicating boundary crises. A phase-plane representation in the representative $x(t) - x(t - \tau)$ plane for different b is shown in Fig. 2.23, which shows the following characteristics: period-1 ($b = 1.36$), period-2 ($b = 1.64$), period-4 ($b = 1.70$), period-8 ($b = 1.73$), chaos ($b = 1.76$), and hyperchaos ($b = 2.40$).

These observations are summarized through a bifurcation diagram with b as the control parameter Fig. 2.22 (lower row). The observations are further supported by

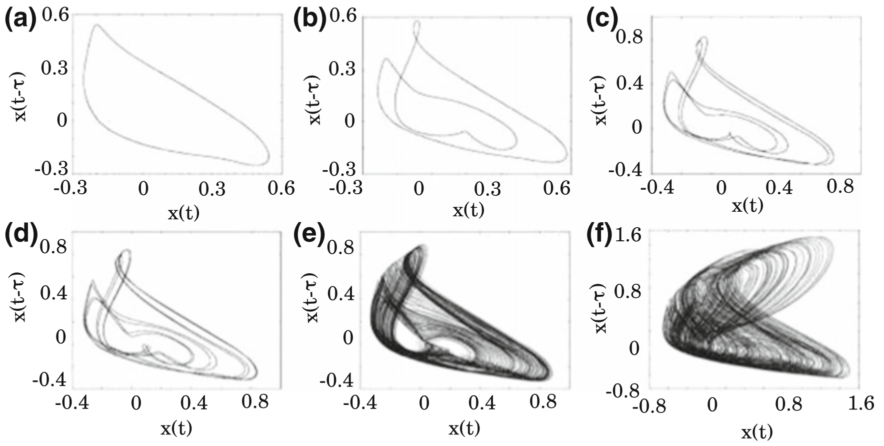

Fig. 2.23 Phase-plane plots in $x - x(t - \tau)$ space for different b: **a** $b = 1.36$ (Period-1), **b** $b = 1.64$ (Period-2), **c** $b = 1.70$ (Period-4), **d** $b = 1.73$ (Period-8), **e** $b = 1.76$ (chaos), and **f** $b = 2.40$ (hyperchaos). Other parameters are $a = 1$, $n = 1.15$, $m = 0.97$, $l = 2.19$, and $\tau = 4$

Fig. 2.22 (right panel), which plots D_{KY} with b. It is noteworthy that to obtain hyperchaos we do not need to make τ high but a suitable choice of b with a moderate value of τ is sufficient.

2.8 Experimental Observations

We implement the system described by Eq. (2.34) using analog electronic circuit. Figure 2.24 shows the representative diagram of the experimental circuit. Let $V(t)$ be the voltage drop across the capacitor C_0 of the low-pass filter section $R_0 - C_0$; thus, the following equation represents the time evolution of the circuit

$$R_0 C_0 \frac{dV(t)}{dt} = -V(t) - \frac{R_7}{R_6} f\big(V(t - T_D)\big), \tag{2.41}$$

where $f\big(V(t - T_D)\big) = f(V_\tau)$ is the nonlinear function representing the output of the nonlinear device (ND) of Fig. 2.24 in terms of the input voltage V_τ. T_D is the time delay produced by the delay block. The different blocks of this figure are illustrated in detail in Figs. 2.25 and 2.13, respectively. The former shows the "ND" part and

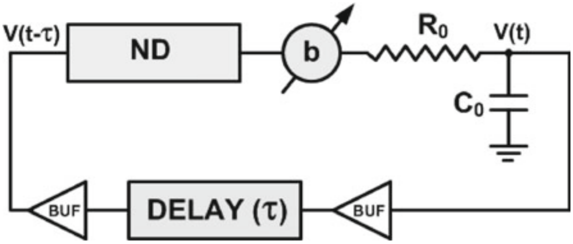

Fig. 2.24 Experimental circuit diagram. $R_0 = 1\ \text{k}\Omega$, $C_0 = 100$ nF. Buffers are designed with unity gain noninverting op-amps

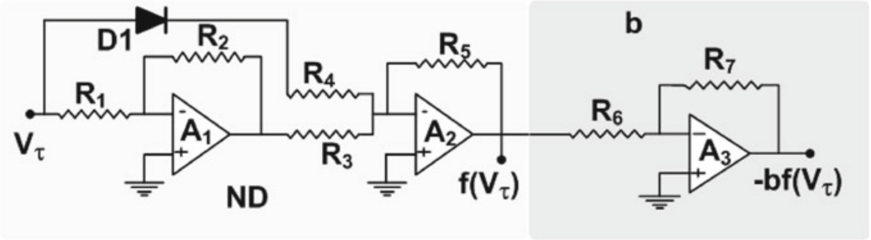

Fig. 2.25 Nonlinear device (ND) along with the amplifying stage (b). A1–A3 are op-amps (TL074), D1 is the diode: 1N4148, $R_1 \approx 10\ \text{k}\Omega$, $R_2 \approx 18.5\ \text{k}\Omega$, $R_3 \approx 12.05\ \text{k}\Omega$, $R_4 \approx 8.25\ \text{k}\Omega$, and $R_5 = R_6 \approx 10\ \text{k}\Omega$

the latter shows the "Delay" part, respectively. We can write the following form of the nonlinearity:

$$f\big(V(t-T_D)\big) = -\frac{R_5}{R_4}0.5\Big[\big|V(t-T_D)\big| + V(t-T_D)\Big] + \frac{R_5}{R_3}\beta V_{sat}\tanh\left(\omega\frac{R_2}{R_1}\frac{V(t-T_D)}{V_{sat}}\right). \tag{2.42}$$

As before, the variable delay element is realized by the first-order all-pass filter (APF) (Fig. 2.13, p. 26).

Let us define the following dimensionless variables and parameters: $t = \frac{t}{R_0C_0}$, $\tau = \frac{T_D}{R_0C_0}$, $x = \frac{V(t)}{V_{sat}}$, $x(t-\tau) = \frac{V(t-\tau)}{V_{sat}}$, $n_1 = \frac{R_5}{R_4}$, $m_1 = \beta\frac{R_5}{R_3}$, and $l_1 = \omega\frac{R_2}{R_1}$. Now, the system Eq. (2.41) can be reduced to the following dimensionless equation:

$$\frac{dx}{dt} = -x(t) - bf\big(x(t-\tau)\big), \tag{2.43}$$

where $b = \frac{R_7}{R_6}$ and

$$f\big(x(t-\tau)\big) \equiv f(x_\tau) = -0.5n_1\big(|x(t-\tau)|+x(t-\tau)\big)+m_1\tanh\big(l_1x(t-\tau)\big). \tag{2.44}$$

It is worth noting that Eq. (2.43) (along with Eq. (2.44)) is equivalent to Eq. (2.34) (along with Eq. (2.35)) with $a = 1$, and appropriate choices of n_1, m_1, and l_1.

For the low-pass section, we choose $R_0 \approx 1$ kΩ and $C_0 \approx 100$ nF. For the nonlinear device (ND), we use a 1N4148 diode; the following resistor values are used: $R_1 \approx 10$ kΩ, $R_2 \approx 18.5$ kΩ, $R_3 \approx 12.05$ kΩ, $R_4 \approx 8.25$ kΩ, and $R_5 \approx 10$ kΩ. Figure 2.26 shows the experimentally obtained nonlinearity produced by the nonlinear device (ND). Qualitatively, it is equivalent to the nonlinear function (n1) of Fig. 2.18. The gain of the noninverting amplifier (A3) that follows the ND part is designed with $R_6 \approx 10$ kΩ and variable R_7; R_7 is varied with a potentiometer to

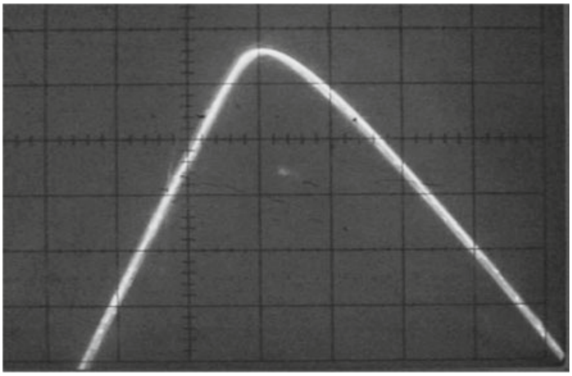

Fig. 2.26 Experimentally obtained nonlinearity produced by the ND part of Fig. 2.25

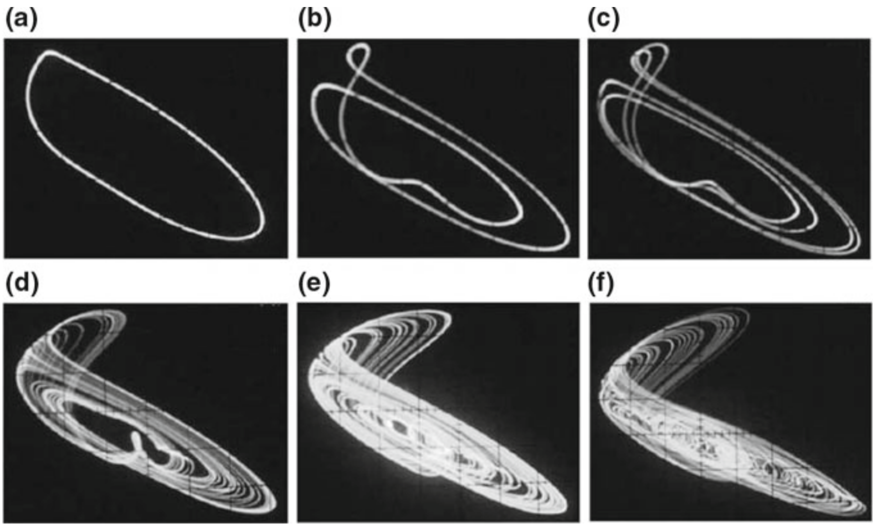

Fig. 2.27 The oscilloscope trace of experimentally obtained phase-plane plots in the $V(t) - V(t - T_D)$ space for variable τ: **a** period-1 at $T_D = 0.15$ ms, **b** period-2 at $T_D = 0.24$ ms, **c** period-4 at $T_D = 0.3$ ms, **d** chaos at $T_D = 0.33$ ms, **e** hyperchaos at $T_D = 0.39$ ms, and **f** hyperchaos at $T_D = 0.44$ ms (for other parameters, see text). V (x-axis): 0.5 v/div; $V(t - T_D)$ (y-axis): 0.5 v/div

change the parameter b. For the delay section, the all-pass filter (APF) is designed with the following parameters: $R \approx 10$ kΩ, $C \approx 10$ nF, and $R_8 = R_9 \approx 2.2$ kΩ. At first, we fix the value of b with $R_7 \approx 17$ kΩ (i.e., $b \approx 1.7$). Now, we vary the delay by varying R. At first, to get a small delay, we use only one APF stage. For $R < 9$ kΩ, the circuit shows a fixed dc value (equilibrium point of the circuit). For $R \geq 9$ kΩ (i.e., $T_D = 0.09$ ms) (approx.), a stable limit cycle appears with a frequency 2380 Hz. Next, we use three blocks of APF; $R \approx 10$ kΩ is taken for the first two blocks (contributing 0.2 ms delay) and vary R of the third block. At $R \approx 3$ kΩ (i.e., $T_D = 0.23$ ms) (approx.), the limit cycle of period-1 loses its stability and a period-2 oscillation emerges. A period-4 behavior is observed at $R \approx 9.5$ kΩ (i.e., $T_D = 0.295$ ms) (approx.). Next, we use four blocks: three blocks have $R \approx 10$ kΩ (contributing a delay of 0.3 ms) and the fourth has $R \approx 1.5$ kΩ (i.e., $T_D = 0.315$ ms), which results in a chaotic oscillation in the circuit. The hyperchaotic attractor is observed beyond $R \approx 7$ kΩ (i.e., $T_D = 0.37$ ms). All the above-mentioned behaviors are shown in Fig. 2.27 (in $V - V(t - T_D)$ space), which depicts the experimental phase-plane plots recorded in an analog oscilloscope.

Next, we set the time delay at $T_D = 0.3$ ms (i.e., $\tau = 3$) by using three APF blocks each having $R \approx 10$ kΩ. To observe the behavior of the system for different b, we vary R_7. For $R_7 \approx 9$ kΩ, the circuit shows a stable limit cycle of frequency 1000 Hz. At $R_7 \approx 16.1$ kΩ, the limit cycle of period-1 loses its stability and a period-2 oscillation emerges. A period-4 behavior is observed at $R_7 \approx 16.71$ kΩ. Chaotic oscillation appears at $R_7 \approx 16.75$ kΩ. Apparently, the circuit enters into

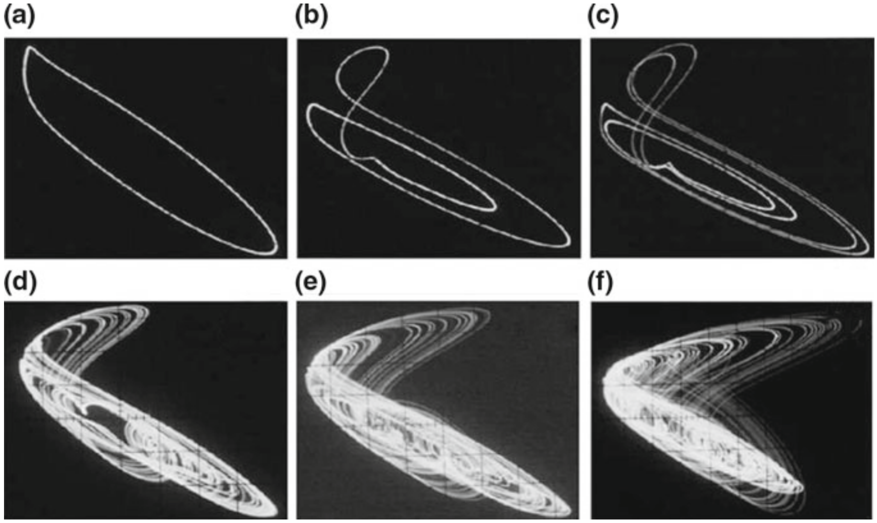

Fig. 2.28 The oscilloscope trace of experimentally obtained phase-plane plots in the $V(t) - V(t - T_D)$ space for variable b: **a** period-1 at $R_7 \approx 12$ kΩ, **b** period-2 at $R_7 \approx 16.4$ kΩ, **c** period-4 at $R_7 \approx 16.72$ kΩ, **d** chaos at $R_7 \approx 16.9$ kΩ, **e** hyperchaos at $R_7 \approx 22.5$ kΩ, and **f** hyperchaos at $R_7 \approx 23.3$ kΩ (for other parameters see text). **a**–**e** V (x-axis): 0.5 v/div; $V(t - T_D)$ (y-axis): 0.5 v/div. **f** V (x-axis): 1 v/div; $V(t - T_D)$ (y-axis): 1 v/div

the hyperchaotic region for $R_7 > 22$ kΩ. With further increase of R_7, the circuit shows a large limit cycle at $R_7 \gtrsim 23.5$ kΩ that indicates the occurrence of boundary crises. All the above-mentioned behaviors (except the large limit cycle) are shown in Fig. 2.28 (in $V - V(t - T_D)$ space), depicting the real-time oscilloscope traces.

2.9 Summary

In this chapter, we have discussed the theory and experiment of two simple first-order time-delayed chaotic systems having single constant delay and two different generic forms of nonlinearities, namely a bimodal and a unimodal nonlinearity. Stability analysis followed by bifurcation analysis established that the systems show a stable limit cycle through a *supercritical Hopf bifurcation*. Detailed numerical simulation proved that with the variation of time delay the systems show a period-doubling route to chaos, hyperchaos, and single scroll or double scroll. Also, if we vary other system parameters keeping the delay constant, the systems show chaotic and hyperchaotic behaviors. The proposed systems have been implemented in analog electronic circuit using off-the-shelf electronic circuit elements. Since a proper choice of system parameters makes the systems hyperchaotic even for a moderate value of time delay, therefore, they can be used as potential hyperchaotic generator for electronic communication applications and chaos-based noise generator systems [5].

Chapter 3
Chaotic Time-Delayed System with Hard Nonlinearity: Design and Characterization

In Chap. 2, we have discussed two chaotic time-delayed systems. However, in those circuits (and other time-delayed chaotic circuits in the literature), the time delay required to obtain limit cycle and chaotic attractor is moderate or large, which affects the frequency and bandwidth of the oscillation obtained from the circuit (large delay implies lower frequency). In this chapter, we discuss a simple nonlinear time-delayed dynamical system having a mathematically closed-form nonlinear function and subsequently, the proposed system is capable of showing limit cycle, chaos, and hyperchaos even for *lower values of intrinsic time delays*.

As far as the nonlinear delay dynamical systems are concerned, the computer-generated numerical analysis alone is not fully reliable, owing to the fact that the simulated model may only describe the system under some trivial initial conditions. Its final state may depend on the choice of *history function* used, the step size of integration, and other factors. Also, due to finite precession and successive approximations, the numerical methods may always contain round-off errors leading to a result far from reality. Since time delay nonlinear systems often show multistability, thus it is advisable to study them using the time series data generated from a real experiment. For these reasons, the experimental verification of the system model is of utmost importance. The dynamical behavior of the system may be obtained best by realizing the electronic analog of it and investigating the time series it produces [138]. Another way to understand the behavior of a nonlinear time-delayed system is to study the harmonic decompositions of the experimental time series of the captured signal through fast Fourier transform (FFT), which provides power spectrum along with subharmonics and ultraharmonics, enabling one to characterize the nonlinear model [107]. In characterizing a nonlinear system, one important measure is the experimental bifurcation diagram, obtained directly from the experiment. This diagram enables one to understand the complete dynamical behavior of the circuit with

D. Biswas and T. Banerjee, *Time-Delayed Chaotic Dynamical Systems*, SpringerBriefs in Nonlinear Circuits,
https://doi.org/10.1007/978-3-319-70993-2_3

the variation of a control parameter. In this chapter, we describe an automated technique of acquiring experimental data, which is controlled through a data acquisition system (DAQ) under LabVIEW [69] environment. Here, we acquire the real-time data through the DAQ system and study the time series waveform, spectral behavior (FFT), phase-plane plots, and the bifurcation diagram.

3.1 System Description

We consider the following first-order nonlinear time-delayed dynamical system:

$$\dot{x} = -ax(t) - bf(x_\tau), \tag{3.1}$$

where a and b are positive parameters. $x_\tau \equiv x(t-\tau)$, $\tau \in \mathscr{R}^+$, is the intrinsic time delay involved in the system. Let us consider the following nonlinear function [20]:

$$f(x_\tau) = -n\,\mathrm{sign}(x_\tau) + m\tanh(lx_\tau), \tag{3.2}$$

where n, m, and l are the parameters controlling the shape of the nonlinear function. The signum (sign$(\cdot)$) function is given by

$$\mathrm{sign}(x_\tau) = \begin{cases} 1, & \text{if } x_\tau > 0 \\ 0, & \text{if } x_\tau = 0 \\ -1, & \text{otherwise} \end{cases} \tag{3.3}$$

In the present case, we consider a particular choice of the nonlinearity that contains a weighted linear combination of $\tanh(\cdot)$ and sign$(\cdot)$ functions. The motivations of considering Eq. (3.2) that contains $\tanh(\cdot)$ and sign$(\cdot)$ function are twofold: first, most of the natural systems show saturation-type nonlinearity. With the variation of a control parameter, saturation may be approached gradually obeying $\tanh(\cdot)$ function, as in the case of magnetization in a para and ferromagnetic system [92], nonideal op-amp [115], activation function in neural network [85], etc. The second type of saturation is a hard saturation described by a signum function sign$(\cdot)$, e.g., binary systems, ideal op-amp characteristics, etc. Thus, it would be of fundamental interest to study their interplay and how they affect the dynamics of a time-delayed system. Second, in experimental realization of the system with analog electronic circuit, it is easy to implement both these nonlinearities and to control them (Fig. 3.1). Further, usage of $\tanh(\cdot)$ function makes the system suitable for implementation in IC design; in IC design, the first stage, which is a differential amplifier, obeys an input–output relation of $\tanh(\cdot)$ nonlinearity [115].

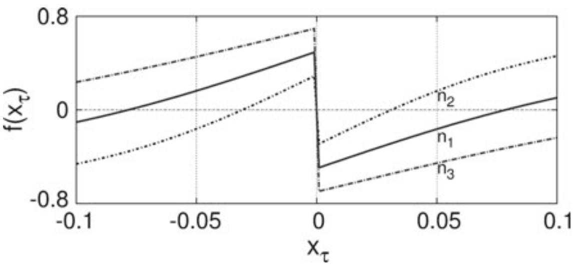

Fig. 3.1 Nonlinearity of the function $f(x_\tau) = -n$ sign $(x_\tau) + m\tanh(lx_\tau)$. (n1) $n = 0.5, m = 1, l = 7$; (n2) $n = 0.3, m = 1, l = 10$; (n3) $n = 0.7, m = 1$, and $l = 5$

3.2 Stability Analysis

We consider the system Eq. (3.1) in the following form:

$$g(x, x_\tau) \equiv \dot{x} = -ax(t) - bf(x_\tau). \tag{3.4}$$

The equilibrium condition for the system implies, $\dot{x} = 0$ and $x(t) = x_\tau = x^*$, i.e., $ax^* = -bf(x^*)$. This is a *transcendental equation* and graphical method has to be used in order to find fixed points. By inspection, one notices that there exists *three equilibrium points*, namely, $x^* = 0$, $x^* = p_1$, and $x^* = p_2$. The point $x^* = 0$ is a trivial fixed point and $p_{1,2}$ are nontrivial fixed points. By the symmetry of the equation, we get $|p_1| = |p_2|$. The trajectory of the equilibrium points with the variation of the parameter b is shown in Fig. 3.2 (Left panel). The points p_1 and p_2 are marked in the figure given by $|p_1| = |p_2| = 0.046$ for $b = 0.245, n = 0.5, m = 1$, and $l = 7$. The following analysis enables us to find the value of τ for which Hopf bifurcation occurs.[1] We define $J_0 = \frac{\partial g(x,x_\tau)}{\partial x} = -a$ and $J_\tau\big|_{x_\tau = x^*} = -bml\,\mathrm{sech}^2(lx^*)$. Now the *characteristic equation* is given by $J_0 + J_\tau e^{-\lambda\tau} - \lambda = 0$, which reads

$$\lambda = -a - bml\,\mathrm{sech}^2(lx^*)e^{-\lambda\tau}. \tag{3.5}$$

The roots of Eq. (3.5) are written as $\lambda = \mu + i\nu$ and we will show that the system is asymptotically stable for some conditions with $\tau \in [0, \tau_k)$.

---

[1] It is important to note that, unlike ordinary differential equations (ODE), the condition of existence and uniqueness of limit cycle in delay differential equations is not necessarily determined by the Lipschitz condition, but it has been discussed in the literature [38, 130] that there exist limit cycles in a time-delayed system even if the system is discontinuous. In Ref. [130], it has been shown that the existence of solutions of functional differential equation with discontinuous nonlinearity exists. Reference [38] proved that the nonlinearity in delay differential equations need not be continuous or monotone to have existence of limit cycle.

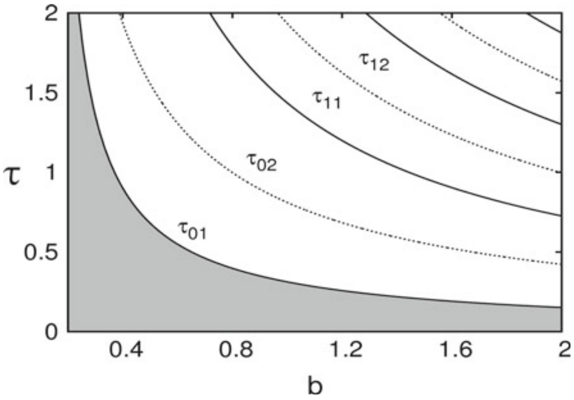

Fig. 3.2 Stability diagram in $b - \tau$ space. The shaded region indicates the stable zone. Other parameters are $n = 0.5$, $m = 1$, and $l = 7$

Stability for $\tau = 0$

For $\tau = 0$, we analyze the stability of the system following the steps done in Sect. 2.2.1 (p. 12). The condition of stability reads the following condition:

$$a > -bml \operatorname{sech}^2(lx^*). \tag{3.6}$$

Stability for $\tau \neq 0$

In the presence of time delay (i.e., $\tau \neq 0$), the system looses its stability and oscillatory behavior starts through the occurrence of Hopf bifurcation. The stability condition may be obtained by the method followed in Sect. 2.2.1. We get the equations of delay as

$$\tau_{k1} = \frac{\left[\cos^{-1}(-\frac{J_0}{J_\tau}) + 2k\pi\right]}{\sqrt{{J_\tau}^2 - {J_0}^2}}, \quad \text{for } J_\tau < 0, \tag{3.7}$$

and

$$\tau_{k2} = \frac{\left[\left(2\pi - \cos^{-1}(-\frac{J_0}{J_\tau})\right) + 2k\pi\right]}{\sqrt{{J_\tau}^2 - {J_0}^2}}, \quad \text{for } J_\tau > 0, \tag{3.8}$$

where $k = 0, 1, 2, \ldots$ The condition of stability of the system reads in the following form:

$$|bml\operatorname{sech}^2(lx^*)| > |a|. \tag{3.9}$$

Also, we get the derivative of the real part of the eigenvalue as

$$\mu'(\tau_k) = \frac{{\nu_0}^2}{(1 + \tau_k a)^2 + \tau_k^2 \nu_0^2} > 0. \tag{3.10}$$

For all values of above-mentioned x^*, Eq. (3.10) is valid. So we conclude that the stable state lies between $\tau = 0$ and τ_{01}.

Next, we investigate the stability for the following set of parameter values: $a = 1$, $n = 0.5$, $m = 1$, and $l = 7$, the resulting nonlinearity for this case is shown in curve “n1” of Fig. 3.1. The stability in the $\tau - b$ space is shown in Fig. 3.2. The shaded region represents the stable steady states.

3.2.1 Stability and Direction of Hopf Bifurcation

From the previous subsection, we see that the Hopf bifurcation occurs at $\tau = \tau_{01}$. We know that, under the hypothesis $-bf'(x^*) < a$, all the characteristic values, except $\pm i\nu_0$, have negative real parts, when $\tau = \tau_{01}$. In this section, we study the direction of Hopf bifurcation and the stability of the bifurcating solutions, when $\tau = \tau_{01}$, using the techniques described in [144] and done in Sect. 2.2.1 (p. 12). We refer to Eq. 2.25 (p. 12) for different quantities that confirm the following bifurcation conditions. It has been shown in [144] that μ_2 determines the direction of the Hopf bifurcation: if $\mu_2 > 0$ ($\mu_2 < 0$), then the Hopf bifurcation is *supercritical (subcritical)* and the bifurcating periodic solutions exist for $\tau > \tau_{01}$ ($\tau < \tau_{01}$). Further, the bifurcating periodic solutions are orbitally asymptotically *stable (unstable)* if $\beta_2 < 0$ ($\beta_2 > 0$). Finally, T_2 determines the period of bifurcating periodic solutions: the period *increases (decreases)* if $T_2 > 0$ ($T_2 < 0$).

To test the validity of our analysis, let us use the following parameter values: $a = 1$, $n = 0.5$, $m = 1$, and $l = 7$. For $b = 0.5$, we have $p_1 = 0.0578$, which results in $J_0 = -a = -1$ and $J_\tau = -bml\,\text{sech}^2(\pm l p_1) = -2.984$. Thus, we see that $|J_\tau| \geq |J_0|$ (satisfying the condition of stability). Also, at these parameter values, we have $\tau_{01} = 0.68$ (from Eq. (3.7), p.44). Thus, at $b = 0.5$ and $\tau_{01} = \tau_H = 0.68$, the fixed point losses its stability through Hopf bifurcation. Further, at these parameter values, we have $g_{11} = 2.828 - 3.219i$, $g_{20} = -0.16 + 4.282i$, $g_{02} = -4.226 + 0.71i$, $g_{21} = -26.331 - 4.045i$, $E_1 = 1.59 + 1.378i$, $E_2 = 4.025$, $W_{20} = 0.338 - 1.05i$, $W_{11} = 5.435 - 1.998i$, and $c_1 = -16.467 - 6.538i$. Using these set of values in Eq. (2.25), we have $\mu_2 = 13.499 > 0$; that means the resulting bifurcation is a *supercritical* Hopf bifurcation. Also, $\beta_2 = -32.934 < 0$; thus, the bifurcating periodic solutions are orbitally asymptotically stable. Finally, since $T_2 = 17.026 > 0$, the period of the limit cycle increases with increasing τ.

3.3 Numerical Studies

The system Eq. (3.1) is numerically investigated using the fourth-order Runge–Kutta algorithm using a step size $h = 0.005$. A large number of initial transients have been left out in the investigation to represent the stable dynamics in the numerical results. The initial condition is kept $\phi(t) = 0.8$ for $t \in [-\tau, 0]$ throughout the investigation (we have chosen other initial conditions also but the steady-state results remain same for all the cases). In all the cases, we consider the following parameter values: $a = 1$, $n = 0.5$, $m = 1$, and $l = 7$.

3.3.1 *Varying* b *with Constant* τ

We consider the variation of parameter b, keeping the intrinsic delay to a suitable constant value $\tau = 2$. The variation of b showed a rich dynamics in the system. Figure 3.3 shows the outcomes of this investigation. The left column in this figure shows the time series $(x(t), x(t-\tau)-t)$ and the right column shows the phase-plane $(x(t)-x(t-\tau))$ plots. The fixed point loses its stability for $b = 0.245$ and period-1

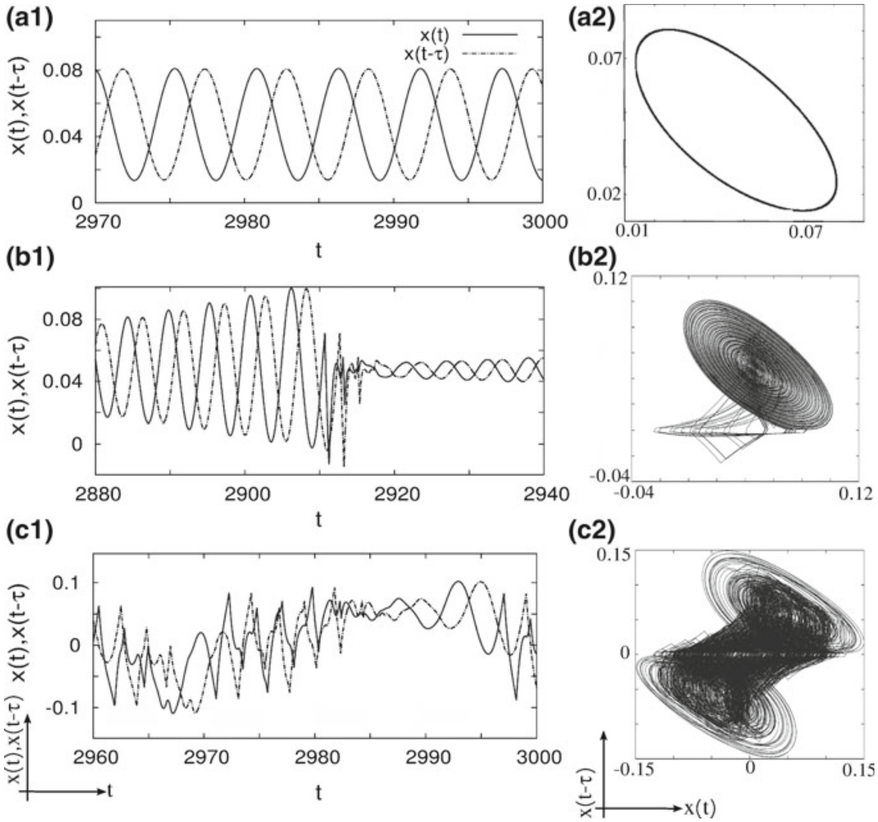

Fig. 3.3 The time series (Left column) and phase-plane plots (Right column) in $x(t) - x(t-\tau)$ space for variable b and constant τ. (a1-a2) Period-1 (P1) for $b = 0.245$, (b1-b2) chaos for $b = 0.25$, and (c1-c2) double-scroll hyperchaos for $b = 0.4$. Other parameters are $a = 1$, $n = 0.5$, $m = 1$, $l = 7$, and $\tau = 2$

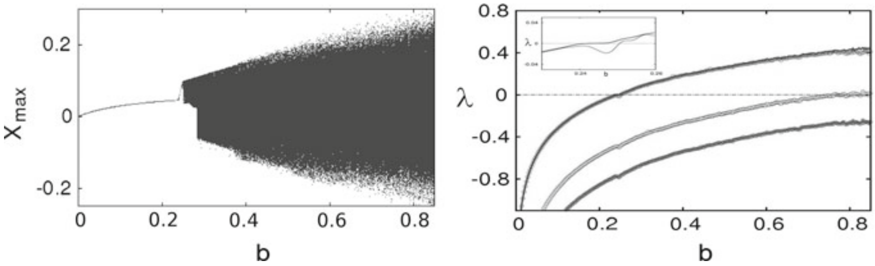

Fig. 3.4 (Left panel) The bifurcation diagram of the system with variable b and constant $\tau = 2$. (Right panel) First six Lyapunov exponent (LE) spectrums. The inner panel shows the zoomed portion where the LEs cross zero. Other parameters are $a = 1$, $n = 0.5$, $m = 1$, and $l = 7$

(P1) limit cycle emerges. The situation is shown in Fig. 3.3(a1–a2). Further, increase in b makes the system chaotic. The single-scroll chaotic attractor for $b = 0.25$ is shown in Fig. 3.3(b1–b2). The system eventually enters the hyperchaotic regime for $b \geq 0.25$. Finally, the system depicts two scroll hyperchaos for $b \geq 0.287$. The situation for $b = 0.4$ is shown in Fig. 3.3(c1-c2). The corresponding bifurcation diagram in b space is shown in Fig. 3.4 (Left panel). The bifurcation diagram is plotted using the local maxima of x, after discarding a large number of transients. All the observed phenomena have been summarized in the bifurcation diagram. The occurrence of Hopf bifurcation at $b = 0.245$ is confirmed in this figure.

For the quantitative measurement of the system dynamics, we calculate the Lyapunov exponent (LE) spectrum. The process for calculating the LEs is adopted from the algorithm of Ref. [37]. Figure 3.4 (Right panel) shows the first six LEs for the system, which agrees with the bifurcation diagram. The multiple positive LEs *along with the occurrence of a strange attractor* confirms the presence of hyperchaos in the system [72].

3.3.2 *Varying* τ *with Constant* b

The effect of variation of τ with fixed b is considered by fixing $b = 0.5$ and varying the intrinsic delay τ in the system. The outcomes of this investigation are shown in Fig. 3.5. The left column in this figure shows the time series and the right column shows the phase-plane plots. The system undergoes a supercritical Hopf bifurcation at $\tau = 0.68$ and the stability of the fixed point is lost resulting a limit cycle oscillation. The P1 limit cycle for $\tau = 0.69$ is shown in Fig. 3.5(a1). The corresponding phase-plane plot in $x(t) - x(t - \tau)$ is shown in Fig. 3.5(a2). The system eventually enters the chaotic regime for $\tau \geq 0.72$. In Fig. 3.5(b1, b2), we show the real-time and phase-plane plots for $\tau = 0.8$, respectively. The system shows double-scroll hyperchaotic oscillations for $\tau \geq 0.82$. The scenario for $\tau = 2$ is shown in Fig. 3.5(c1, c2).

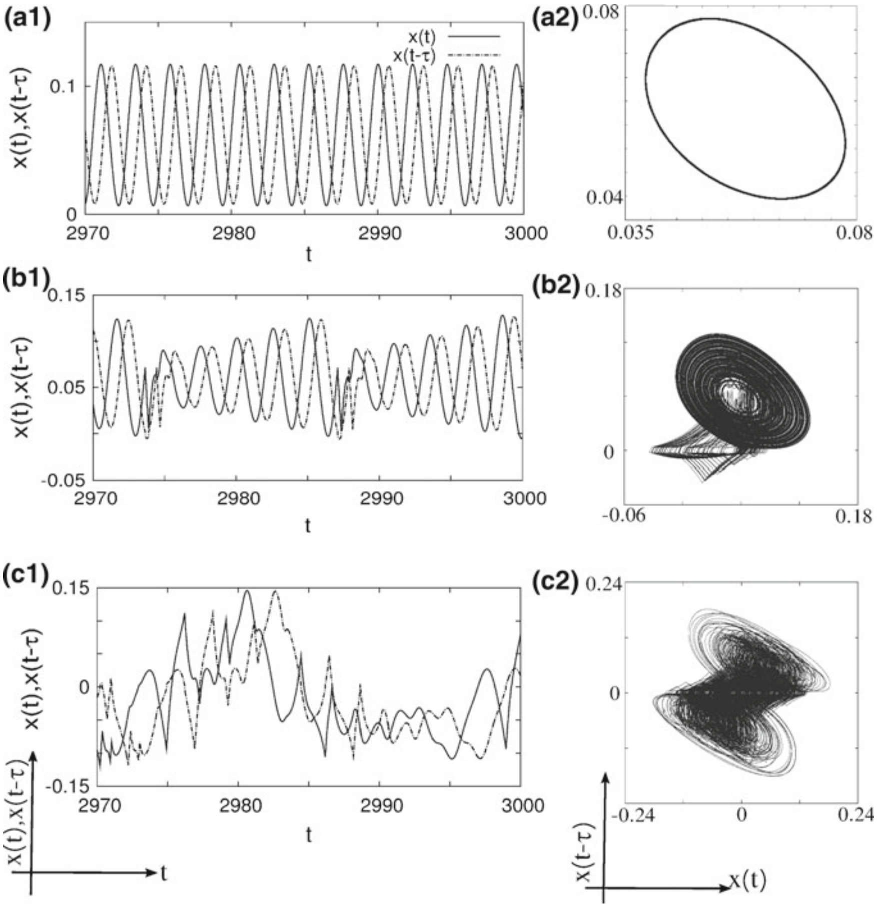

Fig. 3.5 Time series (Left column) and phase-plane plots (Right column) for variable τ and fixed b. (a1, a2) P1 oscillation for $\tau = 0.69$, (b1, b2) single-scroll chaos for $\tau = 0.8$, (c1, c2) double-scroll hyperchaos for $\tau = 2$. Other parameters are $a = 1$, $n = 0.5$, $m = 1$, $l = 7$, and $b = 0.5$

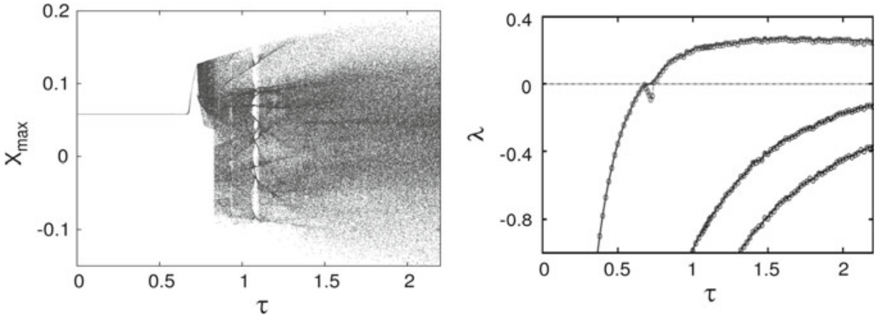

Fig. 3.6 (Left panel) Bifurcation diagram for varying τ and constant b, (Right panel) Lyapunov exponent spectrum. Other parameters are $a = 1$, $n = 0.5$, $m = 1$, $l = 7$, and $b = 0.5$

The dynamics of the system is summarized in the bifurcation diagram of Fig. 3.6 (Left panel). The Lyapunov exponent spectrum is shown in Fig. 3.6 (right panel). The bifurcation diagram and LE spectrum support the scenario observed above.

3.4 Electronic Circuit Realization

We experimentally implement the system Eq. (3.1) in an electronic circuit. The experimental circuit diagram is shown in Fig. 3.7. The circuit is built using IC TL074 (quad JFET op-amp), IC AD633 (voltage multiplier chip), and a ±15 volt power supply. All the resistors (capacitors) used have 5% (1%) tolerance. The LPF section consists of $R_0 \approx 1$ kΩ and $C_0 \approx 0.1$ μF. The ND part consists of the following parameter values: $R_1 \approx 22$ kΩ, $R_2 \approx 3.75$ kΩ, $R_3 \approx 10$ kΩ, $R_4 \approx 97.3$ kΩ, and $R_5 \approx 10$ kΩ. Let us consider the voltage drop across the capacitor C_0 of the first-order low-pass filter section $R_0 - C_0$ be $V(t)$, then the equation of the circuit is given by

$$R_0 C_0 \frac{dV(t)}{dt} = -V(t) - \frac{R_7}{R_6} f\big(V(t - T_D)\big). \tag{3.11}$$

In Fig. 3.7, the ND part represents the proposed nonlinearity, achieved by the op-amps A1–A3. The inverting amplifier section obtained by op-amp A4 provides the required gain in the system. The delay part is obtained through an active all-pass filter (AFP) blocks. We use buffers wherever they are needed.

Here, $f\big(V(t - T_D)\big) \equiv f(V_\tau)$ is the nonlinear function of system. T_D is the delay offered by the delay blocks. The nonlinearity is the result of the two terms, namely, (i) the signum function (sign($\cdot$)) is obtained by an op-amp (A2) without any feedback and (ii) the tanh($\cdot$) function obtained by the op-amp (A1) as

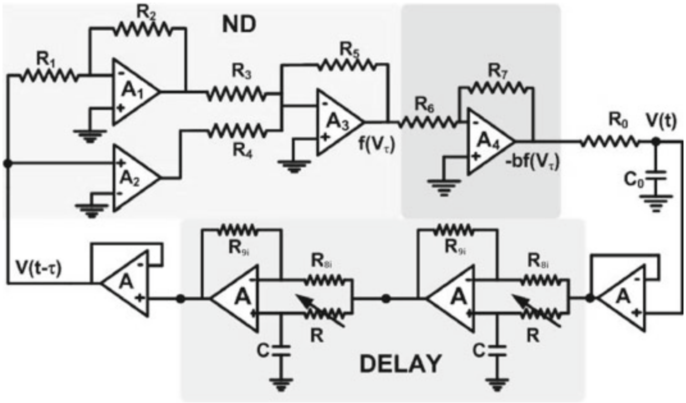

Fig. 3.7 Experimental electronic circuit diagram. ND is the nonlinear device and DELAY is the delay block produced using the active All-Pass filters

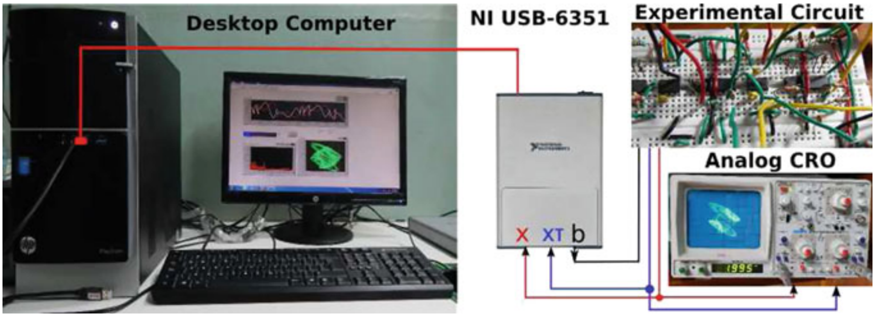

Fig. 3.8 Experimental arrangement showing the interface between the hardware circuit and desktop computer through NI DAQ (USB-6351) and LabVIEW

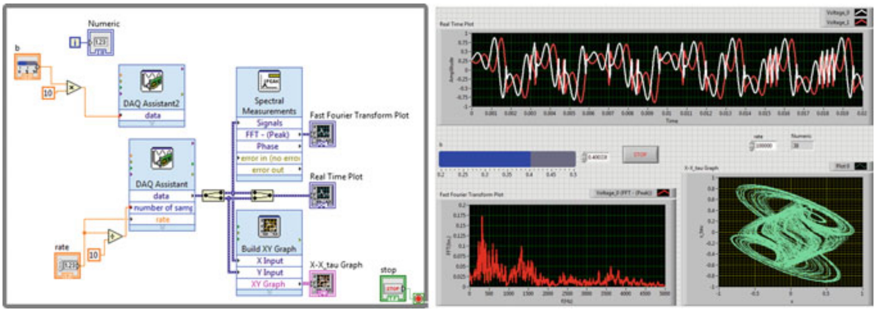

Fig. 3.9 (Left panel) The block diagram and (Right panel) front panel of the NI LabVIEW DAQ. In the figure, we show real-time plot, FFT, phase-plane plot. The circuit is controlled from computer through NI DAQ and LabVIEW through the variation of b. The signal sampling rate is 100000 dps

$$-\beta V_{sat} \tanh\left(\omega \frac{R_2}{R_1} \frac{V(t-T_D)}{V_{sat}}\right),$$

where β and ω are the scaling factors to fit the model with the experimental data. For smaller voltages, one can approximate $\beta \approx 1$ and $\omega \approx 1$, (iii) the opamap (A3) acts as a weighted adder to produce the required nonlinearity of the system.

Hence, the nonlinearity of the system is represented as

$$f\big(V(t-T_D)\big) = -\frac{R_5}{R_4}\,\mathrm{sign}\left(\frac{V(t-T_D)}{V_{sat}}\right) + \frac{R_5}{R_3}\beta V_{sat} \tanh\left(\omega \frac{R_2}{R_1} \frac{V(t-T_D)}{V_{sat}}\right). \tag{3.12}$$

We design the proposed circuit in the hardware in a breadboard and control it with a NI data acquisition (DAQ) system using the LabVIEW interface. The representative experimental setup is shown in Fig. 3.8. The block diagram and front panel of the LabVIEW NI DAQ interface for a set of exemplary circuit parameters is shown in Fig. 3.9. The block diagram is a set of some instructions in the form of graphical

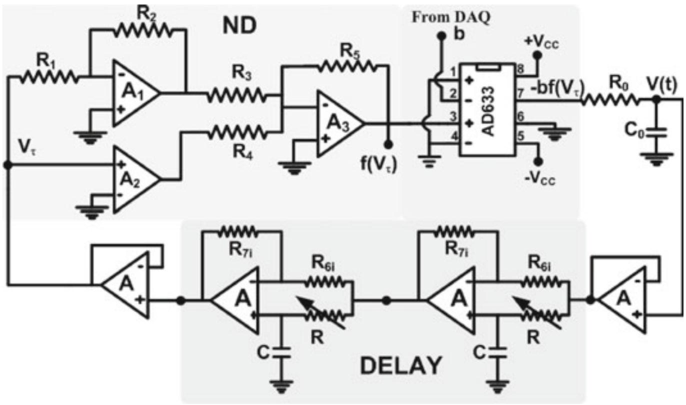

Fig. 3.10 Experimental electronic circuit diagram modified for controlling *b* from computer using NI DAQ with LabVIEW interface (For resistor and capacitor values, see text)

program elements, and the front panel shows the outcomes of the block diagram. The variable delay part consists of all-pass filter (APF) [115] with delay $T_D = iRC$ $(i = 1, 2, 3, \ldots)$.

To control the system through a computer interface, we introduce some modifications in the circuit. Figure 3.7 is modified such that we can *control* the parameter *b* [i.e., the gain of A4] by using DAQ system. We use Natinal Instrument (NI) DAQ NI USB–6351 (8 input, 2 output, maximum sampling rate 1.25 MS/s). For this purpose, we build the circuit as shown in Fig. 3.10; here, the gain (i.e., A4 amplifier of Fig. 3.7) is replaced by a voltage multiplier chip AD633JN in Fig. 3.10. The output of this chip is given by

$$X_7 = \frac{(X_1 - X_2)(X_3 - X_4)}{10} + X_6,$$

where X_i's are the voltages at the different terminals of the chip, with $i = 1, 2, \ldots, 8$. By the inclusion of this chip, one can control the parameter *b* by simply varying the voltage level in the output port of the NI DAQ through computer interface. To make Eq. (3.11) a dimensionless one, we define the following dimensionless quantities: $t = \frac{t}{R_0C_0}$, $\tau = \frac{T_D}{R_0C_0}$, $x = \frac{V(t)}{V_{sat}}$, $x(t-\tau) = \frac{V(t-T_D)}{V_{sat}}$, $b = \frac{R_7}{R_6}$, $\frac{R_5}{R_4} = n_1$, $\beta\frac{R_5}{R_3} = m_1$, and $\omega\frac{R_2}{R_1} = l_1$. With these, Eq. (3.11) reads the form

$$\frac{dx(t)}{dt} = -x(t) - bf\big(x(t-\tau)\big), \tag{3.13}$$

with

$$f\big(x(t-\tau)\big) \equiv f(x_\tau) = -n_1\mathrm{sign}\big(x(t-\tau)\big) + m_1\tanh\big(l_1x(t-\tau)\big). \tag{3.14}$$

Equations (3.13) and (3.14) are exactly equivalent to Eqs. (3.1) and (3.2), respectively, with $a = 1$ and appropriate choices of n_1, m_1, and l_1.

3.5 Experimental Results

We design the proposed circuit in the hardware in a breadboard and control it with a NI Data Acquisition (DAQ) system using the LabVIEW interface. The parameter b is controlled by the NI DAQ system through a desktop computer. It is fed to the multiplier chip in the circuit. The experimental nonlinearity produced by the ND part of Fig. 3.10 is shown in Fig. 3.11. One can observe the well analogy with that obtained numerically (Fig. 3.1). The delay portion has $R_{6i} = R_{7i} \approx 2.2\,\mathrm{k}\Omega$, $C \approx 10$ nF, and $R \approx 10\,\mathrm{k}\Omega$. Thus, each AFP part contributes a delay of $T_D \approx RC = 0.1$ ms, which, when dimensionalized, gives $\tau \approx \frac{RC}{R_0 C_0} = 1$. The effect of variable τ may be obtained by the variation of R in the APF blocks.

Variable b, ***Fixed*** τ

In this part, we vary the parameter b through the NI DAQ via LabVIEW by keeping the intrinsic delay term fixed to $\tau \approx 2$ by selecting two stages of APFs with $R = 10\,\mathrm{k}\Omega$. The variation of b produced the rich dynamics that is shown in Fig. 3.12. The system loses its stability at $b = 0.21$ through Hopf bifurcation and period-1 (P1) limit cycle emerges. The situation for $b = 0.23$ is shown in Fig. 3.12(a1-a3). Figure 3.12(a1) shows the time series plots, and Fig. 3.12(a2) shows the Fast Fourier Transform (FFT) of the time series. The presence of a single peak around $f = 1150$ Hz confirms a period-1 limit cycle oscillation in the system. Figure 3.12(a3) shows the phase-plane plots in $x(t) - x(t - \tau)$ space. Figure 3.12(b1-b3) shows the single-scroll chaos in the system for $b = 0.26$. The continuous nature of the FFT is confirmatory for the chaotic oscillation. The phase-plane

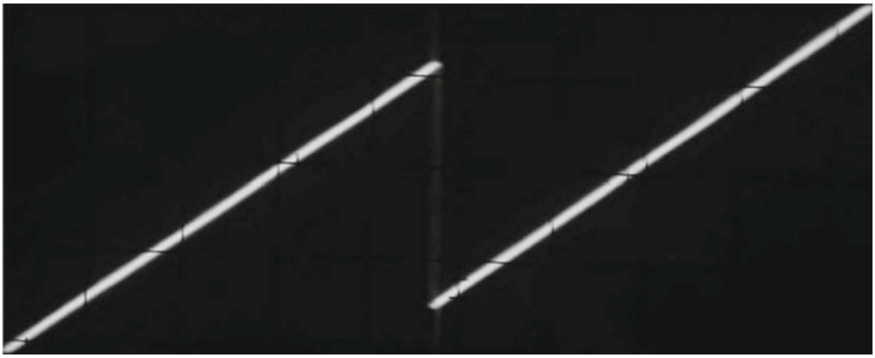

Fig. 3.11 The experimental nonlinearity produced by the ND part of Fig. 3.10. For other parameters, see text. Scale: x-axis=50 mV/div, y-axis=0.2 V/div

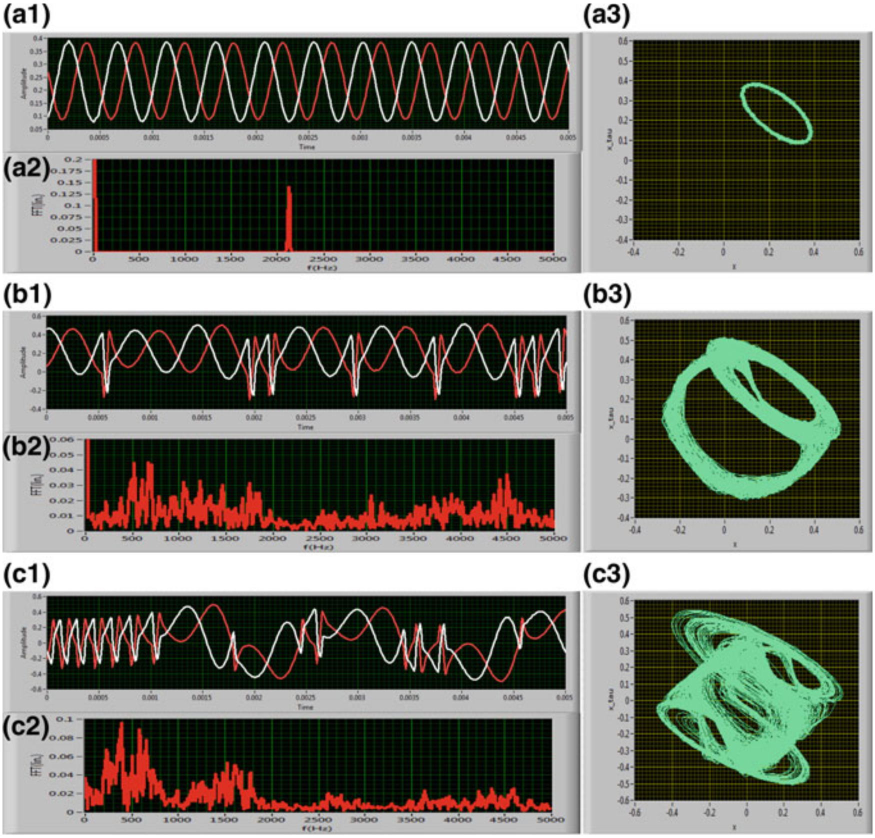

Fig. 3.12 Experimental time series (a1, b1, c1), fast Fourier transform (FFT), (a2, b2, c2) and phase-plane plots (a3, b3, c3) for variable b and constant $\tau = 2$. (a1-a3) limit cycle oscillation for $b = 0.23$, (b1-b3) single-scroll chaos for $b = 0.26$, and (c1-c3) double-scroll attractor for $b = 0.4$ (For other parameters, see text)

plots in Fig. 3.12(b3) again confirm the presence of chaos for this parameter value. Finally, the system emerges double-scroll hyperchaotic oscillations for $b \geq 0.28$. The double-scroll hyperchaos for $b = 0.4$ is shown in Fig. 3.12(c1-c3). The time series in Fig. 3.12(c1) shows hyperchaotic nature. The FFT (Fig. 3.12(c2)) confirms this owing to its continuous nature. The phase-plane plot in Fig. 3.12(c3) confirms the much complex double-scroll hyperchaos in the system.

To confirm the aforesaid observations, we draw the *experimental* bifurcation diagrams by detecting the local maxima in $V(t)$. For this purpose, we write a program in LabVIEW which automatically varies b in an preassigned step size, detects the local maxima of $V(t)$, stores the values in two-dimensional array, and plots the experimental bifurcation diagram. The graphical program for the bifurcation diagram is shown in Fig. 3.13. Much care is taken in leaving the transients in the system. The

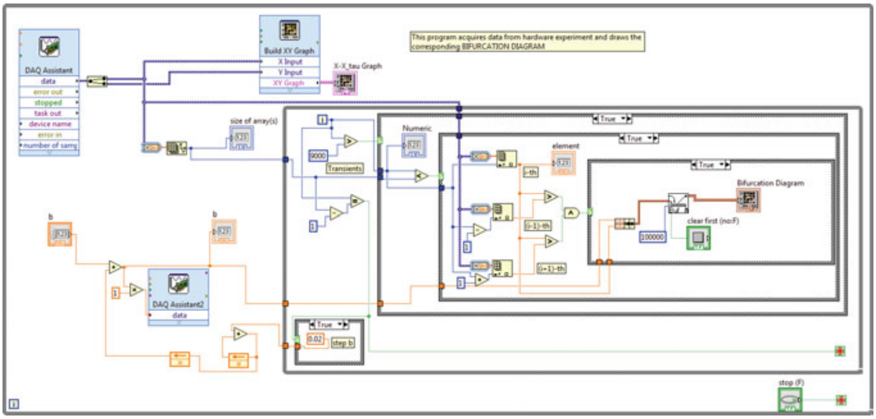

This program acquires data from hardware experiment and draws the corresponding BIFURCATION DIAGRAM

Fig. 3.13 The front panel of the graphical program for the bifurcation diagram to automatically increase the variable b and store data in a computer and plot them

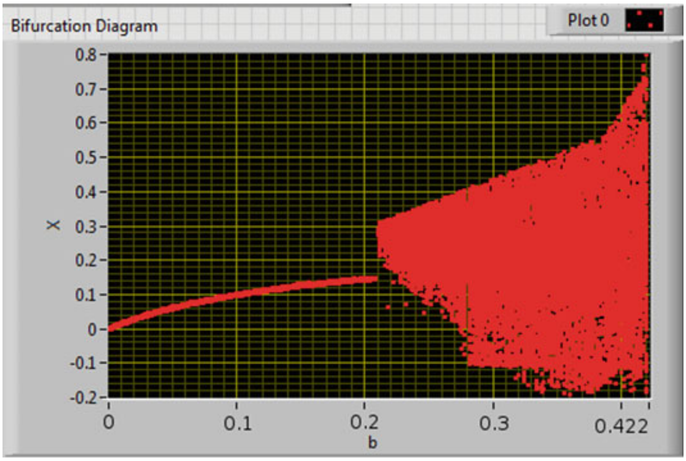

Fig. 3.14 The experimental bifurcation diagram with variable b. For other parameters, see text

experimental bifurcation diagram is shown in Fig. 3.14. The plot closely resembles the numerically obtained bifurcation diagram of Fig. 3.4 (p. 47).

Variable τ, *Fixed* b

Next, we vary the intrinsic time delay τ by fixing the parameter b. For this purpose, we fix b at $b = 0.5$ and keep all other resistor and capacitor values the same as the previous ones. The system looses its stability for $\tau \approx 0.7$. The situation for $\tau \approx 0.75$ is shown in Fig. 3.15(a1-a3). This particular value of τ is obtained by using only one APF stage with $R \approx 7.5\ \mathrm{k}\Omega$. Figure 3.15(a1) shows the real-time plots, (a2) shows the FFT of the time series, and (a3) shows the phase plane plot obtained by NI DAQ.

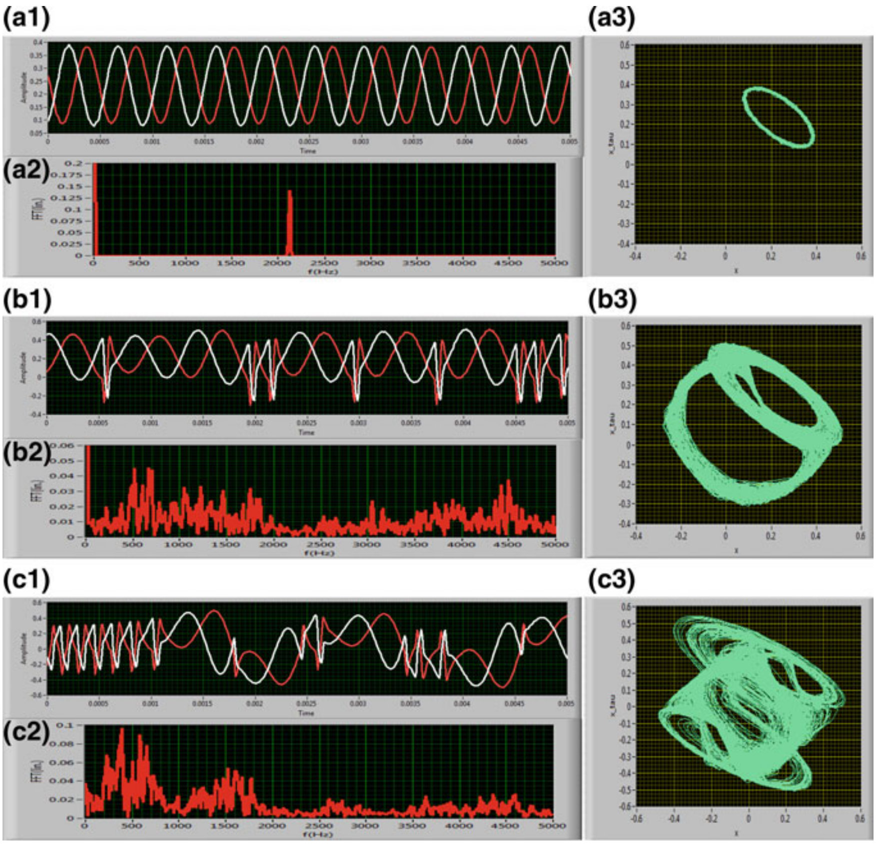

Fig. 3.15 Experimental time series (a1, b1, c1), fast Fourier transform (FFT) (a2, b2, c2), and phase-plane plots (a3, b3, c3) for variable τ with constant $b = 0.5$. (a1-a3) limit cycle oscillation for $\tau \approx 0.75$, (b1-b3) Single-scroll chaos for $\tau \approx 0.85$, and (c1-c3) Double-scroll for $\tau \approx 2$ (For other parameters, see text)

The system enters the chaotic regime for $\tau \approx 0.78$. The situation for $\tau \approx 0.85$ is shown in Fig. 3.15(b1-b3). Further increase in τ causes the system to enter the regime of double-scroll hyperchaos at $\tau \approx 0.93$. The scenario for $\tau \approx 2$ is shown in Fig. 3.15(c1-c3). The continuous nature of the FFT along with the time series and phase-plane plots confirm the double-scroll hyperchaos in the system. Finally, we also show the double-scroll attractor for $b = 0.4$, $\tau = 2$, and $b = 0.5$, $\tau \approx 1.6$ in Fig. 3.16, which are obtained by snapshots from an analog CRO.

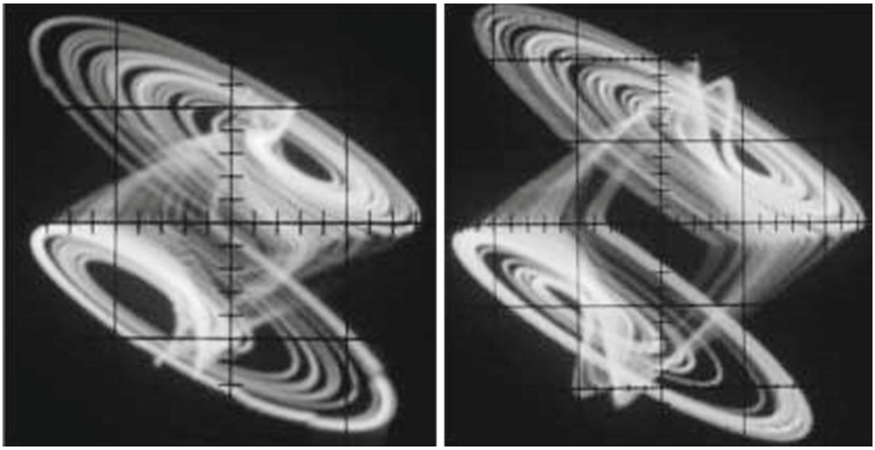

Fig. 3.16 Snapshots of double-scroll attractors obtained from an analog CRO. (Left panel) $b = 0.4$, $\tau = 2$; and (Right panel) $b = 0.5$, $\tau \approx 1.6$. Scale div. x-axis=0.2 V/div, y-axis=0.2 V/div

3.6 Discussions

In this chapter, we have reported the first-order time-delayed chaotic and hyperchaotic system and characterized its dynamics with *experimentally acquired* time series data. The stability and bifurcation of the system are analyzed to show that the system emerges limit cycle for very low value of time delay. The bifurcation analysis shows that the system experiences *supercritical* Hopf bifurcation to give rise to a limit cycle oscillation beyond a certain time delay. The system is numerically simulated to study the chaotic and hyperchaotic attractors. The bifurcation diagrams under different parameter variations are drawn. The system is realized in electronic circuit in the hardware-level experiment. The signals from the experimental circuit is interfaced with a NI Data Acquisition system (DAQ) and processed in LabVIEW environment. The LabVIEW is programmed to acquire the time series waveform, the fast Fourier transform (FFT), the phase-plane plots, and the experimental bifurcation diagrams from the experimental time series data.

The following interesting features of the discussed system and the circuit are to be noticed, which may play important role from the perspective of *practical applications*: (i) With the suitable choice of the parameters, the system shows chaotic or hyperchaotic behavior for a *very small value of time delay*. Thus, the system can be used as an efficient chaos or hyperchaos generator for electronic communication applications, chaos-based noise generator systems, and chaotic cryptography. (ii) Since the system is capable of producing limit cycle for a small value of time delay, it may be a good candidate to generate high-frequency oscillations.

Chapter 4
Collective Behavior-I: Synchronization in Hyperchaotic Time-Delayed Oscillators Coupled Through a Common Environment

Collective behaviors of coupled dynamical systems are of significant interest in the field of physical and biological sciences, and engineering [96]. The prominent collective behaviors that occur in periodic and chaotic systems are synchronization and phase locking [96], oscillation suppression [10, 15, 16, 47, 63, 112], chimera states [9, 91, 113], etc. We have already discussed in Chap. 1 that synchronization of chaos in time-delayed chaotic system was reported much later by Pyragas [100] (1998) than its discovery in low-dimensional chaotic systems [93] (in 1990). In all the research works discussed in Chap. 1 (Sect. 1.2, p. 5), the coupling schemes were essentially the *direct coupling*, i.e., either unidirectional coupling or bidirectional coupling, where either of the two coupled systems or both the systems directly affect the dynamics of each other.

In this chapter, we discuss the synchronization scenarios of two hyperchaotic time-delayed oscillators that are coupled indirectly via a common environment. This coupling scheme was originally proposed by Resmi et al. [106] in low-dimensional systems. Later, Banerjee and Biswas [11] extended the study to time-delayed systems. Here, we show that depending upon the coupling parameters a hyperchaotic time-delayed system can show in-phase or complete synchronization, and also inverse-phase or anti-synchronization. We confirm the occurrence of phase synchronization in the coupled system through the dynamical measures like generalized autocorrelation function, correlation of probability of recurrence [81, 108], and the concept of localized sets [95] computed directly from the experimental time series data. We also perform a linear stability analysis of the coupled system for the complete and anti-synchronized cases.

D. Biswas and T. Banerjee, *Time-Delayed Chaotic Dynamical Systems*, SpringerBriefs in Nonlinear Circuits,
https://doi.org/10.1007/978-3-319-70993-2_4

4.1 Environmentally Coupled Time-Delayed System

Let us consider two first-order identical time-delayed systems coupled indirectly through a common environment z. The mathematical model of the coupled system, in general, is given by

$$\dot{x} = -ax + b_1 f(x_\tau) + \varepsilon_1 \beta_1 z, \tag{4.1a}$$

$$\dot{y} = -ay + b_2 f(y_\tau) + \varepsilon_1 \beta_2 z, \tag{4.1b}$$

$$\dot{z} = -\kappa z - \frac{\varepsilon_2}{2}(\beta_1 x + \beta_2 y), \tag{4.1c}$$

where $a > 0$, b_1 and b_2 are called the feedback rates for the x-system and y-system, respectively. Also, $u \equiv u(t)$ and $u_\tau \equiv u(t-\tau)$ $(u = x, y)$, where $\tau \in \mathcal{R}^+$ is a constant time delay. ϵ_1 determines the coupling strength that controls the effect of environment on the systems. ϵ_2 determines the coupling strength that controls the effect of individual systems on the environment. β_1 and β_2 determine the nature of coupling: for $\beta_1 = 1, \beta_2 = -1$, the systems are attractively coupled; on the other hand, repulsive coupling is achieved for $\beta_1 = 1$ and $\beta_2 = 1$. Finally, κ (> 0) determines the nature of the environment; in absence of both the x- and y-systems (i.e., $\epsilon_2 = 0$), the environment decays toward the zero steady state and remains in that dormant state. In the following, for Eq. (4.1), we consider the bimodal nonlinear function discussed in Eq. 2.2 (Chap. 2, p. 11) indirect coupling via1),

$$f(u_\tau) = -nu_\tau + m\tanh(lu_\tau). \tag{4.2}$$

4.2 Experiment

4.2.1 Electronic Circuit Realization

We implement the coupled system given by Eq. (4.1) in an analog electronic circuit. Figure 4.1 shows the representative diagram of the experimental circuit. The circuit consists of three distinct parts, namely, the *x-system*, the *y-system*, and the *z-system* or the *environment*. The circuit of nonlinear device (ND) of each systems is given in Fig. 4.2; delay block is realized by using active all-pass filters (APF) shown in Fig. 2.13 (p. 26). To achieve the indirect coupling via environment, we feed the outputs from the $R_0 - C_0$ junctions of the x- and y-systems to the inverting terminal of the op-amp A5, which acts as an integrator, through buffers (for impedance matching) and resistors R_{11x} and R_{11y}, which determine the parameter ϵ_2. The voltage from the $R_0 - C_0$ terminal of the y-system can be inverted for the in-phase coupling (i.e., $\beta_1 = 1, \beta_2 = -1$) by the use of an unity gain inverter and connecting the points "D" and "E", where for inverse-phase coupling ($\beta_1 = 1, \beta_2 = 1$), terminals "D" and "F" will be connected. The output of the integrator A5 is fed into the inverting

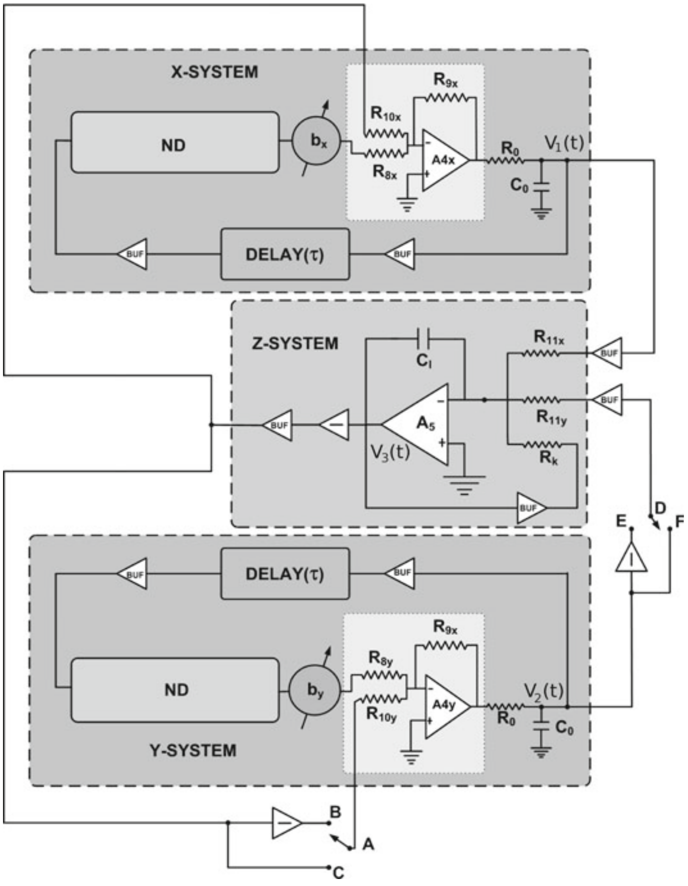

Fig. 4.1 Experimental circuit diagram of the coupled system. $R_0 = 1$ kΩ, $C_0 = 0.1$ μF, $C_I = 0.1$ μF. Buffers are designed with the unity gain non-inverting operational amplifiers. $b_{x,y}$ are amplifiers and ND represents nonlinear device (see Fig. 4.2). A4x,y op-amps are used as inverting adder and A5 op-amp is used as inverting integrator. All the op-amps are TL074. $R_k = 1$ kΩ, $R_{8x,y} = R_{9x,y} = 1$ kΩ. In experiment, the following condition is always held: $R_{10x} = R_{10y}$ and $R_{11x} = R_{11y}$

terminal of it through a buffer and a resistance R_k; R_k will determine the damping parameter κ. Further, the output of the integrator is passed through an unity gain inverter and a buffer, and it is distributed in two ways: **(i)** it is directly added to the x-system by the use of an inverting adder (A4x) through R_{10x} that determines the coupling strength ϵ_1, and **(ii)** it is passed through an inverter (connecting "A" and "B", for $\beta_1 = 1, \beta_2 = -1$) or directly connected (connecting "A" and "C", for $\beta_1 = 1, \beta_2 = 1$) to inverting adder A4y through resistor R_{10y} that also determines ϵ_1; thus we always kept $R_{10x} = R_{10y}$ and $R_{11x} = R_{11y}$.

Let $V_1(t)$ and $V_2(t)$ be the voltage drop across the capacitor C_0 of the low-pass filter section of the x-system and y-system, respectively. Also, let the output of

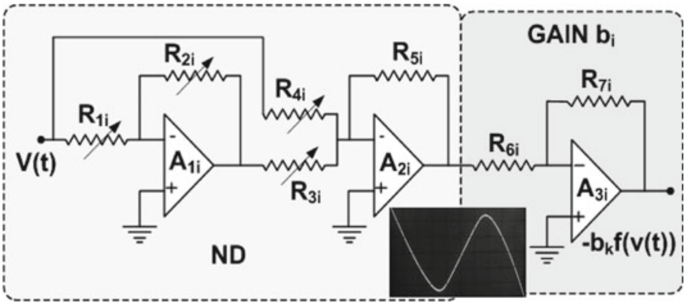

Fig. 4.2 Nonlinear device (ND) along with the gain block (b_i). A1i-A3i ($i = x, y$) are op-amps (TL 074), $R_1 = 1.26$ kΩ, $R_2 = 19.29$ kΩ, $R_3 = 52.81$ kΩ, $R_4 = 6.73$ kΩ, $R_5 = 10$ kΩ, $R_6 = 1$ kΩ. Inset shows the experimental oscilloscope trace of the nonlinearity produced by the ND

the integrator A5 be $V_3(t)$, which represents the *environment*. Thus, the following equations represent the time evolution of the circuit:

$$R_0C_0\frac{dV_1(t)}{dt} = -V_1(t) + \frac{R_{9x}}{R_{8x}}b_1 f(V_{1T_D}) + \frac{R_{9x}}{R_{10x}}\beta_1 V_3(t), \tag{4.3a}$$

$$R_0C_0\frac{dV_2(t)}{dt} = -V_2(t) + \frac{R_{9y}}{R_{8y}}b_2 f(V_{2T_D}) + \frac{R_{9y}}{R_{10y}}\beta_2 V_3(t), \tag{4.3b}$$

$$C_I\frac{dV_3(t)}{dt} = -\frac{1}{R_k}V_3(t) - \frac{1}{R_{11x}}\beta_1 V_1(t) - \frac{1}{R_{11y}}\beta_2 V_2(t). \tag{4.3c}$$

Here, $b_1, b_2 = \frac{R_{7i}}{R_{6i}}$ is the gain of the amplifier A3i ($i = x, y$) (Fig. 4.2), $\beta_1 = 1$, and $\beta_2 = \mp 1$, depending upon connection topology. $f(V_{jT_D}) \equiv f\big(V_j(t - T_D)\big) \equiv f(V_{j_\tau})$, ($j = 1, 2$), is the nonlinear function representing the output of the nonlinear device (ND) of Fig. 4.2, in terms of the input voltage V_{j_τ}. T_D is the time delay produced by the delay block. Also, we choose $R_{8x,y} = R_{9x,y} = 1$ kΩ.

The nonlinearity of nonlinear device (Fig. 4.2) has the following form:

$$f(V_{jT_D}) = -\frac{R_{5i}}{R_{4i}}V_{jT_D} + \frac{R_{5i}}{R_{3i}}\beta V_{sat}\tanh\left(w\frac{R_{2i}}{R_{1i}}\frac{V_{jT_D}}{V_{sat}}\right). \tag{4.4}$$

See Eq. 2.30 and the corresponding discussions.

Let us define the following dimensionless variables and parameters: $t = \frac{t}{R_0C_0}$, $\tau = \frac{T_D}{R_0C_0}$, $x = \frac{V_1(t)}{V_{sat}}$, $x_\tau = \frac{V_{1T_D}}{V_{sat}}$, $y = \frac{V_2(t)}{V_{sat}}$, $y_\tau = \frac{V_{2T_D}}{V_{sat}}$, $z = \frac{V_3(t)}{V_{sat}}$, $\frac{R_{5i}}{R_{4i}} = n_1$, $\beta\frac{R_{5i}}{R_{3i}} = m_1$, $w\frac{R_{2i}}{R_{1i}} = l_1$, $b_{1,2} = \frac{R_{7i}}{R_{6i}}$, $\epsilon_1 = \frac{R_{9i}}{R_{10i}}$, $\kappa = \frac{R_0C_0}{R_kC_I}$, $\frac{\epsilon_2}{2} = \frac{R_0C_0}{R_{11i}C_I}$, where $i = x, y$. To make the timescale of the $x-$, y-systems and the z-system equal, we use $C_I = C_0$. Now, we get $\kappa = \frac{R_0}{R_k}$, $\frac{\epsilon_2}{2} = \frac{R_0}{R_{11i}}$. Thus, to make $\epsilon_1 = \epsilon_2$, we have to use $R_{11i} = 2R_{10i}$ (since $R_0 = R_{9i} = 1$ kΩ).

Now, the Eqs. (4.3) and (4.4) can be reduced to the following dimensionless, coupled, first-order, retarded type nonlinear delay differential equations:

$$\frac{dx}{dt} = -x(t) + b_1 f(x_\tau) + \epsilon_1 \beta_1 z, \tag{4.5a}$$

$$\frac{dy}{dt} = -y(t) + b_2 f(y_\tau) + \epsilon_1 \beta_2 z, \tag{4.5b}$$

$$\frac{dz}{dt} = -\kappa z - \frac{\epsilon_2}{2}\big(\beta_1 x + \beta_2 y\big), \tag{4.5c}$$

where

$$f(u_\tau) = -n_1 u_\tau + m_1 \tanh(l_1 u_\tau), \tag{4.6}$$

with, $u \equiv x, y$. It is interesting to note that Eq. (4.5) (along with Eq. (4.6)) are qualitatively equivalent to Eq. (4.1) (along with Eq. (4.2)) with $a = 1$, and appropriate choices of n_1, m_1 and l_1.

4.2.2 Experimental Results

The coupled system is designed in hardware level using IC TL074 op-amps (JFET quad op-amps) with ±15 volt power supply. The resistances are $R_1 = 1.26$ kΩ, $R_2 = 19.29$ kΩ, $R_3 = 52.81$ kΩ, $R_4 = 6.73$ kΩ, $R_5 = 10$ kΩ, $R_6 = 1$ kΩ. For the low-pass section, we used $R_0 = 1$ kΩ and $C_0 = 0.1$ μF. Also, for the z-system, we choose $R_k = 1$ kΩ and $C_I = 0.1$ μF. The identical active all-pass filter stages of delay line (Fig. 2.13 in Chap. 2 (p. 26)) have $R_{12} = R_{13} = 2.2$ kΩ, $C = 10$ nF, and a variable resistance R.

4.2.2.1 Real-Time Waveform and Phase-Plane Plots

We fix the feedback delay to the value $\tau = 3.6$ and $R_7 \approx 2.1$ kΩ to keep both the systems in the hyperchaotic regime. In the following cases, we consider the coupling resistors for which $\epsilon_1 = \epsilon_2$.

(i) $\beta_1 = 1$ and $\beta_2 = -1$: This condition is satisfied by connecting the points "A" to "B", and "D" to "E", in the Fig. 4.1. Figure 4.3 shows three distinct cases: **(a)** The x- and y-systems evolve independently in time for large (small) coupling resistance (coupling strength). For example, when we keep $R_{10x} = R_{10y} \approx 9.96$ kΩ, $R_{11x} = R_{11y} = 20$ kΩ, both the systems are unsynchronized. Figure 4.3(a1) shows the time series of the x-system (yellow (lighter)) and the y-system (blue (darker)), and the red trace in the lower portion of this plot shows the difference $[V_1(t) - V_2(t)]$ (we call it the "error signal") of the two systems captured by a digital storage oscilloscope (DSO) (Tektronix TDS2002B, 60 MHz, 1 GS/s). It can be noticed that the amplitude of the error signal is of the same order as the original signals $V_1(t)$ and $V_2(t)$ indi-

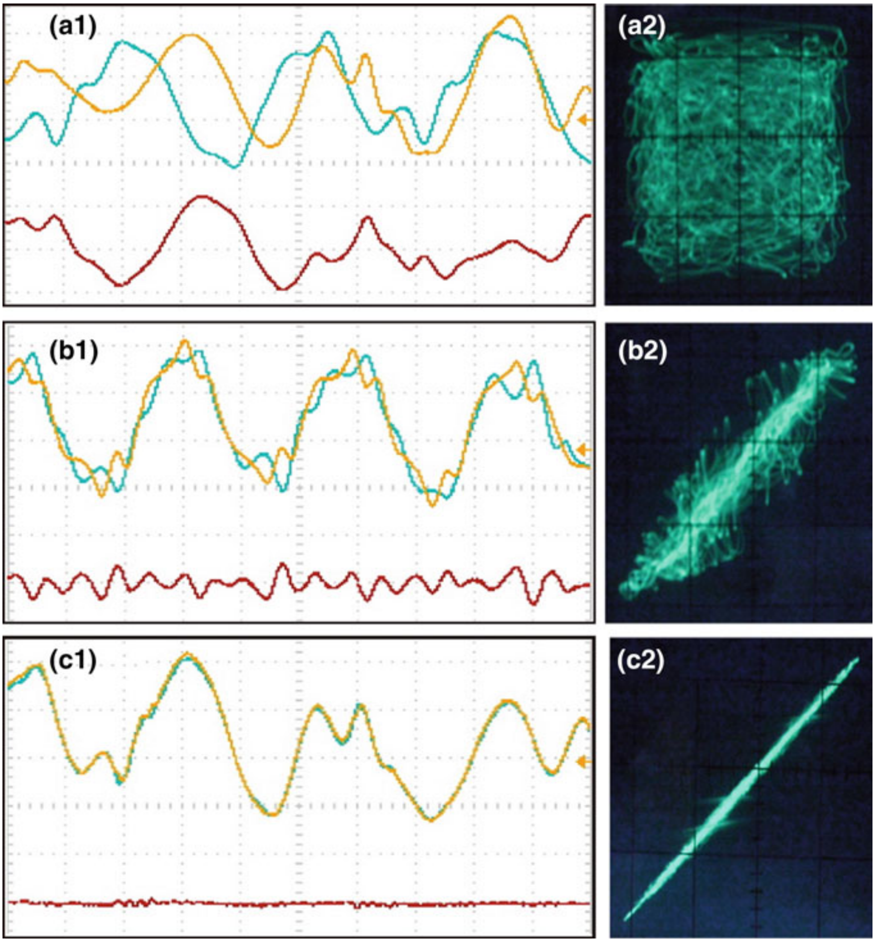

Fig. 4.3 $\beta_1 = 1$ and $\beta_2 = -1$: Experimental time series plot of the x-system $V_1(t)$ (yellow (lighter)) and the y-system $V_2(t)$ (blue (darker)) in the *hyperchaotic* regime, lower trace in red represents the error signal $(V_1(t) - V_2(t))$: **a1** unsynchronized state, **b1** in-phase synchronization, **c1** complete synchronization. The corresponding phase-plane plots are shown in (**a2**), (**b2**), and (**c2**), respectively. (For parameter values see text). For (**a1**), (**b1**), and (**c1**): x-axis: 25µs/div, y-axis: 1.25 v/div. For (**a2**), (**b2**), and (**c2**): x-axis: 1 v/div, y-axis: 1 v/div

cating unsynchronized states. Figure 4.3(a2) shows the corresponding phase-plane plot in $V_1(t) - V_2(t)$ space that confirms the asynchronous condition. **(b)** If we decrease the coupling resistors (i.e., increase the coupling strength ϵ), the coupled systems show in-phase synchronization. This is shown for $R_{10x} = R_{10y} \approx 1.57$ kΩ, $R_{11x} = R_{11y} \approx 3.2$ kΩ in Fig. 4.3(b1), (b2); the time series in Fig. 4.3(b1) shows that the waveforms are in phase but their amplitude levels are still uncorrelated in timescale. Also, the amplitude of error signal is much reduced here. Figure 4.3(b2)

shows the corresponding phase-plane diagram, where we can see that the system dynamics now wanders around the 45° diagonal line. These two indicate the in-phase synchronization of the x- and y-systems. **(c)** Further reduction in the coupling resistors results in complete synchronization. Figure 4.3(c1), (c2) show this for $R_{10x} = R_{10y} \approx 0.56$ kΩ and $R_{11x} = R_{11y} \approx 1.2$ kΩ. Figure 4.3(c1), (c2) shows the real-time and phase-plane plots of the systems, respectively. The error line in lower portion of Fig. 4.3(c1) indicates that the two waveforms are equal in phase and amplitude. The phase-plane plot in Fig. 4.3(c2) showing 45° inclination with both the axes confirms complete synchronization.
(ii) $\beta_1 = \beta_2 = 1$: This condition is achieved when we connect the points "A" to "C" and "D" to "F", in Fig. 4.1. In this case also, we get three distinct situations: **(a)** The x- and y- systems evaluate independently in time for larger coupling resistance. Figure 4.4(a1), (a2) show this for $R_{10x} = R_{10y} \approx 9.93$ kΩ, $R_{11x} = R_{11y} = 20$ kΩ. Figure 4.4(a1) shows the time series of the x- and y-systems, and that in the lower portion of the plot shows the sum of the two waveforms $(V_1(t) + V_2(t))$. Figure 4.4(a2) shows the corresponding phase-plane plot. The sum and the phase-plane plot confirm that the systems are not synchronized. **(b)** Lowering of coupling resistances results in inverse-phase synchronization. This is shown in Fig. 4.4(b1), (b2) for $R_{10x} = R_{10y} = 2$ kΩ, $R_{11x} = R_{11y} \approx 4.1$ kΩ. Figure 4.4(b1) shows the time series and the sum $(V_1(t) + V_2(t))$, and Fig. 4.4(b2) shows the corresponding phase-plane plot. One can see that $V_1(t)$ and $V_2(t)$ are in the phase-inverted mode but their amplitudes do not correlate. **(c)** At further lower coupling resistance values, the systems show anti-synchronization; Fig. 4.4(c1), (c2) shows the real-time and phase-plane plots, respectively, for $R_{10x} = R_{10y} \approx 0.3$ kΩ, $R_{11x} = R_{11y} \approx 0.7$ kΩ. Here one can see that the two systems have π phase shift and also their amplitude levels are same. The phase-plane plot shows that the system dynamics lives in a diagonal line making an angle 135° with the x- axis. This confirms the occurrence of anti-synchronization.

4.2.2.2 Generalized Autocorrelation Function (GAF) and Correlation of Probability of Recurrence (CPR)

It is seen from numerical simulations (Fig. 2.5 in Chap. 2 (p. 20)) and experimental results that the attractor of the system under study is not phase-coherent.[1] The detection of phase in non-phase-coherent system is of utmost difficulty and is an open problem. Let us go through a discussion of defining phase in a system in general in tabular form (see Table 4.1). For this purpose, we take recourse to Romano et al. [108] and consider the system has a dominant peak in power spectrum.

However, the situation is not so hopeless. The credit goes to Poincaré, as he called on the concept of recurrence in dynamical system (H. Poincare, Acta. Math. 1890), and proved that *"after a sufficiently long time interval, the trajectory of a*

---

[1] *Phase coherence* is the state in which two or more signals maintain a fixed phase relationship between them or to a reference signal.

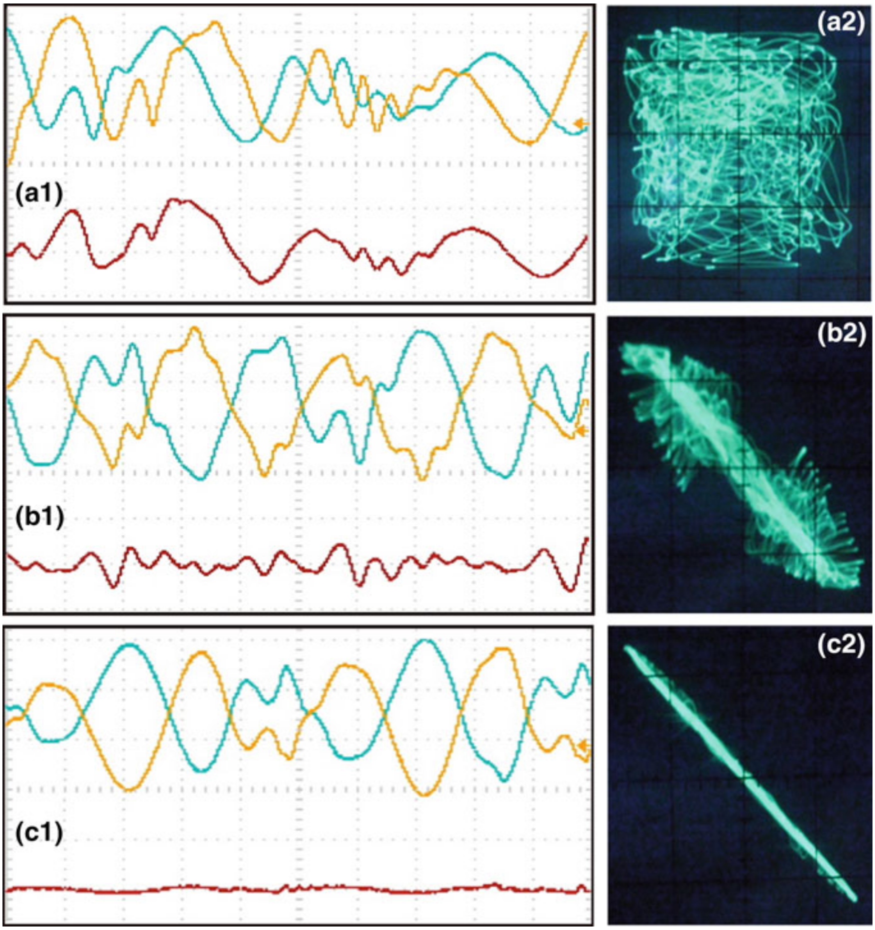

Fig. 4.4 $\beta_1 = 1$ and $\beta_2 = 1$: Experimental time series plots of the x-system $V_1(t)$ (yellow (lighter)) and the y-system $V_2(t)$ (blue (darker)) in the *hyperchaotic* regime, lower trace in red represents the error signal $(V_1(t) + V_2(t))$: **a1** unsynchronized state, **b1** in-phase synchronization, **c1** complete synchronization. The corresponding phase-plane plots are shown in (**a2**), (**b2**), and (**c2**), respectively. (For parameter values see text). For (**a1**), (**b1**), and (**c1**): x-axis: 25µs/div, y-axis: 1.25 v/div. For (**a2**), (**b2**) and (**c2**): x-axis: 1 v/div, y-axis: 1 v/div

dynamical system will return arbitrarily close to each former point of its route with probability one". This is the concept of recurrence. Later on, recurrence plots (RPs) were introduced to yield a visual representation of recurrences in phase space [33]. The RPs are defined for a given trajectory $\{x_i\}_{i=1}^{N}$ with $x_i \in \mathcal{R}^+$ of a dynamical system as

$$R_{i,j}^{(\epsilon)} = \Theta\big(\epsilon - ||x_i - x_j||\big), \quad i, j = 1, \ldots, N, \tag{4.7}$$

where ϵ is a predefined threshold and $\Theta(\cdot)$ is the Heaviside function.

Table 4.1 Table discussing the methods of defining phase in dynamical systems and their difficulties.

Method	Difficulties
Projecting the trajectory on an appropriate plane—the smeared limit cycle with well-defined rotations around center. Then, the phase is the angle of rotation	The projected trajectory should go around a center, this is not applicable in non-phase-coherent oscillators, effect of false neighbor
Choose a Poincaré surface that is crossed transversely by each trajectories. The phase is defined as the linear function of time, which increases by 2π with each return to the surface	It is difficult to identify surfaces that are crossed transversely by each trajectory
Based on general idea of curvature	Suitable for low-dimensional systems

Thus for complex and high-dimensional system, one can define the phase Φ for Eq. (4.7). In periodic systems, the phase increases by 2π for the trajectory to complete one rotation around the center or, equivalently, when $||x(t+T)-x(t)|| = 0$, where T is the period. In the case of complex system, this analogy may be drawn by assigning an increment 2π in phase for $||x(t+\tau)-x(t)|| \approx 0$ or, equivalently, $||x(t+T)-x(t)|| < \epsilon$. Therefore, one may look for the probability $P^{(\epsilon)}(\tau)$ that the system returns to the ϵ-neighborhood of a former point x_i of the trajectory after τ time steps and comparing $P^{(\epsilon)}(\tau)$ for both systems allows to detect and quantify PS properly. This is called the *generalized autocorrelation function* (GAF). Thus, as there exists no general technique of finding phase of a phase-incoherent hyperchaotic attractor, we use two dynamical measures of phase synchronization (PS) proposed in Refs. [81, 108], namely, generalized autocorrelation function ($P(t)$, here we write $P(t) \equiv P^{(\epsilon)}(\tau)$) and correlation of probability of recurrence (CPR). These two measures have already been used in the context of chaotic phase synchronization of *directly* coupled time-delayed systems [119]. Here, we compute $P(t)$ and CPR of the coupled system *experimentally* using the time series data acquired from the experimental circuit.

The generalized autocorrelation function ($P(t)$) is defined as [81, 108]

$$P(t) = \frac{1}{N-t}\sum_{i}^{N-t} \Theta\left(\epsilon_t - \|x_i - x_{i+t}\|\right), \tag{4.8}$$

where Θ is the Heaviside function, x_i is the i-th data point in the x variable, N is the total number of data points, ϵ_t is a preassigned threshold value, and $\|.\|$ represents the Euclidean norm. Let $P_1(t)$ represent the generalized autocorrelation function of the x-system and $P_2(t)$ be that of the y-system. We compute $P_1(t)$ and $P_2(t)$ from the experimental time series data ($N = 2400$) acquired using DSO (Tektronix TDS2002B, 60 MHz, 1 GS/s). For both the cases, we choose the threshold value $\epsilon_t = 0.01$.

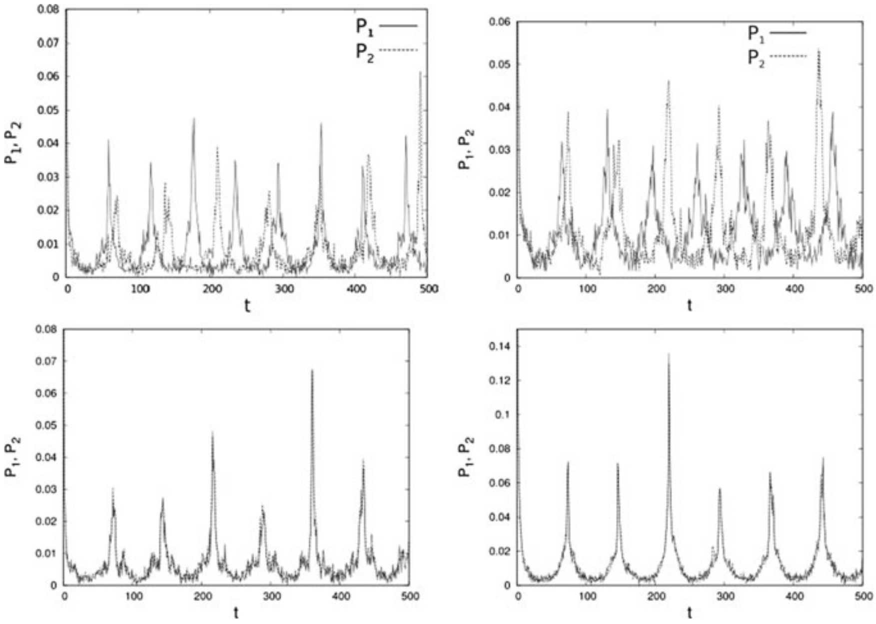

Fig. 4.5 Generalized autocorrelation function ($P(t)$) computed from the experimental time series. (Left column) $\beta_1 = 1, \beta_2 = -1$: GAF ($P(t)$) of x-system (P_1, in red) and y-system (P_2, in blue) in the unsynchronized state (upper panel) and in-phase synchronized state (lower panel). Notice the matching (difference) of the peaks of P_1 and P_2 in the in-phase synchronized (unsynchronized) case. (Right column) $\beta_1 = 1, \beta_2 = 1$: GAF ($P(t)$) of x-system (P_1, in red) and y-system (P_2, in blue) in the unsynchronized state (upper panel) and inverse-phase synchronized state (lower panel). Notice the matching (difference) of the peaks of P_1 and P_2 in the inverse-phase synchronized (unsynchronized) case (for parameter values see text)

Figure 4.5 (Left column) shows $P(t)$'s for $\beta_1 = 1, \beta_2 = -1$ (i.e., in-phase coupling case), and Fig. 4.5 (Right column) shows the same for $\beta_1 = 1, \beta_2 = 1$ (i.e., inverse-phase coupling case). Left upper panel of Fig. 4.5 represents the unsynchronized state for $\beta_1 = 1, \beta_2 = -1$ at $R_{10x,y} \approx 9.96$ kΩ, $R_{11x,y} = 20$ kΩ (same parameter values as of Fig. 4.3(a1)); similarly, Fig. 4.5 (Right upper panel) shows the same for $\beta_1 = 1, \beta_2 = 1$ at $R_{10x,y} \approx 9.93$ kΩ, $R_{11x,y} = 20$ kΩ (same parameter values as of Fig. 4.4(a1)). From both the figures (upper row), we can see that peaks of $P_1(t)$ do not match with that of $P_2(t)$ in the t-axis, confirming the fact that the phases of the two oscillators are not synchronized. Lower row of Fig. 4.5 shows the case for ($R_{10x,y} \approx 1.57$ kΩ, $R_{11x,y} \approx 3.2$ kΩ) and ($R_{10x,y} = 2$ kΩ, $R_{11x,y} \approx 4.1$ kΩ), respectively, which depicts that the dominant peaks of $P_1(t)$ and $P_2(t)$ match exactly in the t-axis confirming the phase synchronization of the coupled oscillators. Also, almost equal amplitude of the peaks in the phase synchronized cases shows the good quality of PS in the coupled systems.

A quantitative measure of $P(t)$ is the correlation of probability of recurrence (CPR) that was defined in Refs. [81, 108] as

$$CPR = \frac{\langle \bar{P}_1(t)\bar{P}_2(t) \rangle}{\sigma_1\sigma_2}, \tag{4.9}$$

$\bar{P}_{1,2}$ present that the mean value has been subtracted, and $\sigma_{1,2}$ are the standard deviations of the $P_1(t)$ and $P_2(t)$, respectively. In the phase synchronized case, generally, CPR $\approx$ 1, and for the unsynchronized case, its value is appreciably smaller than unity. Using the definition of Eq. (4.9), we compute CPR from experimental time series data both for the in-phase and inverse-phase cases. For in-phase synchronized case, we have CPR $\approx$ 0.997 (parameters are same as of left lower panel of Fig. 4.5), and for inverse-phase synchronized case we have CPR $\approx$0.985 (parameters are same as of right lower panel of Fig. 4.5), which confirm the occurrence of phase synchronization in the coupled system.

4.2.2.3 Concept of Localized Sets

We use another dynamical measure for qualitative confirmation of phase synchronization called the *concept of localized sets* (CLS) proposed in [95]. It was shown in Ref. [95] that the CLS technique is extremely useful to detect phase synchronization even when no proper measure of phase is possible. The idea of CLS in coupled oscillators is based on the fact that if one identifies a certain event in the first oscillator and then track the second oscillator at that particular event, a set D will be obtained for the second oscillator; if that set spreads over the whole attractor space of the second oscillator then one may say that there is no phase correlation between the two coupled oscillators. On the contrary, if the set D becomes localized to a certain zone of the attractor space, then one can say that the coupled oscillators are phase synchronized.

From the experimental circuit, we simultaneously acquire the time series data of x- and y-systems (with 2400 data points for each). Next, we define the event $V_1(t) = -0.5$ for the $x-$system and track the values of $V_2(t)$ from the time series whenever that event is met. The obtained set of data values of $V_2(t)$, and the corresponding V_1 and V_2 are plotted in $V_1 - V_2$ space. Figure 4.6 shows the localized sets for the in-phase and inverse-phase cases at unsynchronized, phase synchronized and complete (anti-) synchronized cases. It can be seen that for the unsynchronized cases (Fig. 4.6a for $\beta_1 = 1, \beta_2 = -1$ and Fig. 4.6d $\beta_1 = 1, \beta_2 = 1$), the set D (represented by black points) spreads over the whole attractor space of $V_2(t)$ (resistor values are same as used in Fig. 4.3(a1) ($\beta_1 = 1, \beta_2 = -1$) and Fig. 4.4(a1) ($\beta_1 = 1, \beta_2 = 1$), respectively). With further decrease in $R_{10x,y}$ and $R_{11x,y}$ (that is increase in coupling strength), the set D becomes localized in $V_2(t)$-space indicating the occurrence of phase synchronization; Fig. 4.6b and e show this case for in-phase and inverse-phase cases, respectively (resistor values are same as used in Fig. 4.3(b1) ($\beta_1 = 1, \beta_2 = -1$) and Fig. 4.4(b1) ($\beta_1 = 1, \beta_2 = 1$), respectively). Here, we can see that the black points representing the set D are localized to a small zone of $V_2(t)$. Another interesting observation can be made from Fig. 4.6, that is, for in-phase synchronized state (Fig. 4.6b), the localized set D is situated around $V_2(t) = -0.5$, which is equal to $V_1(t) = -0.5$, whereas for inverse-phase synchronized state (Fig. 4.6e), the localized set D is situated around $V_2(t) = 0.5$, which is opposite of $V_1(t) = -0.5$ (indicating a π phase shift between $V_1(t)$ and $V_2(t)$). Finally, with further decrease in coupling resistance (i.e., increase in coupling strength), we observe that the set D becomes localized to a very narrow range of $V_2(t)$ that indicates complete synchronization (Fig. 4.6c) and anti-synchronization (Fig. 4.6f).

4.3 Linear Stability Analysis

In this section, we explore the linear stability of synchronized states of the coupled system of Eq. (4.1). In [106], stability of the synchronized states of the environmentally coupled flows with no delay has been derived with some broad approximations; it was shown that no exact analysis is possible; nevertheless, the authors arrived at a condition that predicts the stable complete (anti-) synchronized zone in parameter space. In the present case, the scenario is more complex owing to the presence of delay. Let us start by considering ψ, θ and ϕ be the deviations from the synchronized states of the system variables in the Eq. (4.1), i.e., we introduce new primed variables $x' = x - \psi, y' = y - \theta$ and $z' = z - \phi$. Then linearizing the system along with these deviations leads to

$$\dot{\psi} = -a\psi(t) + b_1 f'(x_\tau)\psi_\tau + \epsilon_1\beta_1\phi, \tag{4.10a}$$

$$\dot{\theta} = -a\theta(t) + b_2 f'(y_\tau)\theta_\tau + \epsilon_1\beta_2\phi, \tag{4.10b}$$

$$\dot{\phi} = -\kappa\phi - \frac{\epsilon_2}{2}(\beta_1\psi + \beta_2\theta), \tag{4.10c}$$

where $u_\tau \equiv u(t-\tau), u \equiv \psi, \theta$.

It is not possible to carry out an exact analysis of Eq. (4.10). To make the analysis possible, we impose some constraints to it and consider this one as a special case. Let us consider the complete synchronized state of the systems, i.e., $x = y$ and hence, $x_\tau = y_\tau$. Also, we define a new variable relating ψ and θ in the following way:

$$\chi = \beta_1\psi + \beta_2\theta. \tag{4.11}$$

With this, Eq. (4.10) can be reduced to the following equations (with $b_1 = b_2 = b$):

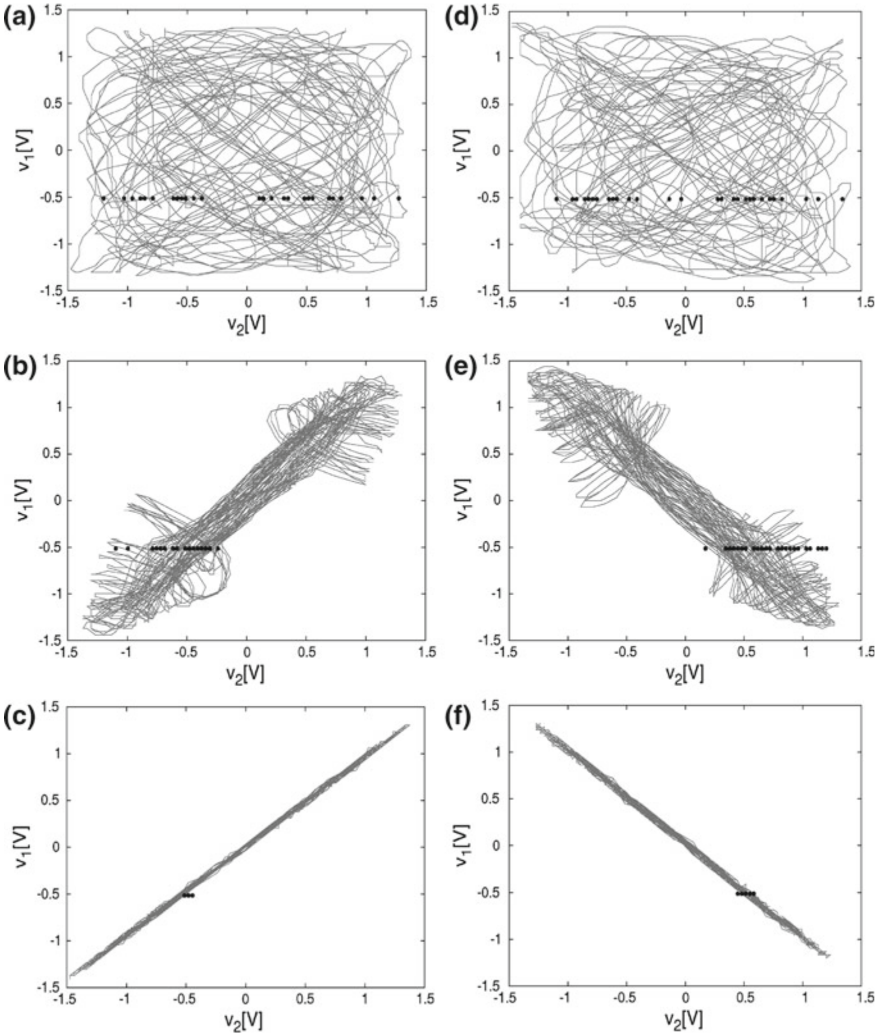

Fig. 4.6 Visualization through the concept of localized sets computed from the experimental time series: Black dots represent the set D for the particular event $V_1(t) = -0.5$, the points are plotted along with $V_1(t)$ and $V_2(t)$ in the $V_1(t) - V_2(t)$ space. $\beta_1 = 1, \beta_2 = -1$: **a** unsynchronized **b** in-phase synchronized **c** complete synchronized states. $\beta_1 = 1, \beta_2 = 1$: **d** unsynchronized **e** inverse-phase synchronized **f** anti-synchronized states. Note the localization of the set D in the narrow region in $V_2(t)$ axis for the phase synchronized (**b**, **e**) and complete (anti-) synchronized cases (**c**, **f**). For parameter values, see text

$$\dot{\chi} = -a\chi + bf'(x_\tau)\chi_\tau + \epsilon_1(\beta_1^2 + \beta_2^2)\phi, \tag{4.12a}$$

$$\dot{\phi} = -\kappa\phi - \frac{\epsilon_2}{2}\chi. \tag{4.12b}$$

Equation (4.12) also cannot be solved in closed form. We can make further approach by considering $f'(x_\tau) = \delta'$, where δ' is a constant; this approximation was also used and justified in [106]. Define $\delta = b\delta'$ and $\beta_1^2 + \beta_2^2 = 2$, from Eq. (4.12), we get

$$\dot{\chi} = -a\chi + \delta\chi_\tau + 2\epsilon_1\phi, \tag{4.13a}$$

$$\dot{\phi} = -\kappa\phi - \frac{\epsilon_2}{2}\chi. \tag{4.13b}$$

The characteristic equation of Eq. (4.13) is given by

$$\det\begin{pmatrix} \lambda + a - \delta e^{-\lambda\tau} & -2\epsilon_1 \\ \frac{\epsilon_2}{2} & \lambda + \kappa \end{pmatrix} = 0, \tag{4.14}$$

which gives on evaluation

$$\lambda^2 + (a + \kappa - \delta e^{-\lambda\tau})\lambda - \delta\kappa e^{-\lambda\tau} + (a\kappa + \epsilon_1\epsilon_2) = 0. \tag{4.15}$$

The eigenvalue of the characteristic Eq. (4.15) may be real or imaginary. Let us consider $\lambda = \mu \pm i\nu$. The synchronization will become just oscillatory if the eigenvalue is a purely imaginary one. Thus for the limiting case, we consider $\mu = 0$ and $\lambda = \pm i\nu$. Substitution of this in the above and a comparison between the real and the imaginary parts yield

$$-b\delta'\nu \sin\nu\tau - b\delta'\kappa\cos\nu\tau = \nu^2 - (a\kappa + \epsilon_1\epsilon_2), \tag{4.16}$$

$$-b\delta'\nu\cos\nu\tau + b\delta'\kappa\sin\nu\tau = -(a + \kappa)\nu. \tag{4.17}$$

Squaring and adding Eqs. (4.16) and (4.17), we get

$$\nu^4 + (a^2 + \kappa^2 - 2\epsilon_1\epsilon_2 - b^2\delta'^2)\nu^2 + (a\kappa + \epsilon_1\epsilon_2)^2 - b^2\delta'^2\kappa^2 = 0. \tag{4.18}$$

Consider $(a^2 + \kappa^2 - 2\epsilon_1\epsilon_2 - b^2\delta'^2) = \Theta$ and $(a\kappa + \epsilon_1\epsilon_2)^2 - b^2\delta'^2\kappa^2 = \Lambda$. Thus, Eq. (4.18) reduces to

$$\nu^4 + \Theta\nu^2 + \Lambda = 0. \tag{4.19}$$

Equation (4.19) has the following solution:

$$\nu^2 = \frac{-\Theta \pm \sqrt{\Theta^2 - 4\Lambda}}{2}. \tag{4.20}$$

From the above equation, it may be stated that ν^2 must be real and positive, otherwise there is no purely imaginary roots of Eq. (4.15), and for this one requires $\Theta^2 > 4\Lambda$ along with $\nu^2 > 0$, that results

$$\epsilon_1\epsilon_2 < |\kappa(\delta - a)|. \tag{4.21}$$

This condition leads to the oscillatory solution of the complete synchronization (CS) indicating the loss of CS. Thus, the threshold condition of CS is

$$\epsilon_{1cr}\epsilon_{2cr} = |\kappa(\delta - a)|. \tag{4.22}$$

Here, ϵ_{1cr} and ϵ_{2cr} are only the lower limits of the coupling strengths, where a stable complete synchronized state can be achieved. If we increase the coupling strength beyond the critical values, then the synchronized state will be prevailed. In the next section, we numerically confirm this result with proper choice of the effective value of δ. Also, note that Eq. (4.22) is equally valid for the anti-synchronized (AS) state, because in that case consideration of $y(t) = -x(t)$ and $\beta_1 = \beta_2 = 1$ does not alter the form of Eq. (4.10).

4.4 Numerical Simulation

The system Eq. (4.1) is simulated numerically using the fourth-order Runge–Kutta algorithm with step size $h = 0.01$. Following initial functions have been used for all the numerical simulations: for the x-system $\phi_x(t) = 1$, for the y-system $\phi_y(t) = 0.9$, and for the environment, i.e., z-system, $z(0) = 0.85$. Also, the following system design parameters are chosen throughout the numerical simulations: $a = 1, n = 2.2$, $m = 1$, $l = 10$, $\kappa = 1$; also we choose $b_1 = b_2 = 1$ and $\tau = 3.6$ to ensure that both the systems are in the hyperchaotic region [12]. Unless otherwise stated, we use $\epsilon_1 = \epsilon_2 = \epsilon$.

4.4.1 Lyapunov Exponent Spectrum

The onset of in-phase (inverse-phase) synchronization and complete (anti-) synchronization can be detected directly from the Lyapunov exponent (LE) spectrum of the coupled system [96]. We compute the LE spectrum in ϵ-space ($\epsilon_1 = \epsilon_2 = \epsilon$) directly from Eq. (4.1). Among a large number of LEs, we track the behavior of the first four LEs that are sufficient to detect the occurrence of phase or complete (anti-) synchronization with the variation of ϵ [106]. For $\beta_1 = 1$, $\beta_2 = -1$, Fig. 4.7a shows the first five LEs in ϵ-space; it can be observed that with increase in ϵ, the fourth largest LE (LE4) crosses the zero value to become negative at $\epsilon \approx 1.1$ indicating the transition from unsynchronized state to in-phase synchronized state. With further increase in ϵ, we observe that LE3 also becomes negative (from a positive value) at $\epsilon \approx 1.48$, which indicates the transition from in-phase synchronization to complete synchronization. Similar case is shown in Fig. 4.7b for $\beta_1 = 1$, $\beta_2 = 1$; here we can see that LE4 becomes negative at $\epsilon \approx 1.2$ indicating inverse-phase synchronization and transition of LE3 from a positive value to a negative value at $\epsilon \approx 1.56$ indicates anti-synchronization of the coupled systems.

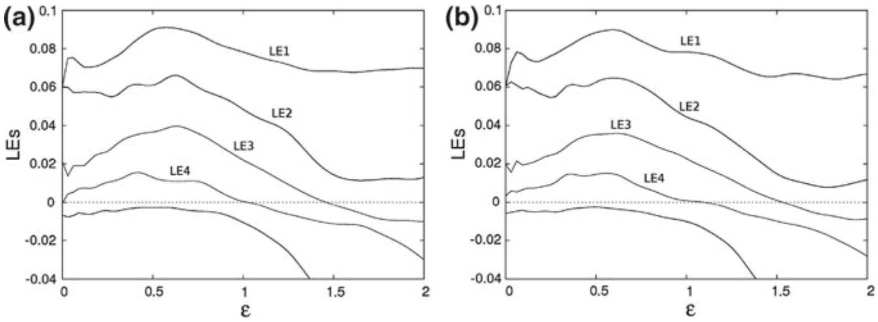

Fig. 4.7 Lyapunov exponent spectrum of the environmentally coupled system. **a** $\beta_1 = 1, \beta_2 = -1$. **b** $\beta_1 = 1, \beta_2 = 1$. Transitions of LE4 from positive to negative value through zero indicates phase synchronization, similar transition of LE3 indicates complete (anti-) synchronization

4.4.2 Time Series and Phase-Plane Plots

Guided by the above result, we choose three different coupling strengths, ϵ ($\epsilon_1 = \epsilon_2 = \epsilon$), and plot the time series and phase-plane plots for the illustrative examples of unsynchronized, phase synchronized, and complete (anti-) synchronized states. Figure 4.8 (Left column) shows this for $\beta_1 = 1, \beta_2 = -1$. Upper panel of Fig. 4.8 shows the unsynchronized case at $\epsilon = 0.2$; corresponding phase-plane plot indicates no correlation between the x-system and y-system. Middle panel of Fig. 4.8 shows the in-phase synchronized state at $\epsilon = 1.4$; we can see from the corresponding phase-plane plot that although the phases of two systems are synchronized but their amplitudes still differ. Finally, lower panel of Fig. 4.8 shows the case of complete synchronization at $\epsilon = 1.6$; here both the systems become identical to each other. Figure 4.8 (Right column) shows the scenario for $\beta_1 = \beta_2 = 1$. At $\epsilon = 0.2$, we can see the unsynchronized case (upper panel); at $\epsilon = 1.4$, the system is inverse-phase synchronized (middle panel), and finally at $\epsilon = 1.6$, we observe anti-synchronization (lower panel), where $x(t)$ and $y(t)$ have a π phase shift and their amplitude levels are similar.

4.4.3 Generalized Autocorrelation Function and CPR

As discussed in Sect. 4.2.2.2 (p. 63), we compute $P(t)$ and CPR from numerical simulations. We use $N = 5000$ and plot $P_{1,2}(t)$ for the unsynchronized and phase synchronized cases. Figure 4.9 (upper row) shows this at $\epsilon_1 = \epsilon_2 = 0.2$ for ($\beta_1 = 1, \beta_2 = -1$) and ($\beta_1 = \beta_2 = 1$), respectively. The unmatched dominant peaks of $P_{1,2}(t)$ indicate the lack of phase synchronization in the coupled systems at this small value of coupling strength. We plot the same at $\epsilon_1 = \epsilon_2 = 1.4$ (Fig. 4.9 (lower row)). Here, the perfect matching of dominant peaks of $P_{1,2}(t)$ indicates the occurrence of

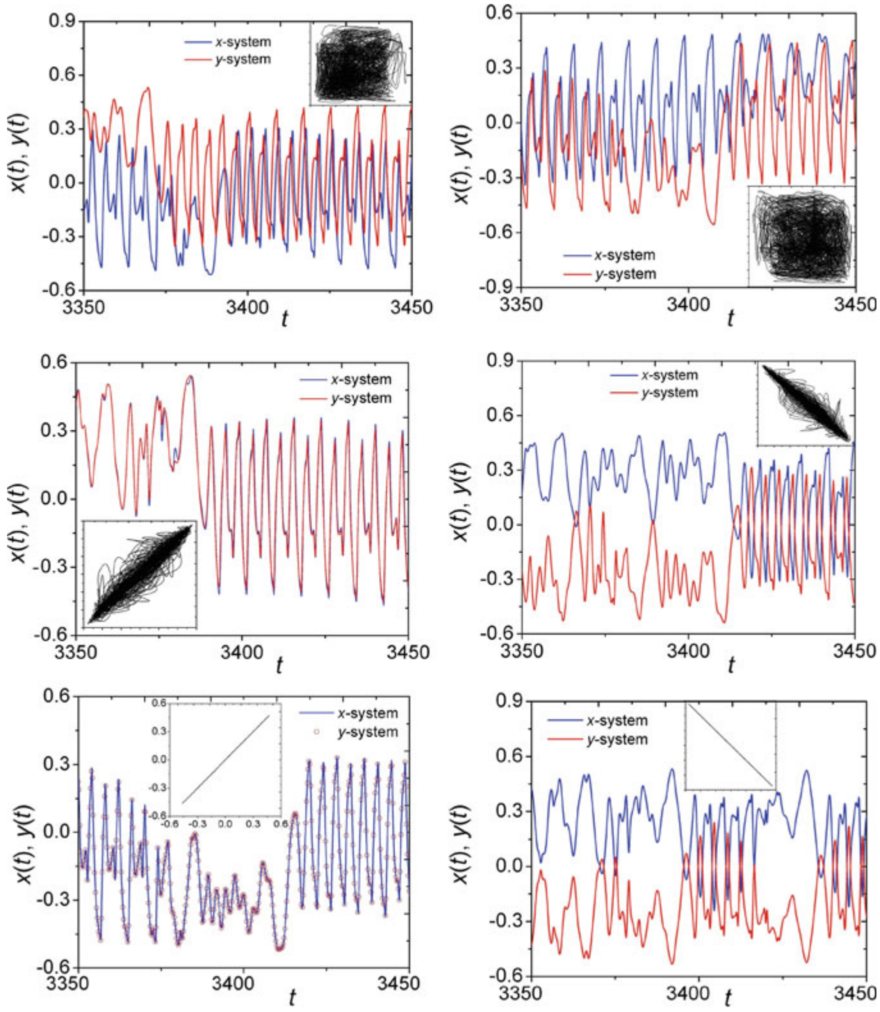

Fig. 4.8 (Left column) $\beta_1 = 1$ and $\beta_2 = -1$: Numerically obtained time series of x and y, and corresponding phase-plane plots in $x - y$ space. (Upper panel): unsynchronized state ($\epsilon = 0.2$), (middle panel): in-phase synchronized state ($\epsilon = 1.4$), (lower panel): complete synchronized state ($\epsilon = 1.6$); (Right column) $\beta_1 = 1$ and $\beta_2 = 1$: Numerically obtained time series of x and y, and corresponding phase-plane plots in $x - y$ space. (Upper panel): unsynchronized state ($\epsilon = 0.2$), (middle panel): inverse-phase synchronized state ($\epsilon = 1.4$), (lower panel): anti-synchronized state ($\epsilon = 1.6$)

PS; at this point we computed CPR, which is equal to 0.99 for $\beta_1 = 1$, $\beta_2 = -1$, and 0.987 for $\beta_1 = \beta_2 = 1$ that also confirms the occurrence of PS in the coupled system.

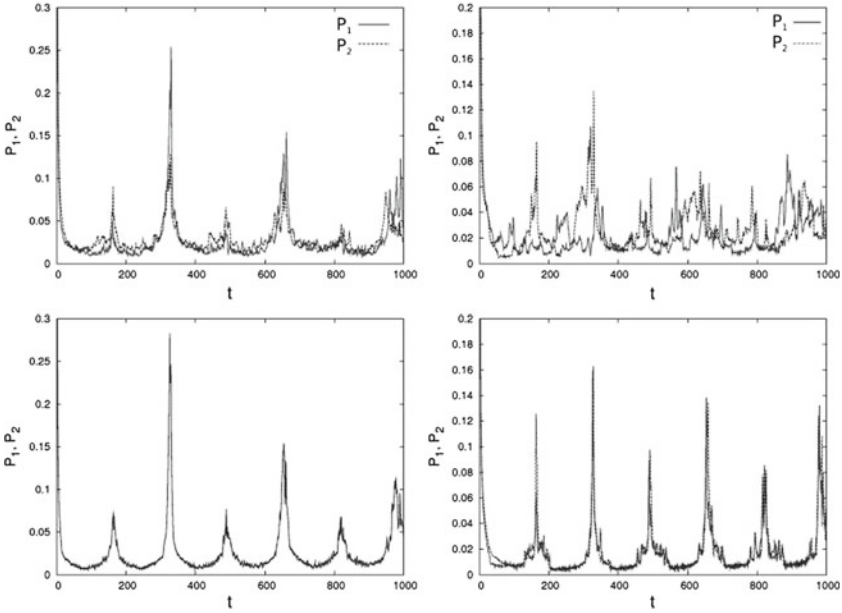

Fig. 4.9 (Left column) $\beta_1 = 1, \beta_2 = -1$: Numerically obtained generalized autocorrelation function, $P(t)$, of x-system (P_1, in solid) and y-system (P_2, dotted) in the unsynchronized state ($\epsilon = 0.2$) (upper panel) and in-phase synchronized state ($\epsilon = 1.4$) (lower panel). Notice the matching (difference) of the peaks of P_1 and P_2 in the in-phase synchronized (unsynchronized) case; (Right column) $\beta_1 = 1, \beta_2 = 1$: Numerically obtained generalized autocorrelation function, $P(t)$, of x-system (P_1, in red) and y-system (P_2, in blue) in the unsynchronized state ($\epsilon = 0.2$) (upper panel) and inverse-phase synchronized state ($\epsilon = 1.4$) (lower panel). Notice the matching (difference) of the peaks of P_1 and P_2 in the inverse-phase synchronized (unsynchronized) case (for other parameter values see text)

4.4.4 Concept of Localized Set

Further, we use the technique of concept of localized set to numerically confirm PS in the coupled system. Here, we define the following event in the y-system: $y(t) = -0.2$ and $y(t - \tau) \leq -0.2$; whenever this event occurs in time, we track the values of the x-system and get a set of values of $x(t)$. Then we plot this set in the $x(t) - x(t - \tau)$ space. The similar process is repeated for the y-system with the following event in the x-system: $x(t) = -0.2$ and $x(t - \tau) \leq -0.2$. Figure 4.10 shows this for $\beta_1 = 1, \beta_2 = -1$ and Fig. 4.11 represents the case for $\beta_1 = \beta_2 = 1$ for various coupling strengths. Figures 4.10a, d and 4.11a, d show the spreading of data set over the whole phase space for $\epsilon_1 = \epsilon_2 = 0.2$ indicating phase-incoherent behavior of the coupled systems. At $\epsilon_1 = \epsilon_2 = 1.4$, the data set forms a localized set in the phase space indicating the occurrence of phase synchronization (Figs. 4.10b, e and 4.11b, e). Finally, at $\epsilon_1 = \epsilon_2 = 1.6$, we can see that Fig. 4.10c, f shows that the localized set becomes identical with the defined event itself for $\beta_1 = 1, \beta_2 = -1$, indicating

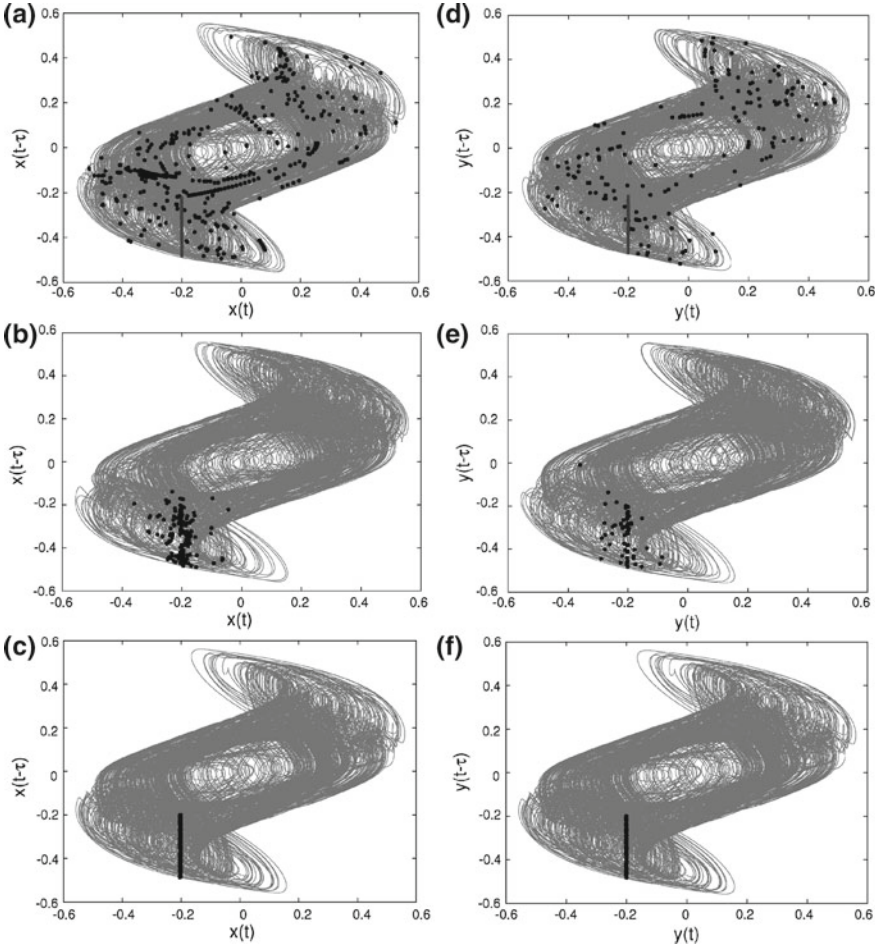

Fig. 4.10 $\beta_1 = 1$ and $\beta_2 = -1$: Visualization through the concept of localized sets (numerical): **a**, **b**, and **c**: plot of $x(t) - x(t - \tau)$ along with the set D (black dots) obtained by defining the following event in the y-system: $y(t) = -0.2$ and $y(t - \tau) \leq -0.2$ (dark line in (**d**)). **d**, **e**, and **f**: plot of $y(t) - y(t - \tau)$ along with the set D (black dots) obtained by defining the following event in the x-system: $x(t) = -0.2$ and $x(t - \tau) \leq -0.2$ (dark line in (**a**)). **a** and **d** represents unsynchronized state with $\epsilon = 0.2$ (note that the black dots are scattered all around the attractors representing that the attractors are incoherent). **b** and **e** represents phase synchronized states with $\epsilon = 1.4$. **c** and **f** represent complete synchronized case with $\epsilon = 1.6$. Note that in the last two cases black dots form a localized set that lives in a narrow region of the attractor

a complete phase synchronization. Whereas, for $\beta_1 = \beta_2 = 1$, at $\epsilon_1 = \epsilon_2 = 1.6$ Fig. 4.11c, f shows that the localized set is situated in a narrow region that is just opposite to the defined event, indicating anti-phase synchronization.

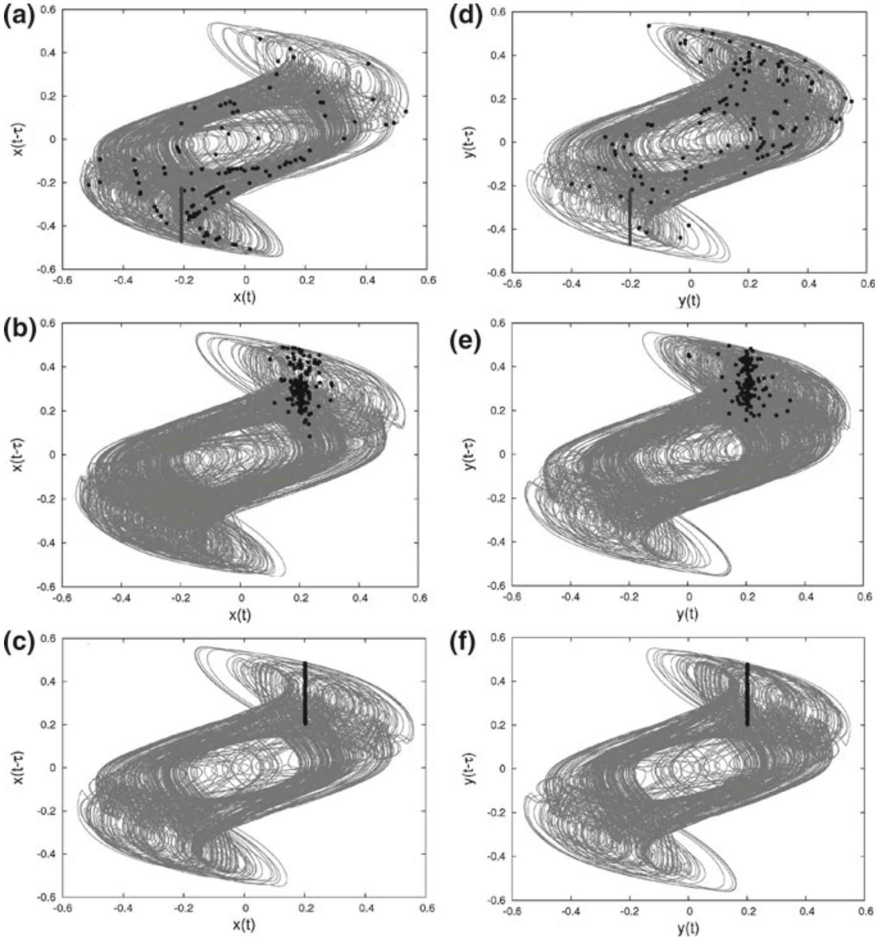

Fig. 4.11 $\beta_1 = 1$ and $\beta_2 = 1$: Numerically computed concept of localized sets: **a**, **b**, and **c**: plot of $x(t) - x(t - \tau)$ along with the set D (black dots) obtained by defining the following event in the y-system: $y(t) = -0.2$ and $y(t-\tau) \leq -0.2$ (dark line in (**d**)). **d**, **e**, and **f**: plot of $y(t) - y(t-\tau)$ along with the set D (black dots) obtained by defining the following event in the x-system: $x(t) = -0.2$ and $x(t - \tau) \leq -0.2$ (dark line in (**a**)). **a** and **d** represent unsynchronized state with $\epsilon = 0.2$ (note that the black dots are scattered all around the attractors representing that the attractors are incoherent). **b** and **e** represent phase synchronized states with $\epsilon = 1.4$. **c** and **f** represent anti-synchronized case with $\epsilon = 1.6$

4.4.5 Stability of Synchronization in Parameter Space

To support the theoretical result obtained analytically in Eq. (4.22), numerically we study the synchronization scenario in the $\epsilon_1 - \epsilon_2$ space. We use all the above-mentioned measures to detect the complete synchronization (CS) and anti-synchronization (AS). The threshold value of ϵ_1 and ϵ_2 for which CS and AS occurs

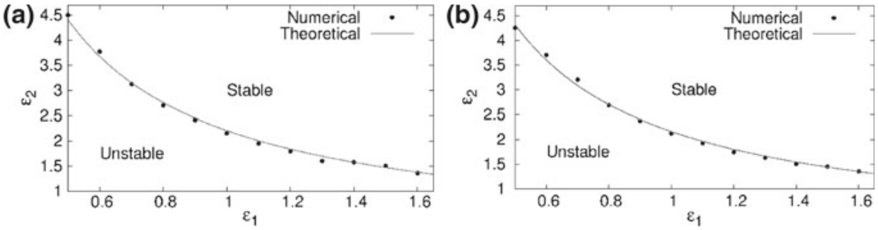

Fig. 4.12 Stability curve in $\epsilon_1 - \epsilon_2$ parameter space **a** $\beta_1 = 1$ and $\beta_2 = -1$, **b** $\beta_1 = 1$ and $\beta_2 = 1$

are plotted in Fig. 4.12 a and b, respectively. The solid line represents the theoretical prediction and points represent the numerically obtained threshold values for which CS or AS just start. In theoretical curve, for CS, we use $\delta' = 3.20$ (also $a = 1$, b=1, and $\kappa = 1$); this value of δ' is obtained for $x_\tau = \pm 0.0825$ (remember that $\delta' = f'(x_\tau)$). Similarly for AS, we use $\delta' = 3.15$, that implies $x_\tau \approx \pm 0.0832$. In both the cases, the values of x_τ, for which theoretical and numerical results match, lie well within the actual phase space where the system dynamics live. Thus, the stability analysis agrees with the numerical results with some effective choice of δ'.

4.5 Discussions

In this chapter, we have reported different synchronization scenarios of hyperchaotic time-delayed systems coupled indirectly through a common environment. The system we have chosen is a first-order, nonlinear time-delayed system that possesses a closed-form mathematical function for the nonlinearity, shows hyperchaos even at a moderate or small time delay, and is convenient for the electronic circuit design. We have confirmed the occurrence of phase synchronization and complete (anti-) synchronization in the experimental circuit by using recurrence analysis and the concept of localized sets computed directly from the experimental time series data. We have shown that with the proper choice of coupling parameters (i.e., $\beta_1 = 1$, $\beta_2 = -1$), an increase in the coupling strength results in a transition from unsynchronized state to complete synchronized state via phase synchronized states. Also, for $\beta_1 = \beta_2 = 1$, with the increasing coupling strength, we have observed a transition from unsynchronized states to the anti-synchronized state via inverse-phase synchronized states. To corroborate the experimental results, we have presented a linear stability analysis of the complete (anti-) synchronized state, and also we perform detailed numerical simulations. Numerically, we computed the Lyapunov exponent spectrum of the coupled system from where we have identified the zone of phase synchronization and complete (anti-) synchronization in the parameter space. We have used the recurrence analysis and the concept of localized set to numerically reconfirm the occurrence of phase synchronization in the system. Finally, using all the measures, we have identified the parameter zone in the two-parameter space for the stable complete and anti-synchronization, which agree well with the theoretical results.

One of the main features of the environmental coupling scheme is that here the system dynamics in the synchronized states and unsynchronized states have almost the same structure in phase space; this particular feature makes this coupling scheme advantageous over other time delay coupling schemes. From the academic interest, as the environmental coupling is very much relevant in biological systems where delay appears inherently, therefore, the present study will be helpful for the understanding of synchronization phenomena in the biological systems. Apart from the academic interest, the present study is important from application point of view also; for example, since with environmental coupling one can make a transition from complete synchronization to anti-synchronization by simply changing the sign of β_2, thus this will be useful in implementation of hyperchaotic binary-phase-shift-keying (BPSK)-based digital communication systems.

Chapter 5
Collective Behavior-II: Amplitude Death and the Corresponding Transitions in Coupled Chaotic Time-Delayed Systems

In the previous chapter (Chap. 4), we have discussed synchronization scenarios in time-delayed systems. Another important collective behavior in coupled oscillators is *amplitude death* (AD) where oscillations cease and the oscillators arrive at the common stable steady state. AD is important in the case of control applications where suppression of unwanted fluctuations is necessary, e.g., in laser [66] and neuronal systems [36]. Lord Rayleigh [103] first observed AD in the acoustic systems. However, the systematic observation of AD has first been reported by Yamaguchi et al. [147]; later the same has been studied in detail by Bar-Eli [17], and Shiino and Frankowicz [127]. For an extensive review on AD, see Ref. [112].

Contrary to the phenomenon of AD in low-dimensional systems (with or without *coupling time delay*), amplitude death in systems with *intrinsic time delay* is a less explored topic. The first observation of AD in the intrinsic time-delayed oscillators has been reported by Konishi et al. [62] in which dynamic and delayed couplings were studied. AD in networks of delay-coupled delay oscillators has been studied analytically in Ref. [55]. Reference [71] reports AD in intrinsic time-delayed oscillators coupled via multiple delay connections. An important technique of inducing AD has been proposed in Ref. [48], which employs time delay open-plus-closed-loop coupling. In all of these works (except the case of dynamic coupling), AD is mediated by the presence of moderate or very long time delay in the coupling path. The presence of time delay in coupling path makes the dynamics of the coupled systems more complex, and at the same time much difficult for analysis and practical implementation.

In this chapter, we discuss amplitude death and the corresponding synchronization transitions leading to AD in coupled time-delayed hyperchaotic oscillators interacting through mean-field diffusive coupling. The idea of mean-field coupling is widely used in physics (e.g., in three-dimensional Ising spin model [92] interaction with mean-field explains ferromagnetism) and biology [42]. We will discuss a novel synchronization transition scenario that leads to AD, namely the transitions among AD,

D. Biswas and T. Banerjee, *Time-Delayed Chaotic Dynamical Systems*, SpringerBriefs in Nonlinear Circuits,
https://doi.org/10.1007/978-3-319-70993-2_5

generalized anticipatory synchronization (GAS), complete synchronization (CS), and *generalized lag synchronization* (GLS); this transition occurs for the variation of the difference of *intrinsic time delays*, $\tau_d = (\tau_2 - \tau_1)$ (τ_1 and τ_2 are the intrinsic time delays associated with two coupled systems). We show the occurrence of GAS for $\tau_d < 0$, CS for $\tau_d = 0$, and GLS for $\tau_d > 0$.

By definition [90, 148], in the GAS, CS, and GLS conditions, there exists a smooth function H such that $x_2(t) = H(x_1(t+\tau))$, $\tau \in \mathscr{R}^+$; for GAS, $\tau > 0$, and for GLS, $\tau < 0$; for conventional AS and LS states H is an identity function, i.e., $x_2(t) = x_1(t+\tau)$, and as usual, for a CS state, $x_2(t) = x_1(t)$. Earlier, it has been shown that mismatch in intrinsic time delay in linearly coupled time-delayed systems gives rise to generalized synchronization (GS) [14, 123]. In non-delayed systems, to observe GLS and GAS, appropriate controller has to be designed; Refs. [90, 148] reported two such controller design techniques to induce GLS and GAS in low-dimensional systems under *drive-response* coupling. Experimental confirmation of GLS has been reported in Ref. [154] which considers Rössler systems. Unlike non-delayed systems, in the present case, no controller is required but only variations of the intrinsic time delays give rise to GAS and GLS. Further, at present, there exists no general theory or confirmatory quantitative measures of GAS and GLS. In this chapter, we try to derive a general stability analysis for the GAS and GLS states using Krasovskii–Lyapunov theory. Also, we use error function and a modified form of the similarity function to provide the quantitative support to the occurrence of GAS and GLS. We further study the effect of coupling parameter for equal intrinsic time delays. It is shown that depending upon the coupling strength and mean-field parameters, the coupled systems show a transition from the unsynchronized state to AD state via in-phase and complete synchronized states.

5.1 Mean-Field Coupling

We consider N first-order time-delayed dynamical systems interacting through mean-field diffusive coupling; mathematical model of the coupled system is given by [10]

$$\dot{x_i} = h(x_i, x_{i\tau_i}; p) + \varepsilon\left(Q\overline{X} - x_i\right), \tag{5.1}$$

with $i = 1 \cdots N$, $\overline{X} = \frac{1}{N}\sum_{i=1}^{N} x_i$ is the mean-field of the coupled system. $x_\tau \equiv x(t-\tau)$, $\tau \in \mathscr{R}^+$ is the constant time delay, and p represents the m-dimensional parameter space. The coupling strength is given by ε, and Q is a control parameter that determines the density of mean-field [43, 124] ($0 \le Q \le 1$). Here, the function $h(x_i, x_{i\tau_i}; p)$ is given by $h(x_i, x_{2\tau_i}, p) = -ax_i - b_i f(x_{i\tau_i})$, thus the individual units are represented by the following scalar first-order, retarded type delay differential equations:

$$\dot{x_i} = -a_i x_i - b_i f(x_{i\tau_i}), \tag{5.2}$$

where $a_i > 0$ and b_i are the system parameters, and τ_i is the intrinsic time delay associated with the individual systems. Equation (5.2) represents a general class of first-order, nonlinear, retarded delay differential equations. For example, for the Mackey–Glass system [79]: $f(x_{i\tau_i}) = -\frac{x_{\tau_i}}{1+x^c_{\tau_i}}$; for the Ikeda system [56]: $f(x_{i\tau_i}) = \sin(x_{i\tau_i})$, etc. Thus, Eq. (5.1) represents mean-field diffusive coupling scheme for *any* first-order delay dynamical systems. Also, the following theoretical and numerical results can be extended to any first-order time-delayed systems.

5.2 Stability Analysis

In this section, we analyze the asymptotic stability of the synchronization of the coupled systems given in Eq. (5.1). Here, we restrict our study to a pair ($N = 2$) of time-delayed systems.

5.2.1 Krasovskii–Lyapunov Theory: Complete Synchronization ($\tau_1 = \tau_2$)

Let us define the error function as $\Delta = (x_1 - x_2)$, and also let $\tau_1 = \tau_2 = \tau$. Time evolution of the error function that describes the error dynamics of Eq. (5.1) is given by

$$\dot{\Delta} = -(a+\varepsilon)\Delta - (b_1 - b_2) f(x_{1\tau}) - b_2 f'(x_{1\tau})\Delta_\tau. \tag{5.3}$$

This is an inhomogeneous equation and difficult to deal with; to make it homogeneous, we impose the following constraint: $b_1 = b_2 = b$, which is also the necessary condition of complete synchronization. Now, Eq. (5.3) becomes

$$\dot{\Delta} = -(a+\varepsilon)\Delta - b f'(x_{1\tau})\Delta_\tau. \tag{5.4}$$

According to the Krasovskii–Lyapunov theory [64], a stable synchronization implies the stability of the origin of Eq. (5.4). The sufficient condition for the stability of synchronization requires the definition of a positive definite functional, $V(t)$, given by

$$V(t) = \frac{1}{2}\Delta^2 + \mu \int_{-\tau}^{0} \Delta^2(t+\varphi)d\varphi. \tag{5.5}$$

Here, $\mu > 0$ is an arbitrary positive parameter. The stability of the origin of Eq. (5.4) requires that the time derivative of $V(t)$ be negative. Now

$$\frac{dV}{dt} = -\mu\Delta^2\Gamma(X,\mu), \tag{5.6}$$

where

$$\Gamma(x,\mu) = \frac{(a+\varepsilon-\mu)}{\mu} + \frac{bf'(x_{1_\tau})}{\mu}x + x^2 \tag{5.7}$$

and $x = \frac{\Delta_\tau}{\Delta}$. Thus, from Eq. (5.6), it may be noted that dV/dt is negative if $\Gamma_{min} > 0$. Now, from Eq. (5.7), Γ_{min} is derived as

$$\Gamma_{min} = \frac{4\mu(a+\varepsilon-\mu) - b^2 f'^2(x_{1_\tau})}{4\mu^2}. \tag{5.8}$$

Hence, $\Gamma_{min} > 0$ implies that

$$a + \varepsilon > \frac{b^2 f'^2(x_{1_\tau})}{4\mu} + \mu = \Phi(\mu), \tag{5.9}$$

where $\Phi(\mu)$ is a function of μ. Now, we find the minimum value Φ_{min} by setting $\frac{d\Phi}{d\mu} = 0$. That gives $\mu = \frac{|bf'(x_{1_\tau})|}{2}$. With this value of μ, one gets the minimum value of Φ as $\Phi_{min} = |bf'(x_{1_\tau})|$; using this in Eq. (5.9), we get the following sufficient condition of complete synchronization:

$$a + \varepsilon > |bf'(x_{1_\tau})|. \tag{5.10}$$

Note that, Eq. (5.10) represents the sufficient condition of complete synchronization for *any* general first-order time-delayed systems of the form given by Eq. (5.2) coupled via mean-field diffusion.

5.2.2 Generalized (Anticipatory, Lag) Synchronization: ($\tau_1 \neq \tau_2$)

For GAS and GLS, we consider the following error function: $\Delta = H(x_{1_{\tau_2-\tau_1}}) - x_2$, where $x_{1_{\tau_2-\tau_1}} = x_1\big(t - (\tau_2 - \tau_1)\big)$. Using this, we can express three different synchronization phenomena, namely, generalized (anticipatory, lag), and complete synchronization. GAS is observed for $\tau_1 > \tau_2$; under this condition one has $x_2(t) = H\big(x_1(t + |\tau_2 - \tau_1|)\big)$. For $\tau_1 = \tau_2$, we have CS, i.e., $x_2(t) = x_1(t)$. GLS occurs for $\tau_1 < \tau_2$; in this case, one has $x_2(t) = H\big(x_1(t - |\tau_2 - \tau_1|)\big)$.

The time evolution of the error function is given by: $\dot{\Delta} = \dot{H}(x_{1_{\tau_2-\tau_1}}) - \dot{x_2}$. Since H is an unknown arbitrary function, further analysis is not possible. Considerable progress can be made if we consider $H(\mathbf{u}) = \Psi\mathbf{u}$, where Ψ is an appropriate scaling factor; this is a valid approximation only in the strong coupling case where the dynamics become periodic. With this, we have

$$\begin{aligned}\dot{\Delta} = -\Big(a + \varepsilon\Big(1 - \frac{Q}{2}\Big)\Big)\Delta + b\Big(f\big(x_2(t-\tau_2)\big) - f\big(x_2(t-\tau_1)\big)\Big) \\ - bf'\big(x_2(t-\tau_1)\big)\Delta_{\tau_1} + \frac{\varepsilon Q}{2}\Big(\Psi x_2\big(t-(\tau_2-\tau_1)\big) - x_1\Big),\end{aligned} \tag{5.11}$$

where $\Delta_{\tau_1} = \Delta(t-\tau_1)$, and $b_1 = b_2 = b$. The synchronization manifold is locally attracting if the origin of (5.11) is stable. It can be noted that for $\tau_1 = \tau_2$, i.e., complete synchronization, $\Psi = 1$, and $x_2(t-(\tau_2-\tau_1)) - x_1 = -\Delta$; thus Eq. (5.11) reduces to Eq. (5.4), and the Krasovskii–Lyapunov theory gives the same result as Eq. (5.10). For $\tau_1 \neq \tau_2$, since Eq. (5.11) is an inhomogeneous equation, it is not tractable for further analysis; but, in the small intrinsic time delay difference condition (i.e., $|\tau_2 - \tau_1|$ is small), we can neglect the second term in Eq. (5.11), and also write $(\Psi x_2(t-(\tau_2-\tau_1)) - x_1) = -\Psi'\Delta$, where Ψ' is a new scaling factor (note that for $|\tau_2 - \tau_1| = 0$, $\Psi' = 1$); under this condition, Eq. 5.11 reduces to

$$\dot{\Delta} = -\left(a + \varepsilon\Big(1 - \frac{Q}{2}(1-\Psi')\Big)\right)\Delta - bf'\big(x_2(t-\tau_1)\big)\Delta_{\tau_1}. \tag{5.12}$$

Note that Eq. (5.12) has the same form as Eq. (5.4); using the Krasovskii–Lyapunov theory and the same arguments of the previous subsections, we arrive at the following stability condition for the generalized (anticipatory, lag) synchronization:

$$a + \varepsilon\left(1 - \frac{Q}{2}(1-\Psi')\right) > |bf'\big(x_2(t-\tau_1)\big)|. \tag{5.13}$$

5.2.3 Linear Stability Analysis: Amplitude Death

Next, to find out the condition of amplitude death, we analyze the stability of synchronization by considering the deviations from the synchronized state. The same for the low-dimensional systems (without intrinsic time delay) has been reported in Refs. [105, 106, 124, 125]. Let us define ψ and ϕ to be the deviations from the synchronized states of the system variables x_1 and x_2 in Eq. (5.1), respectively. Then the linearization of the system along these deviations gives

$$\dot{\psi} = -a\psi - b_1 f'(x_{1_\tau})\psi_\tau + \varepsilon\big(Q\tfrac{\psi+\phi}{2} - \psi\big), \tag{5.14a}$$

$$\dot{\phi} = -a\phi - b_2 f'(x_{2_\tau})\phi_\tau + \varepsilon\big(Q\tfrac{\psi+\phi}{2} - \phi\big). \tag{5.14b}$$

An exact analysis of Eq. (5.14) is not possible due to the presence of the delay term, which makes the characteristic equation a *quasi-polynomial* one. We consider $b_1 = b_2$, and for the complete synchronization, we have $x_1 = x_2$ and $x_{1\tau} = x_{2\tau} = x_\tau$. Let us define $g(x_\tau, \psi, \psi_\tau) \equiv -a\psi - bf'(x_\tau)\psi_\tau$, and $g(x_\tau, \phi, \phi_\tau) \equiv -a\phi - bf'(x_\tau)\phi_\tau$. Now, Eq. (5.14) reduces to

$$\dot{\psi} = g(x_\tau, \psi, \psi_\tau) + \varepsilon\big(Q\tfrac{\psi+\phi}{2} - \psi\big), \tag{5.15a}$$

$$\dot{\phi} = g(x_\tau, \phi, \phi_\tau) + \varepsilon\big(Q\tfrac{\psi+\phi}{2} - \phi\big). \tag{5.15b}$$

The Jacobian matrix of the system is described by

$$\begin{pmatrix} \delta + \varepsilon\big(\frac{Q}{2} - 1\big) & \frac{Q\varepsilon}{2} \\ \frac{Q\varepsilon}{2} & \delta + \varepsilon\big(\frac{Q}{2} - 1\big) \end{pmatrix} = 0, \tag{5.16}$$

where we consider that the time-averaged values of $g'(x_\tau, \psi, \psi_\tau)$ and $g'(x_\tau, \phi, \phi_\tau)$ are approximately same and are equal to an effective constant δ. This type of approximation has been used in Refs. [105, 106, 124] for the low-dimensional systems without intrinsic time delay; here we extend the same for the time-delayed systems.

Now, the characteristic equation of the Jacobian matrix (5.16) is

$$\lambda^2 - 2\Lambda\lambda + \Lambda^2 - \left[\frac{\varepsilon Q}{2}\right]^2 = 0, \tag{5.17}$$

where $\Lambda = \delta + \varepsilon\big(\frac{Q}{2} - 1\big)$. Thus, we have the following two eigenvalues: $\lambda_1 = \delta + \varepsilon(Q - 1)$, $\lambda_2 = \delta - \varepsilon$. For amplitude death to occur, $\lambda_{1,2}$ should be negative [124], which gives: $Q < 1 - \frac{\delta}{\varepsilon}$, and $\varepsilon > \delta$. Thus, the critical parametric condition for which amplitude death occurs is given by

$$Q_{cr} = 1 - \frac{\delta}{\varepsilon_{cr}}, \tag{5.18}$$

along with $\varepsilon_{cr} > \delta$; here Q_{cr} and ε_{cr} are the critical values of the mean-field parameter and coupling strength, respectively.

5.3 Numerical Simulation

5.3.1 System Description

For numerical verification of the analytical predictions and demonstration of the collective behaviors, we consider the following first-order nonlinear retarded time-delayed system proposed in Chap. 2

$$\dot{x} = -ax - bf(x_\tau), \tag{5.19}$$

where a and b are positive parameters. The nonlinear function $f(x_\tau)$ is given by Eq. (2.35) (p. 30):

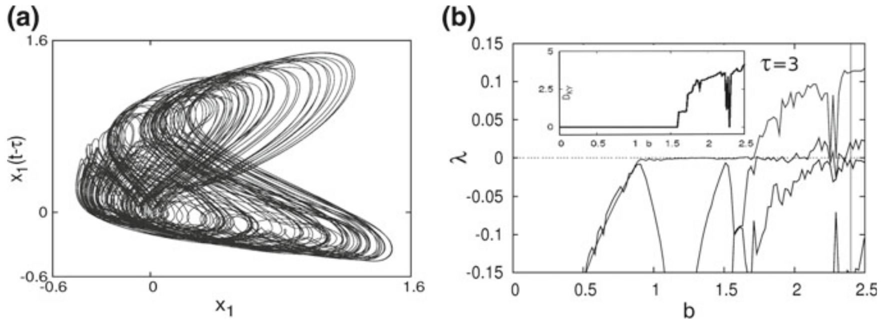

Fig. 5.1 **a** Hyperchaotic attractor for $b = 2.4$ and $\tau = 3$. **b** Lyapunov exponent spectrum with b for $\tau = 3$, the vertical line is for $b = 2.4$; the inset shows Kaplan–Yorke dimension (D_{KY}). Other parameter values are $a = 1$, $n = 1.15$, $m = 0.97$, and $l = 2.19$

$$f(x_\tau) = -0.5n\big(|x_\tau| + x_\tau\big) + m \tanh(lx_\tau), \tag{5.20}$$

where n, m, and l are positive parameters that determine the nature of the nonlinearity. The detailed chaotic dynamical behaviors have been discussed in Chap. 2. The nature of the hyperchaotic attractor for $b = 2.4$ and $\tau = 3$ for individual system along LE spectrum and D_{KY} dimension is shown in Fig. 5.1.

5.3.2 *Numerical Results*

The system Eq. (5.1) (with Eqs. (5.19) and (5.20)) is simulated numerically using Runge–Kutta algorithm with step size $h = 0.01$. Without any loss of generality, the following initial functions have been used for all the numerical simulations: for the x_1-system: $\xi_{x1}(t) = 0.95$, and for the x_2-system: $\xi_{x2}(t) = 0.85$. Also, the following system design parameters are chosen throughout the numerical simulations: $a = 1$, $n = 1.19$, $m = 0.97$, $l = 2.19$, and $b_1 = b_2 = 2.4$.

5.3.2.1 Effect of Intrinsic Time Delays: Transitions Among AD, GAS, CS, and GLS.

At first, we explore the effect of *intrinsic time delay* on the dynamics of the coupled system. Figure 5.2a depicts the phase diagram showing the zone of unsynchronized, synchronized, and AD states in $\varepsilon - \tau_2$ space for a constant τ_1. We observe that beyond a certain coupling strength [e.g., $\varepsilon = 5$, along the solid horizontal line of Fig. 5.2a], for a fixed τ_1, if τ_2 is varied from a low to high value, the coupled system shows transitions from AD to *generalized anticipatory synchronization* (GAS) (for $\tau_1 > \tau_2$) to complete synchronization (for $\tau_1 = \tau_2$) to *generalized lag synchronization* (GLS) (for $\tau_1 < \tau_2$), and again to AD state. Further, for a weaker coupling strength, we have a transition from GAS to CS to GLS, and no AD occurs. The analytically obtained critical value of ε, ε_{cr}, beyond which synchronization occurs is shown in Fig. 5.2a with dashed (red) line, which is obtained by using Eq. (5.13) (with, $\tau_1 = 6, \Psi' = 1.1, Q = 0.6$); it lies well within the numerically obtained synchronized zone indicating the effectiveness of our stability analysis.

Next, we consider $\varepsilon = 5$ and vary τ_2 (i.e., along the dotted (blue) line of Fig. 5.2a). Figure 5.2b shows the first five LEs; with increasing τ_2, the largest LE (solid line) makes a transition from negative values (indicating AD) to zero value [indicating periodic and synchronized (since all other LEs are negative) states], and again to negative values (indicating AD state). From the LE spectrum, it is also obvious that sufficient mismatch in intrinsic time delays enhance the region of AD in the parameter space. Further, unlike *delay-coupled oscillators*, we find no "avoided crossing" [59] in the LE spectrum confirming that no *phase-flip transition* occurs for the variation of intrinsic time delay. We compute Δ from Eq. (5.12) to show the real-time variation of the error function of GAS and GLS. Figure 5.2c, d show this for the GAS ($\tau_2 = 5.8$) and GLS ($\tau_2 = 6.2$), respectively, with $\varepsilon = 1.8$ which is greater than the analytically obtained value of ε_{cr} (with, $\tau_1 = 6, \Psi' = 1.1, Q = 0.6$). It is clear that the error function attains a zero steady-state value confirming the occurrence of GAS and GLS.

Next, for $\tau_1 = 6$ and $\varepsilon = 5$, we plot the time evolution of $x_1(t)$ (solid line) and $x_2(t)$ (dotted line). With the variation of τ_2, we can see the transitions (Fig. 5.2e–i) from AD ($\tau_2 = 4$) to GAS ($\tau_2 = 5.2 < \tau_1$), CS ($\tau_2 = 6 = \tau_1$) to GLS ($\tau_2 = 7 > \tau_1$), and finally again to AD ($\tau_2 = 8$). In the transient regions of the AD states in Fig. 5.2e, i, one can observe that the GAS and GLS behaviors, respectively, lead to AD; we find no "phase-flip" in the transient behaviors for any intrinsic time delay; this along with the LE spectrum confirms that variation of intrinsic time delay does not result in *phase-flip transition*.

Since at present, there exists no confirmatory quantitative measure of GAS and GLS, we compute a modified form of the similarity function S defined as [154]

$$S^2(\tau_d) = \frac{\left\langle [H\left(x_1(t+\tau_d)\right) - x_2(t)]^2 \right\rangle}{[\langle x_1^2(t)\rangle \langle x_2^2(t)\rangle]^{\frac{1}{2}}}, \tag{5.21}$$

where τ_d is the time delay between x_1 and x_2 that is equal to $\tau_d = |\tau_2 - \tau_1|$. For the synchronized states $S \approx 0$. For a GAS case (Fig. 5.2f), we find that $x_2(t)$ leads $x_1(t)$ by $\tau_d \approx |\tau_1 - \tau_2|$, and also using linear regression between $x_2(t)$ and $x_1(t+\tau_d)$ we find that $x_2(t) = H(x_1(t+\tau_d)) \approx 0.909 x_1(t+\tau_d)$. With this relation, from Eq. (5.21), we find the similarity function, $S_{GAS} = 0.039$; however, if we consider H as an identity function (as in the case of conventional AS), we have $S = 0.102$ that is much larger than S_{GAS}, which confirms the occurrence of GAS. At this point, it should be noted that, in general, H is not a linear scaling factor (unlike projective synchronization [44]), thus a higher order polynomial regression is needed to describe the form of H more precisely, and that results in a much lower value of S_{GAS}. Similarly, for GLS

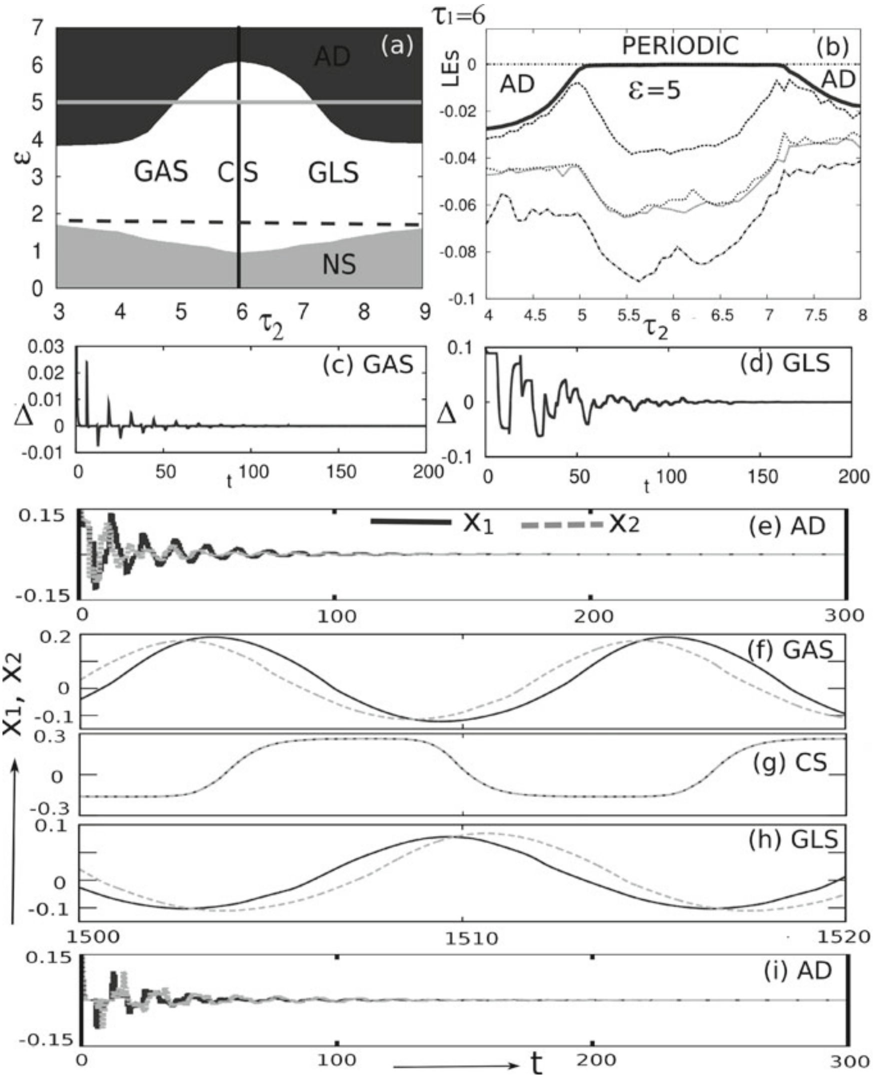

Fig. 5.2 $\tau_1 = 6$. **a** Phase diagram in $\varepsilon - \tau_2$ parameter space ($Q = 0.6$). NS: unsynchronized state. Horizontal dashed line indicates the analytically obtained critical curve for obtaining synchronized states. **b** The Lyapunov exponent (LE) spectrum with τ_2 for $\varepsilon = 5$, $\tau_1 = 6$, and $Q = 0.6$. **c**, **d** Time evolution of the error function of GAS ($\tau_2 = 5.8$) (**c**), and GLS ($\tau_2 = 6.2$) (**d**); both show that synchronization error asymptotically goes to zero. **e**–**i** time series of $x_1(t)$ and $x_2(t)$ show transitions from AD ($\tau_2 = 4$) to GAS ($\tau_2 = 5.2$) to CS ($\tau_2 = 6$) to GLS ($\tau_2 = 7$), and finally again to AD ($\tau_2 = 8$)

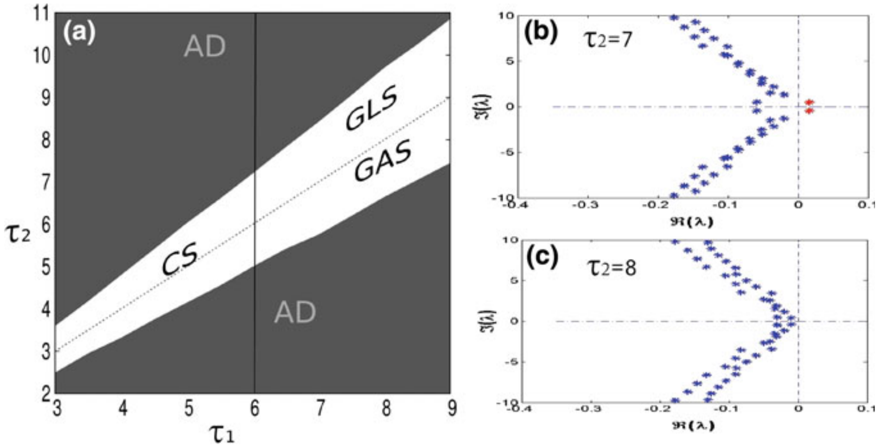

Fig. 5.3 **a** Phase diagram in τ_1–τ_2 parameter space ($\varepsilon = 5$, and $Q = 0.6$). Dotted diagonal line indicates CS for $\tau_1 = \tau_2$. **b**, **c** The eigenvalue spectrum of the coupled systems (**b**) $\tau_2 = 7$ (i.e., near but before AD) (**c**) $\tau_2 = 8$ (i.e., near but after AD); note that the real part of all the eigenvalues now become negative

(Fig. 5.2h) we find $x_2(t) = H(x_1(t - \tau_d)) \approx 1.081 x_1(t - \tau_d)$ ($\tau_d \approx |\tau_1 - \tau_2|$) with a similarity function $S_{GLS} = 0.035$, which is less than 0.112, computed by taking H as an identity function (i.e., conventional LS). For $\tau_1 = \tau_2$, we observe complete synchronization with $x_2(t) = x_1(t)$, and $S = 0$.

Next, we take a sufficiently high coupling strength ($\varepsilon = 5$) to ensure the synchronized state and vary τ_1 and τ_2 (Fig. 5.3a) simultaneously. We observe that two AD regions are separated by a synchronized state consisting of GAS ($\tau_1 > \tau_2$), CS [$\tau_1 = \tau_2$, i.e., along the diagonal dotted line], and GLS ($\tau_1 < \tau_2$). Thus, with the variation of ($\tau_1 - \tau_2$), we can clearly observe the following transitions: AD → GAS → CS → GLS → AD. We observe that for higher values of intrinsic time delays, larger mismatch is required to achieve AD for a fixed coupling strength. In this context, we also noticed that, for equal intrinsic time delays, with increasing intrinsic time delay, critical value to get AD increases slightly; this fact can be explained from Eq. (5.18), which shows that for a fixed Q, ε_{cr} is proportional to δ that is a function of intrinsic time delay.

To confirm the occurrence of AD quantitatively, we compute the eigenvalue spectrum of the coupled systems using the bifurcation package DDE-BIFTOOL [34]. For an illustrative example, Figs. 5.3b, c show the eigenvalue spectrum of the coupled systems for $\tau_2 = 7$ (i.e., near but before the occurrence of AD) and $\tau_2 = 8$ (i.e., near but after the occurrence of AD), respectively (other parameters are $\varepsilon = 5$ and $\tau_1 = 6$). With increasing τ_2, the real part of the largest eigenvalue changes from positive to negative value confirming the occurrence of AD in the coupled system. Further, we observe that the largest complex conjugate pair of eigenvalues cross the

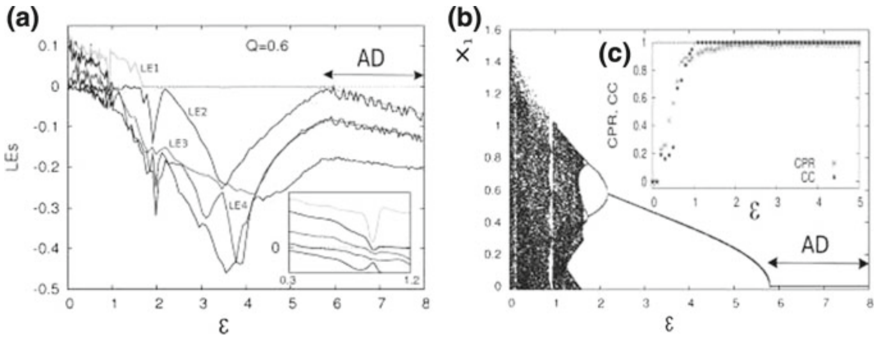

Fig. 5.4 Q = 0.6: **a** Lyapunov exponent (LE) spectrum of largest five LEs. Inset shows the same, but now the range is $\varepsilon \in (0.3, 1.2)$, and curves are smooth (through averaging) for clarity. **b** Bifurcation diagram of x_1 with ε. AD represents AD region in ε parameter space. **c** Variation of CPR and CC with ε (Q = 0.6)

imaginary axis $\Im(\lambda)$ from right to left confirming that the route to AD is indeed through a *Hopf bifurcation*.

5.3.2.2 Effect of Coupling: Transitions Among Unsynchronized, PS, CS, and AD

We set $\tau_1 = \tau_2 = 3$ (i.e., to ensure the hyperchaos in the uncoupled individual systems), and vary ε (with $Q = 0.6$). Figure 5.4a shows the first five LEs in the ε parameter space, $\varepsilon \in (0, 8)$. Inset of the figure shows the same in $\varepsilon \in (0.3, 1.2)$, but with smooth curves. It can be seen that LE4 becomes negative at $\varepsilon \approx 0.65$ that indicates the onset of phase synchronization (PS) [96]. Further, LE3 makes a transition from a positive to negative value at $\varepsilon \approx 1$, indicating the onset of complete synchronization (CS). With further increase in ε, the largest LE, LE1, becomes zero at $\varepsilon \approx 1.85$, indicating that the dynamics of the coupled systems now become periodic. The transition of LE1 from zero to a negative value is indicative of AD in the coupled systems. With further increase in ε, LE1 monotonically decreases toward a more negative value ensuring the stability of the AD state. The AD state can best be observed from the bifurcation diagram of x_1 (Fig. 5.4b) with ε. The figure shows the emergence of AD from hyperchaos through an inverse period doubling sequence.

The transition from the unsynchronized state to complete synchronized state through in-phase synchronized state is verified using *correlation of probability of recurrence* (CPR), and *cross-correlation function* (CC). The CPR is a quantitative measure of phase synchronization (PS) introduced in [81, 108]. It is related with the generalized autocorrelation function ($P(t)$) defined as,

$$P(t) = \frac{1}{N_1 - t} \sum_{i}^{N_1 - t} \Theta\Big(\varepsilon_t - \|x_i - x_{i+t}\|\Big). \tag{5.22}$$

See Chap. 4 (Sec. 4.2.2.2, p. 63) for a detailed discussion. The CPR is defined as [81, 108]: CPR $= \frac{\langle \bar{P}_1(t)\bar{P}_2(t)\rangle}{\sigma_1\sigma_2}$; $\bar{P}_{1,2}$ present that the mean value has been subtracted, and $\sigma_{1,2}$ are the standard deviations of the $P_1(t)$ and $P_2(t)$, respectively. For PS states, CPR ≈ 1. Further, the cross-correlation function is defined as

$$\mathrm{CC} = \frac{\Big\langle (x_1(t) - \langle x_1(t)\rangle)(x_2(t) - \langle x_2(t)\rangle)\Big\rangle}{\sqrt{\Big\langle (x_1(t) - \langle x_1(t)\rangle)^2\Big\rangle\Big\langle (x_2(t) - \langle x_2(t)\rangle)^2\Big\rangle}}. \tag{5.23}$$

CC is a measure of complete synchronization (CS) [96]; in the CS state, CC$= 1$. Figure 5.4c shows the variation of CPR and CC with ε. Increase of both the measures from a zero value with increase in the coupling strength ε agrees with the LE spectrum and bifurcation diagram. For $\varepsilon > 0.65$, CPR attains values nearly equal to unity indicating the onset of PS, and for $\varepsilon > 1$, CC attains a value of unity indicating the onset of CS in the coupled systems.

Figure 5.5 depicts the time variation of $x_1(t)$ and $x_2(t)$ (for $Q = 0.6$); it shows that with increasing ε, the coupled systems make a transition from unsynchronized to complete synchronized states via in-phase synchronized states. Further, this transition is associated with a simultaneous transition of system dynamics, namely the transition from hyperchaotic to periodic states. AD is shown in Fig. 5.5f for $\varepsilon = 6.2$, which shows that both of the coupled systems attain the *zero* steady state which is the only and trivial steady state of the uncoupled systems. Figure 5.6 depicts the phase diagram in the $\varepsilon - Q$ space, which shows three distinct regions, namely unsynchronized state (NS), in-phase or complete synchronized state (PS/CS), and amplitude death (AD) state. It is noteworthy that the transition from the unsynchronized state (NS) to synchronized state (PS/CS) does not depend upon the mean-field parameter Q, but depends only upon the coupling strength, ε, which is in accordance with the analytical result of Eq. (5.10).

5.4 Experiment

We set up an experiment using electronic circuit to implement the time-delayed system Eq. (5.19) (with Eq. (5.20)) under the mean-field diffusive coupling scheme given by Eq. (5.1). Figure 5.7 shows the representative diagram of the experimental electronic circuit. The proposed circuit consists of three distinct parts, namely, the x_1-system (upper portion), x_2-system (lower portion), and the circuit to realize the mean-field coupling (middle portion). Both the x_1 and x_2-systems consist of a low-pass section ($R_0 - C_0$), nonlinear device (ND), delay block (DELAY), gain (b_1 and b_2), and other circuitry used to realize the proper coupling. The ND block produces the nonlinearity of both x_1 and x_2-systems; the circuit to realize the ND block is shown in Fig. 2.25 in Chap. 2 (p. 36). For a given input voltage V_τ (say), this circuit has a nonlinearity, $f(V_\tau)$, given in Chap. 2

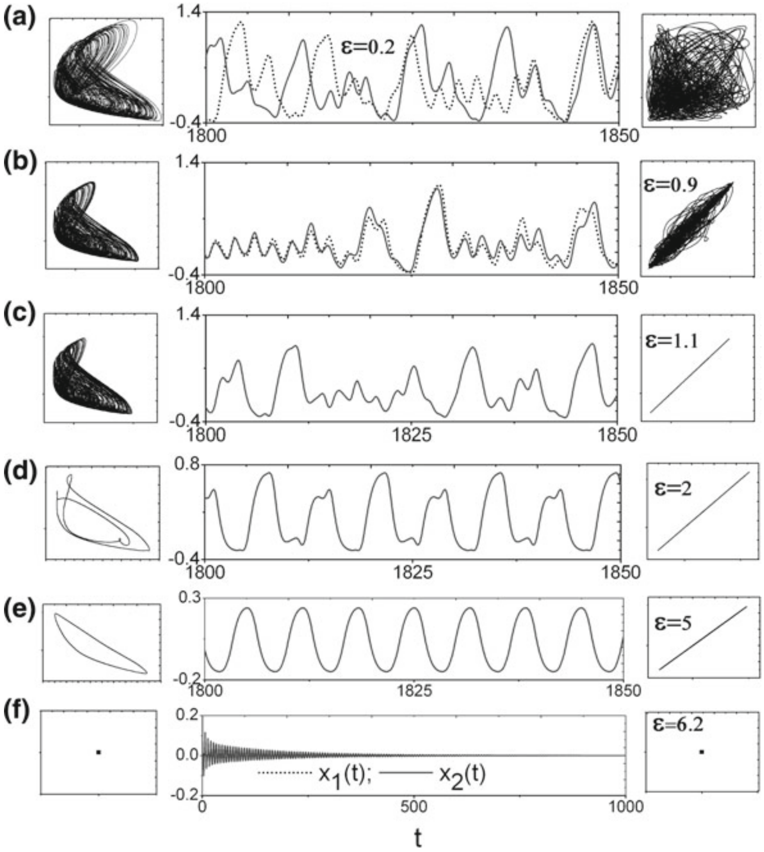

Fig. 5.5 Q = 0.6: variation of system dynamics and synchronization states for variable ε. It shows that with increasing ε the coupled systems make a transition from the unsynchronized state (hyperchaotic) (**a**) to amplitude death state (**f**) via hyperchaotic in-phase synchronized state (**b**) and hyperchaotic or chaotic and periodic complete synchronized states (**c**, **d**, **e**)

$$f(V_\tau) = -0.5\frac{R_5}{R_4}\Big(|V_\tau| + V_\tau\Big) + \frac{R_5}{R_3}\beta V_{sat}\tanh\left(\omega\frac{R_2}{R_1}\frac{V_\tau}{V_{sat}}\right). \tag{5.24}$$

Here, β and ω are certain scaling factors that depend upon the nonideal and asymmetric nature of the op-amps, and V_{sat} is the saturation voltage of the op-amps. The gain part b_1 and b_2 $(= b)$ is realized with op-amp A3 as shown in the same figure. The delay part is implemented using a chain of cascaded active all-pass filters (APF) [115] (shown in Fig. 2.13, p. 26).

Let $V_1(t)$ be the voltage drop across the capacitance C_0 of the low-pass section of x_1-system, and that of x_2-system be $V_2(t)$. Then, the equations that represent the circuit dynamics are

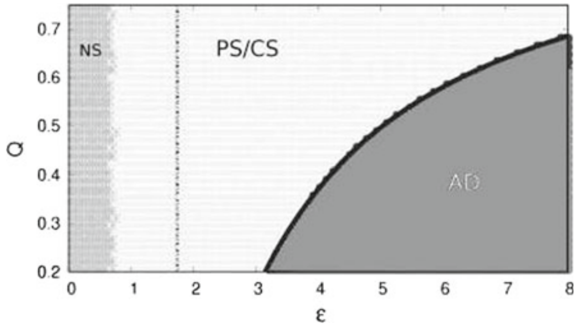

Fig. 5.6 Phase diagram in ε–Q parameter space. AD: amplitude death; PS/CS: in-phase or complete synchronized state; NS: unsynchronized state. Solid line indicates the analytically obtained critical curve for obtaining AD (with $\delta = 2.51$), dotted vertical line indicates the synchronization transition curve

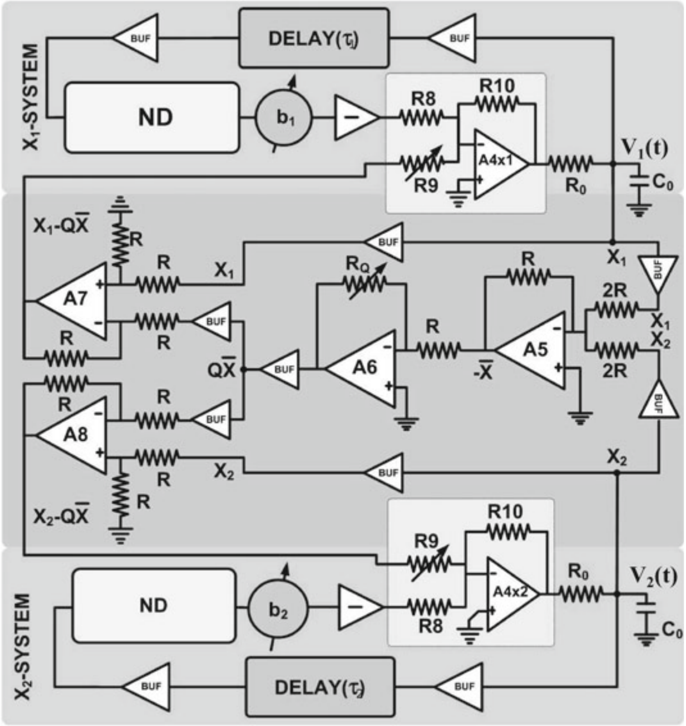

Fig. 5.7 Representative diagram of the experimental circuit (see text for a detailed description)

$$R_0C_0\frac{dV_1(t)}{dt} = -V_1(t) - \frac{R_{10}}{R_8}\left(\frac{R_7}{R_6}f\left(V_{1_{T_D}}\right)\right) + \frac{R_{10}}{R_9}\left(\frac{R_Q}{R}\overline{V(t)} - V_1(t)\right), \tag{5.25a}$$

$$R_0C_0\frac{dV_2(t)}{dt} = -V_2(t) - \frac{R_{10}}{R_8}\left(\frac{R_7}{R_6}f\left(V_{2_{T_D}}\right)\right) + \frac{R_{10}}{R_9}\left(\frac{R_Q}{R}\overline{V(t)} - V_2(t)\right). \tag{5.25b}$$

Here, $f(V_{i_{T_D}}) \equiv f(V_i(t-T_D))$ $(i = 1, 2)$ is given by Eq. 5.24, and $\overline{V(t)} = \frac{V_1(t)+V_2(t)}{2}$. Now, we define the following dimensionless parameters and variables: $t = \frac{t}{R_0C_0}$, $\tau = \frac{T_D}{R_0C_0}$, $x_1 = \frac{V_1(t)}{V_{sat}}$, $x_{1_\tau} = \frac{V_{1_{T_D}}}{V_{sat}}$, $x_2 = \frac{V_2(t)}{V_{sat}}$, $x_{2_\tau} = \frac{V_{2_{T_D}}}{V_{sat}}$, $\overline{X} = \frac{\overline{V(t)}}{V_{sat}}$, $n_1 = \frac{R_5}{R_4}$, $m_1 = \beta\frac{R_5}{R_3}$, $l_1 = \omega\frac{R_2}{R_1}$, $b = \frac{R_7}{R_6}$, $\gamma = \frac{R_{10}}{R_8} = 1$, $\varepsilon = \frac{R_{10}}{R_9}$, and $Q = \frac{R_Q}{R}$. With these, Eq. (5.25) reduces to the following dimensionless form:

$$\frac{dx_1}{dt} = -x_1(t) - bf\left(x_{1_\tau}\right) + \varepsilon(Q\overline{X} - x_1), \tag{5.26a}$$

$$\frac{dx_2}{dt} = -x_2(t) - bf\left(x_{2_\tau}\right) + \varepsilon(Q\overline{X} - x_2), \tag{5.26b}$$

with

$$f(v_\tau) \equiv -0.5n_1(|v_\tau| + v_\tau) + m_1 \tanh(l_1 v_\tau), \tag{5.27}$$

where $v \equiv x_1, x_2$. Thus, Eq. (5.26) (with (5.27)) is equivalent to Eq. (5.1) (with (5.19) and (5.20)) with $a = 1$ and proper choice of n_1, m_1, and l_1.

In the experiment, the following component values are used: $R_1 = 10$ kΩ, $R_2 = 18.55$ kΩ, $R_3 = 18.55$ kΩ, $R_4 = 5.6$ kΩ, $R_5 = 10$ kΩ, $R_6 = 1$ kΩ, $R_8 = R_{10} = 1$ kΩ. In the coupling part of Fig. 5.7, $R = 10$ kΩ. The low-pass sections have $R_0 = 1$ kΩ and $C_0 = 0.1$ μF. The APF section of Fig. 2.13 (p. 26) has $R_{11} = R_{12} = 2.2$ kΩ, $C = 10$ nF, and $R_D = 10$ kΩ. All the op-amps are TL074 IC (quad JFET op-amp) with ±15 volt power supply. The resistors (capacitors) have 5% (1%) tolerance. R_9 and R_Q are varied with precession potentiometers (POT). With these values, the experimental nonlinearity is shown in Fig. 2.26, which is same for both the systems. To drive the systems into hyperchaotic zone, we use $\tau_{1,2} \geq 3$, and $b_1 = b_2 = 2.4$ by setting $R_7 = 2.4$ kΩ.

5.4.1 *Effect of Intrinsic Time Delay*

To demonstrate the effect of variation of intrinsic time delay for a fixed coupling strength, we set $R_9 = 139$ Ω, $R_Q = 8.76$ kΩ and $\tau_1 = 6$, and vary τ_2. Figure 5.8 shows the snapshots of the experimental results [using Tektronix TDS2002B, 60 MHz, 1 Gs/s DSO]: It shows a transition from AD (Fig. 5.8a) to GAS ($\tau_2 = 5$) (Fig. 5.8b) to CS ($\tau_2 = 6$) (Fig. 5.8c) to GLS ($\tau_2 = 7$) (Fig. 5.8d), and again to AD (Fig. 5.8e). It can be seen from Fig. 5.8b that the x_2-system [dark gray(blue) trace] leads the x_1-system [light gray(orange) trace], and at the same time the waveform of V_2 differs from that of V_1, both indicate the occurrence of GAS. Figure 5.8d shows

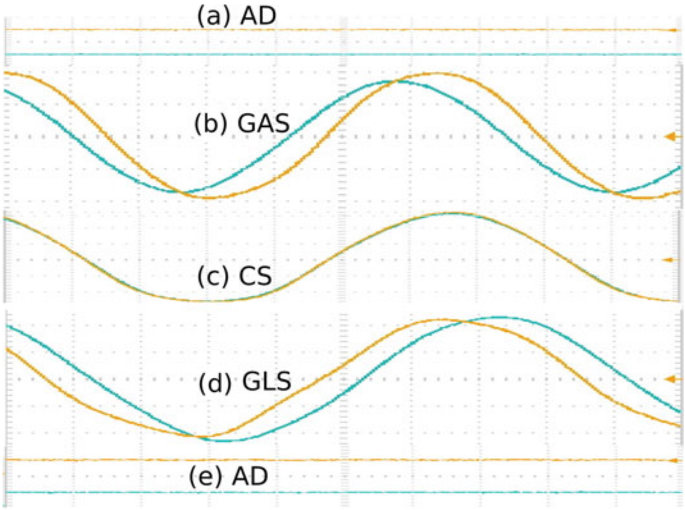

Fig. 5.8 Experimental demonstration of transitions among: **a** AD ($\tau_2 = 4$), **b** GAS ($\tau_2 = 5$), **c** CS ($\tau_2 = 6$), **d** GLS ($\tau_2 = 7$), **e** AD ($\tau_2 = 8$). $R_9 = 139\ \Omega$, $R_Q = 8.76$ kΩ, and $\tau_1 = 6$. V_1-system (light gray(orange) trace), V_2-system (dark gray(blue) trace). (Scale div: x-axis: 12 µs/div, y-axis:1.25 volt/div). The traces of $V_2(t)$ in **a** and **e** shifted downwards by 1.2 V from that of $V_1(t)$

the case of GLS; here V_2 lags behind V_1, and waveform of V_2 and V_1 are different, which is in accordance with the numerical results (Fig. 5.2). We also observe GAS and GLS in the hyperchaotic zone keeping proper values of R_9 and R_Q (not shown here), which indicates that these phenomena are general.

5.4.2 Effect of Coupling

We set $\tau_1 = \tau_2 = 3$ and vary ε by varying R_9 and keep Q fixed by fixing $R_Q = 7.5$ kΩ. The results of this variation are shown in Fig. 5.9. For $R_9 = 10.77$ kΩ, the scenario is shown in the first row a(1–3) of Fig. 5.9; (a1) shows the hyperchaotic attractor, and (a2) and (a3) show that there is no correlation between the coupled systems for these parameter values, and both the systems evolve independently. For $R_9 = 862\ \Omega$, one can observe in-phase synchronization (Fig. 5.9b1–b3). The third row (c(1–3)) shows the complete synchrony for $R_9 = 120\ \Omega$. Period-2 (fourth row d(1–3)) and Period-1 oscillations (fifth row e(1–3)) are shown for $R_9 = 86\ \Omega$ and $R_9 = 30\ \Omega$, respectively. At very low coupling resistance (i.e., high value of ε), the coupled systems show amplitude death (AD); Fig. 5.9f2 shows the waveforms for $R_9 = 15\ \Omega$ that indicates the occurrence of AD, i.e., now the oscillations in both the systems die out. $P_1(t)$ and $P_2(t)$ defined by Eq. (5.22) is computed from the experimental time series data (acquired using DSO, Tektronix TDS2002B, 60 MHz, 1 GS/s) ($\varepsilon_t = 0.01$, and $N_1 = 2400$). Figure 5.10a shows $P(t)$s for the unsynchronized

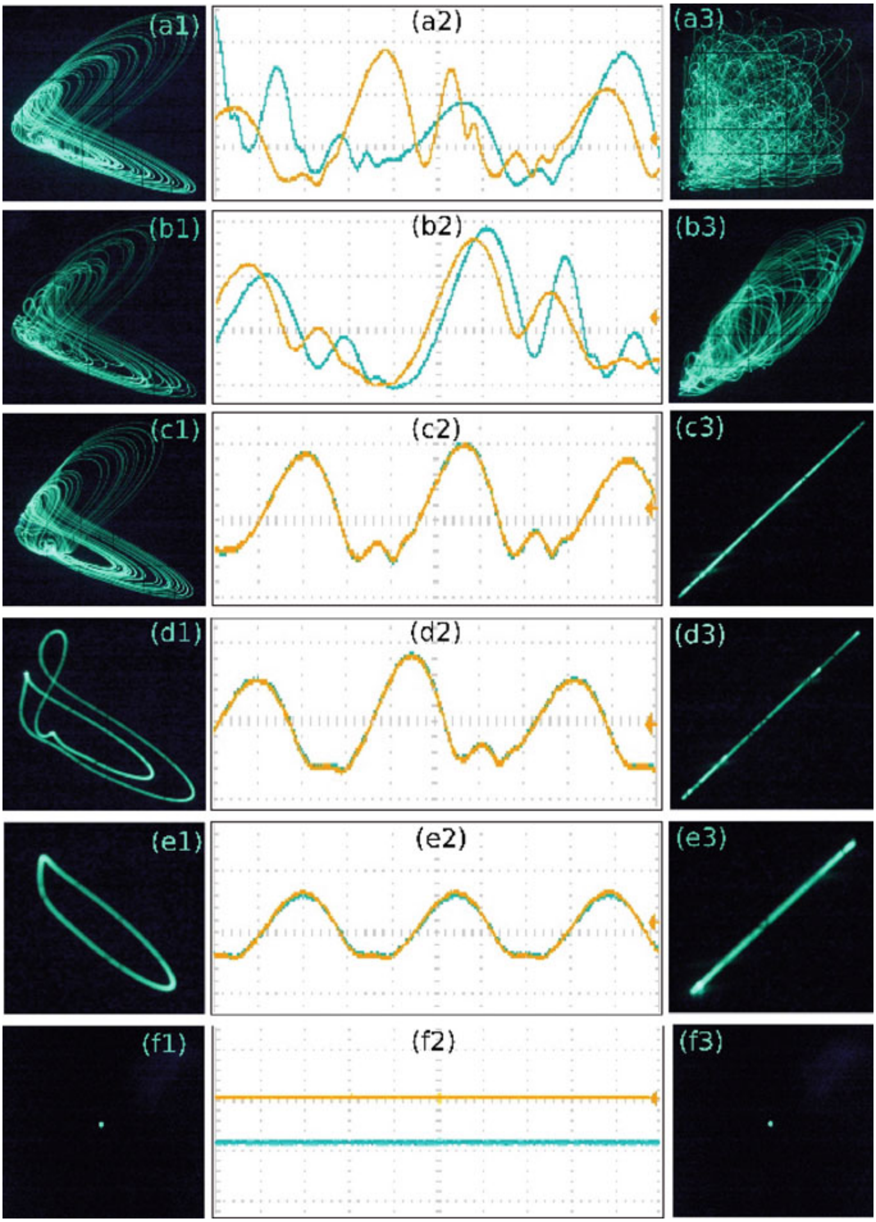

Fig. 5.9 Experimental waveforms and phase-plane plots with fixed Q ($R_Q = 7.5\,\mathrm{k}\Omega$) and variable ε. The left column shows the phase-plane plots $(V_1(t) - V_1(t - T_D))$, the middle column shows the real-time waveforms of $V_1(t)$- (yellow) and $V_2(t)$-(blue), and the right column shows the phase-plane plots in $(V_1(t) - V_2(t))$ plane. **a**(1–3) The unsynchronized state; **b**(1–3) in-phase synchronization; **c**(1–3) complete synchronization; **d**(1–3) period-2 oscillation; **e**(1–3) period-1 oscillation, and **f**(1–3) show AD; in (f2) the trace of $V_2(t)$ (blue) is shifted downward by 1.2 volt from that of $V_1(t)$ (yellow trace). (For the parameter values see text; Scale div: Second column (a2–f2): x-axis: 25 μs/div, y-axis:1.25 volt/div. Other plots: x and y-axes: 0.5 v/div)

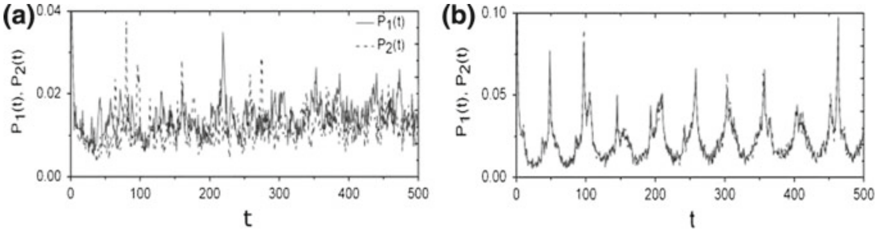

Fig. 5.10 Plots of generalized autocorrelation functions using the experimental time series data (**a**) unsynchronized state (parameters are the same as Fig. 5.9a1–a3), **b** in-phase synchronized state (parameters are the same as Fig. 5.9b1–b3)

case, which shows that peaks of $P_1(t)$ does not match with that of $P_2(t)$ in the t-axis, indicating unsynchronized states. Figure 5.10b is for the in-phase synchronization; here the dominant peaks of $P_1(t)$ and $P_2(t)$ match exactly in the t-axis.

5.5 Summary

In this chapter, we have explored the phenomena of amplitude death and the related synchronization transitions leading to amplitude death in intrinsic time delay hyperchaotic oscillators coupled through mean-field diffusion. We have identified two types of synchronization transitions that lead to amplitude death (AD): (i) a novel transition scenario, namely the transitions among AD, generalized (anticipatory, lag) (GAS, GLS) and complete synchronization (CS); *this transition is mediated by the variation of the difference of the intrinsic time delays* and has no analog in coupled low-dimensional systems (with or without coupling delay). (ii) Transition to the amplitude death state from an unsynchronized state via in-phase (complete) synchronized states. This transition is mediated by the coupling parameters (with the coupled systems having equal intrinsic time delays).

We have derived a stability condition for the GAS, GLS, and CS cases using Krasovskii–Lyapunov theory; also, stability analysis has been carried out to predict the zone of AD in the parameter space. We have exemplified our results numerically using a prototype hyperchaotic oscillator with intrinsic time delay. Through the modified similarity function, LE spectrum, correlation functions, and eigenvalue spectrum, we have identified the zone of GAS, GLS, CS, and amplitude death in the parameter space. It has been found that numerical results agree well with the analytical derivations. The eigenvalue spectrum of the coupled systems revealed that, in the present system, the route to amplitude death is through Hopf bifurcation. Through the transient dynamics and the Lyapunov exponent spectrum, it has been shown that, unlike systems with *coupling time delay*, the variation of *intrinsic time delay* does not induce *phase-flip transition*, but results in transitions among GAS, CS, and GLS. Finally, we set an experiment using electronic circuit to demonstrate all the transition scenarios and amplitude death. It has been observed that the experimental results qualitatively agree well with the analytical results and numerical observations. The present study can be extended to the network of mean-field coupled time-delayed systems with distributed intrinsic time delays, that may reveal the phenomena of GAS and GLS in a more general way.

Chapter 6
Epilogue: Future Directions

Dynamics of nonlinear time-delayed systems is a broad subject. In this brief, we only covered two specific topics: design of time-delayed chaos generators and their collective behaviors. In the following, we discuss few topics that are of immense importance and should govern the future research in nonlinear time-delayed systems.

6.1 Studies on Systems Having Distributed Time Delay

In this brief, we have discussed the scalar time-delayed systems having discrete and single time delay: this only represents a special class. However, there also exist systems and processes that possess *distributed time delay*. Examples include the time lag phenomenon in thermodynamics, transmission line, ecology, and epidemiology (see Refs. [49, 54] for details). Unlike discrete delay, exploring the dynamics of distributed time-delayed systems is a challenging problem for the researchers. Moreover, implementation of these systems in electronic circuits is itself an open engineering problem and should be studied in details.

6.2 Collective Behavior: Chimera States

The chimera state is an intriguing and counterintuitive spatiotemporal state that has been in the center of intensive research over the past decade [91, 113]. In this state, a network of coupled identical oscillators spontaneously splits into two incongruous domains: in one domain the neighboring oscillators are synchronized, whereas in another domain the oscillators are desynchronized. The chimera state was discovered by Kuramoto and Battogtokh [67] in 2002 in phase oscillators. Later, Strogatz and his

D. Biswas and T. Banerjee, *Time-Delayed Chaotic Dynamical Systems*, SpringerBriefs in Nonlinear Circuits,
https://doi.org/10.1007/978-3-319-70993-2_6

group [2, 3] provided the analytical proof of the occurrence of chimera in identical phase oscillators. The name "chimera" was coined by Strogatz [3] considering the fact that in the Greek mythology chimera is a fire-breathing animal that contains the incongruous parts of a goat, a lion, and a snake. Later on, several chimera patterns have been discovered where, in contrast to the chimera state in phase oscillators, not only phase but also amplitude contributes to the spatiotemporal behavior [9, 121, 152]. Recent experimental observation of chimera states has established their robustness in natural and man-made systems. The first experimental observation of chimeras was reported in optical systems [51] and chemical oscillators [137]. A continuous effort is on to observe new kind of chimeras: for example, the coherence resonance chimera in excitable systems [116] and imperfect traveling chimera [19] discovered a novel chimera state. Several chimera patterns have been found in models from ecology [32], neuronal systems [19], SQUID metamaterials, and quantum systems [18] showing their omnipresence in the macroscopic as well as in the microscopic world. In this context, however, a systematic observation of chimeras in intrinsic time-delayed systems and their detailed characterizations are not well explored. Therefore, studies on chimera in networks of time-delayed systems appear to be a potential research problem in the coming years.

6.3 Collective Behavior: Symmetry Breaking Oscillation Quenching States

Oscillation quenching is an emergent and intriguing phenomenon that has been the topic of extensive research in diverse fields like physics, biology, and engineering [63, 112]. There exist two distinct types of oscillation quenching processes: amplitude death (AD) and oscillation death (OD). As discussed in Chap. 5, in the case of AD, the coupled oscillators come to a common stable steady state which was unstable otherwise and thus forms a stable homogeneous steady state (HSS). On the other hand, in the case of OD, coupling breaks the symmetry of the system and oscillators populate different coupling-dependent steady states and thus gives rise to stable inhomogeneous steady states (IHSS); in the phase space, OD may coexist with limit cycle oscillations. AD is important in the case of control applications where suppression of unwanted oscillations is necessary, e.g., in laser and neuronal systems. On the other hand, OD is a much more complex phenomenon because it induces inhomogeneity in a rather homogeneous system of oscillators that has strong connections and importance in the field of biology (e.g., synthetic genetic oscillator, cellular differentiation) and physics (see Ref. [63] and references therein). However, although the OD phenomenon in intrinsic time-delayed systems is of much importance, it has been largely ignored in the literature. Therefore, study on symmetry breaking oscillation quenching states (OD) in time-delayed systems is a potential problem for researchers.

Appendix A
A Brief Tutorial on XPPAUT and LabVIEW

A.1 Solving DDE Using XPPAUT

XPPAUT is an open-source numerical tool for simulating, analyzing, and animating dynamical systems developed by Bard Ermentrout [35]. It contains a number of integrators in it. The package is much flexible to use and faster than the conventional commercial software packages. A few lines of code works for integrating dynamical systems. Another great aspect of XPPAUT is that it provides a very “user-friendly” interface of the bifurcation package AUTO. The installation of the package in different OS environments, like Linux, Windows, MacOS, is supported. The source code of the package is freely available and may be downloaded from the website “http://www.math.pitt.edu/~bard/xpp/xpp.html”. Here, we provide a simple example of how to integrate delay differential equations (DDEs) in XPPAUT.

In the present example, we discuss the integration of the time-delayed system given in Eqs. (2.1) and (2.2) in Chap. 2 (p. 11), which reads the following form

$$\dot{x} = -ax(t) + b\big[-nx(t-\tau) + m\tanh\big(lx(t-\tau)\big)\big], \tag{A.1}$$

where $a > 0$, b, n, m, and l are constants. τ is the positive time delay. All we need is to write an ODE file. The time-delayed system Eq. (A.1) is implemented in the `delay.ode` as follows:

```
#delay.ode
par a = 1, b = 1, n = 2.2, m = 1, l = 10, tau = 4
f(x) = -n*x + m*tanh(l*x)
x' = -a*x + bf(delay(x, tau))
aux xt = delay(x, tau)
x(0) = 0.9
@ delay = 20
@ dt = 0.01
@ total = 1000, maxstor = 1000000, trans = 700
done
```

D. Biswas and T. Banerjee, *Time-Delayed Chaotic Dynamical Systems*, SpringerBriefs in Nonlinear Circuits,
https://doi.org/10.1007/978-3-319-70993-2

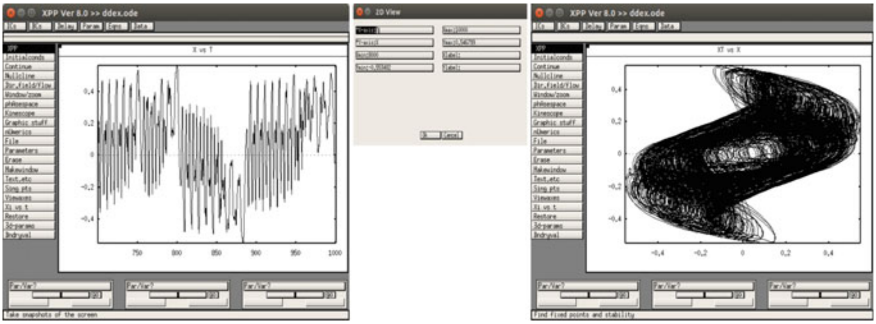

Fig. A.1 (Left Panel)The main window of XPPAUT; (Middle Panel) Window to specify phase-plane plot; (Right Panel) The main window of XPPAUT showing phase-plane plot

The first line starts with the # sign, implies the comment in the ODE file. XPPAUT does not read the line starting with #. The second line starting with `par` tells XPPAUT about the parameters appearing in the system and their respective values (there should be no space between "=" sign and parameters, because XPPAUT considers space as delimiter, thus `a = 1`, not `a = 1`). The third line is a definition of the function occurring in the system. The fourth line defines the system equation. Here, the delay in x is written by the command `delay(x,tau)`. The fifth line tells XPPAUT to store the variable $x(t-\tau)$, i.e., the delayed variable as auxiliary in `xt` variable (for phase-plane plotting). The sixth line indicates the history function; here we consider constant value for it. The sign `@` is a directive that sets some options in XPPAUT. Here at the seventh line, the command `@ delay = 20` defines the maximum delay allowed in the integration. In the eighth line, `@ dt = 0.01`, sets the time step of integration to 0.01. The ninth line specifies total time through the command `@ total = 1000`, i.e., XPPAUT integrates up to time 1000. In the same line, the command `(@) maxstor = 1000000` is a special command and a very useful one. Generally, XPPAUT allocates storage to hold 5000 time points. With the command `(@) maxstor = 1000000`, we fixed it to store 1000000 time points. The command `(@) trans = 700` here indicates XPPAUT to leave 700 times as transients. Finally, the ending command `done` tells XPPAUT that the end of programming has occurred. Running the program by the command `xppaut delay.ode` and clicking `Initialconds, Go (IG)` followed by `Window, Fit (WF)`, we get the following window which shows the time series of the system from the time left after transients to the maximum time specified in the ODE file and shown in Fig. A.1 (left panel).

To see the phase space diagram in $x - x(t-\tau)$ plane click `Viewmap, 2-D (V2)` then a window shown in Fig. A.1 (middle panel) appears. Here, the `x-axis` is assigned `T` and the `y-axis` as `x` by default. Replace `x-axis: x` and `y-axis: xt` (which is stored as auxiliary) then click `OK`. In the main window type, `WF` and the phase space of Fig. A.1 (right panel) is obtained. For more advanced and full references and examples, readers are suggested to consult the book by Bard Ermentrout [35].

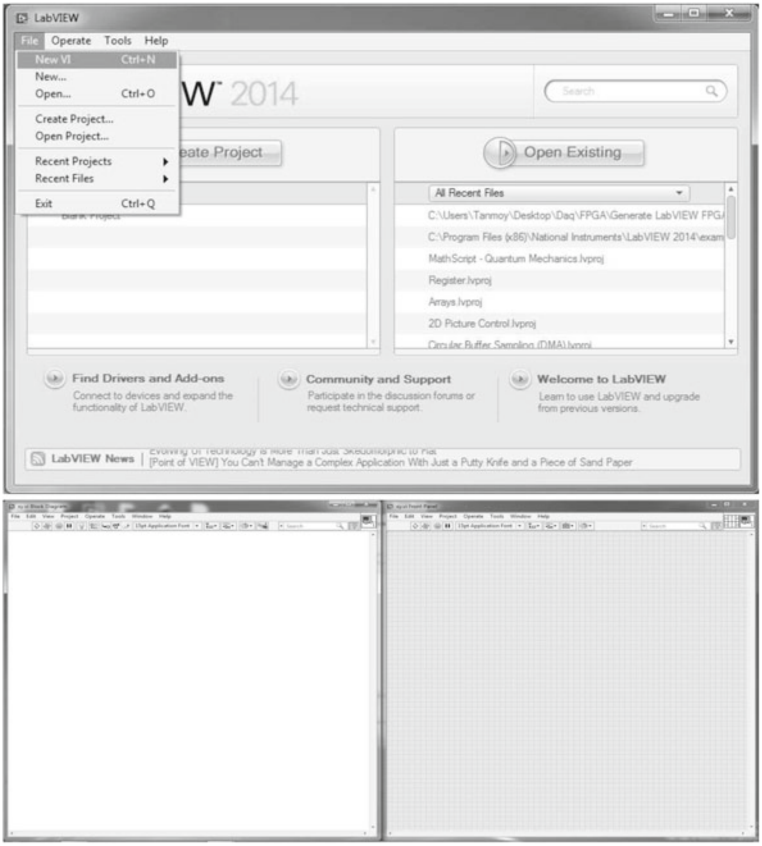

Fig. A.2 (Upper panel) The main window of LabVIEW, (Lower left panel) Virtual Instruments (VI) window, (Lower right panel) Front panel of VI

A.2 Data Acquisition Using LabVIEW

LabVIEW or Laboratory Virtual Instrument Engineering Workbench is a visual programming language for system design platform and development environment [69] developed by National Instruments. LabVIEW is mainly used for data acquisition, control of instruments, and industrial automation. We discuss some basic features of LabVIEW as data acquisition environment that has been used in this book. We show an example to collect data from an external signal source or circuit and display the time series in the computer screen. The required environment is LabVIEW along with hardware data acquisition system (DAQ).

1. First of all, connect the data acquisition (DAQ) system to computer through a USB cable and connect the external signal source (maybe signal generator or any experimental circuit) to DAQ. Then open the LabVIEW software: it will

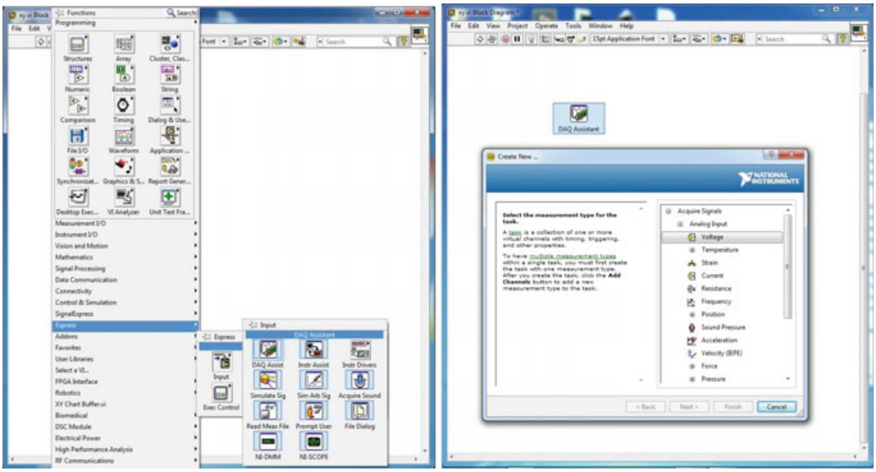

Select the measurement type for the task.

A task is a collection of one or more virtual channels with timing, triggering, and other properties.

To have multiple measurement types within a single task, you must first create the task with one measurement type. After you create the task, click the **Add Channels** button to add a new measurement type to the task.

Fig. A.3 Block Diagram VI

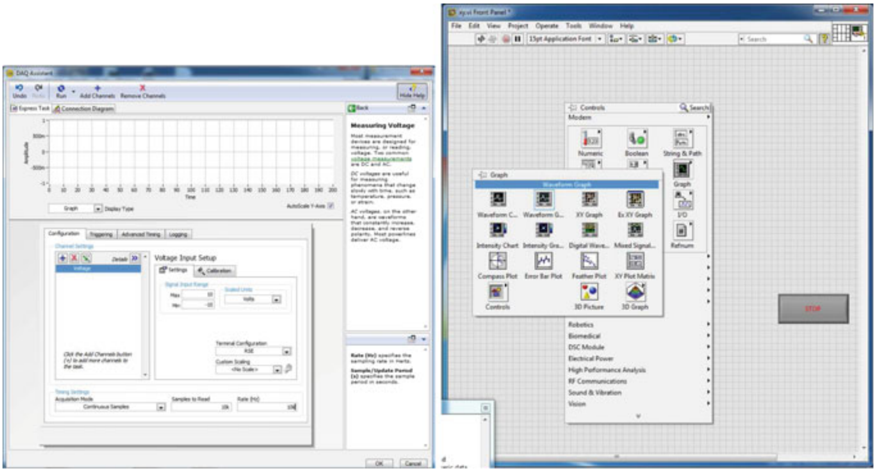

Measuring Voltage

Most measurement devices are designed for measuring, or reading, voltage. Two common voltage measurements are DC and AC.

DC voltages are useful for measuring phenomena that change slowly with time, such as temperature, pressure, or strain.

AC voltages, on the other hand, are waveforms that constantly increase, decrease, and reverse polarity. Most powerlines deliver AC voltage.

Rate (Hz) specifies the sampling rate in Hertz.

Sample/Update Period (s) specifies the sample period in seconds.

Fig. A.4 (Left) DAQ Assistant options window, (Right) Front panel window

create a window shown in Fig. A.2 (upper panel). Now select `File, New VI`. This will open two windows as shown in Fig. A.2 (lower panels): the block diagram window (lower left panel) where block diagrams of the user interface (UI) program elements are arranged and the front panel window (lower right panel), which displays graphs and other processed outputs.

2. To program in LabVIEW, one should use the block diagram window. Right click in block diagram window opens a tray. Here, select `Express, Input, DAQ Assist` as shown if Fig. A.3 (left panel). Selection of this creates an icon `DAQ Assist` in the block diagram window Fig. A.3 (right panel). Also, it opens a

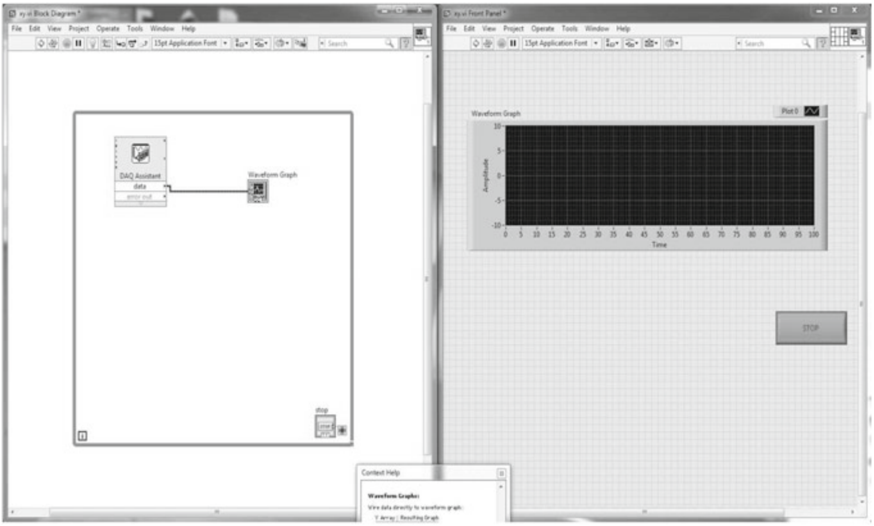

Fig. A.5 (Left panel) Block diagram in VI, (Right panel) Front panel of LabVIEW

sub-window to customize the DAQ Assist (Fig. A.3 (right panel)). Select `Acquire Signals, Analog Input, Voltage` and select the "Supported Physical Channels" to `ai0` (say) and click `Finish`. This opens another window shown in Fig. A.4 (left panel). In this window select `Terminal Configuration` to `RSE`. Select `Acquisition Mode` to `Continuous Samples`. `Samples to Read` to `10k` (say) and `Rate(Hz)` to `1k` (say). Then click `OK`. This asks to use a while loop in the block diagram window. Select `Yes`. This creates a while loop in the block diagram with a stop icon. The "stop" button is created in front panel. Resize it as required and drag it to desired position in the front panel.

3. We want to visualize the signal. This can be achieved in the front panel. To do this right click in the front panel window and select `Graph, Waveform Graph` (see Fig. A.4 (right panel)). This creates a graph in the front panel and an graph icon in the block diagram. Connect the icon to the DAQ Assist with spool wire in the block diagram window (see Fig. A.5 (left panel)).
4. Now connect the output from circuit or signal source to the input port `ai0` of the DAQ system. In any of the window, click arrow sign on the upper left side to run the acquisition. The acquisition of experimental time series is shown in Fig. 3.9 (Chap. 3, p. 50), it also shows the phase-plane plot and FFT of the acquired signal. Also, we can control some of the parameters through controlling the voltage level from LabVIEW.

References

1. G. Ablay, Novel chaotic delay systems and electronic circuit solutions. Nonlinear Dyn. **81**, 1795–1804 (2015)
2. D.M. Abrams, R. Mirollo, S.H. Strogatz, D.A. Wiley, Solvable model for chimera states of coupled oscillators. Phys. Rev. Lett. **101**, 084103 (2008)
3. D.M. Abrams, S.H. Strogatz, Chimera states for coupled oscillators. Phys. Rev. Lett. **93**, 174102 (2004)
4. P. Amil, C. Cebeza, and A. C. Martí. Exact discrete-time implementation of the mackeyglass delayed model. IEEE Trans. Circuits Syst. II Express Briefs **62** (2015)
5. B. Ando, S. Graziani, *Stochastic Resonance: Theory and Applications* (Kluwer, Norwell, 2000)
6. P.K. Asea, P.J. Zak, Time-to-build and cycles. J. Econ. Dyn. Control **23**(8), 1155 (1999)
7. F. Atay (Ed.), *Complex Time-Delay Systems: Theory and Applications*. Springer (2010)
8. A.G. Balanov, N.B. Janson, E. Schöll, Delayed feedback control of chaos: Bifurcation analysis. Phys. Rev. E **71**, 016222 (2005)
9. T. Banerjee, Mean-field-diffusion-induced chimera death state. EPL **110**, 60003 (2015)
10. T. Banerjee, D. Biswas, Amplitude death and synchronized states in nonlinear time-delay systems coupled through mean-field diffusion. Chaos **23**, 043101 (2013)
11. T. Banerjee, D. Biswas, Synchronization in hyperchaotic time-delayed electronic oscillators coupled indirectly via a common environment. Nonlin. Dyn. **73**, 2025–2048 (2013)
12. T. Banerjee, D. Biswas, Theory and experiment of a first-order chaotic delay dynamical system. Int. J. Bifur. Chaos **23**(6), 1330020 (2013)
13. T. Banerjee, D. Biswas, B. Sarkar, Design and analysis of a first order time-delayed chaotic system. Nonlinear Dyn. **70**, 721–734 (2012)
14. T. Banerjee, D. Biswas, B.C. Sarkar, Complete and generalized synchronization of chaos and hyperchaos in a coupled first-order time-delayed system. Nonlinear Dyn. **71**, 279–290 (2013)
15. T. Banerjee, D. Ghosh, Experimental observation of a transition from amplitude to oscillation death in coupled oscillators. Phys. Rev. E **89**, 062902 (2014)
16. T. Banerjee, D. Ghosh, Transition from amplitude to oscillation death under mean-field diffusive coupling. Phys. Rev. E **89**, 052912 (2014)
17. K. Bar-Eli, On the stability of coupled chemical oscillators. Phys. D Nonlinear Phenom. **14**(2), 242–252 (1985)
18. V.M. Bastidas, I. Omelchenko, A. Zakharova, E. Schöll, T. Brandes, Quantum signatures of chimera states. Phys. Rev. E **92**, 062924 (2015)
19. B.K. Bera, D. Ghosh, T. Banerjee, Imperfect traveling chimera states induced by local synaptic gradient coupling. Phys. Rev. E **94**, 012215 (2016)
20. D. Biswas, T. Banerjee, A simple chaotic and hyperchaotic time-delay system: design and electronic circuit implementation. Nonlinear Dyn. **83**, 2331–2347 (2016)

D. Biswas and T. Banerjee, *Time-Delayed Chaotic Dynamical Systems*, SpringerBriefs in Nonlinear Circuits,
https://doi.org/10.1007/978-3-319-70993-2

21. D. Biswas, B. Karmakar, T. Banerjee, A hyperchaotic time-delayed system with single-humped nonlinearity: theory and experiment. Nonlinear Dyn., 1–11 (2017). https://doi.org/10.1007/s11071-017-3548-4
22. I. Boutle, R.H.S. Taylor, R.A. Romer, El niño and the delayed action oscillator. Am. J. Phys. **75**, 15–24 (2007)
23. D. Breda, S. Maset, and R. Vermiglio, *TRACE-DDE: a Tool for Robust Analysis and Characteristic Equations for Delay Differential Equations*, chap. 13, pp. 147–155. Springer, Heidelberg (2009)
24. N. Buric, N. Vasovic, Oscillation in an excitable system with time-delay. Int. J. Bifur. Chaos **13**, 3483 (2003)
25. A. Buscarino, A. Fortuna, M. Frasca, G. Muscato, Chaos does help motion control. Int. J. Bifur. Chaos **17**, 3577–3581 (2007)
26. A. Buscarino, L. Fortuna, M. Frasca, G. Sciuto, Design of time-delay chaotic electronic circuits. IEEE Trans. Circuits Syst. **I**(58), 21888–1896 (2011)
27. A. Buscarnio, L. Fortuna, M. Frasca, G. Sciuto, Design of time-delayed chaotic electronic circuits. IEEE Trans. Circuits Syst.-I **58**, 1888–1896 (2011)
28. S.A. Campbell, *Time Delays in Neural Systems*, Understanding Complex Systems (Springer-Verlag, Heidelberg, 2007)
29. M. Chen, J. Kurths, Synchronization of time-delayed systems. Phys. Rev. E **76**, 359–366 (2007)
30. Y. Ding, W. Jiang, H. Wang, Delayed feedback control and bifurcation analysis of rossler chaotic system. Nonlinear Dyn. **61**, 707–715 (2010)
31. R.D. Driver, *Ordinary and Delay Differential Equatons* (Springer, New York, 1977)
32. P.S. Dutta, T. Banerjee, Spatial coexistence of synchronized oscillation and death: A chimera-like state. Phys. Rev. E **92**, 042919 (2015)
33. J.P. Eckmann, S.O. Kamphorst, D. Ruelle, Recurrence plots of dynamical systems. Europhys. Lett. **4**, 973 (1987)
34. K. Engelborghs, T. Luzyanina, G. Samaey, DDE-BIFTOOL v. 2.00 user manual: a matlab package for bifurcation analysis of delay differential equations. Technical Report TW-330, Department of Computer Science, K.U. Leuven, Leuven, Belgium (2001)
35. B. Ermentrout, *Simulating, Analyzing, and Animating Dynamical Systems: A Guide to XPPAUT for Researchers and Students* (SIAM, Philadelphia, 2002)
36. G.B. Ermentrout, N. Kopell, Oscillator death in systems of coupled neural oscillators. SIAM J. Appl. Math. **50**, 125–146 (1990)
37. J.D. Farmer, Chaotic attractor of an infinite dimensional dynamical system. Phys. D **4**, 366–393 (1982)
38. R. Figueroa, On the discontinuous second-order deviated dirichlet problem with non-monotone conditions. Math. Nachr. **288**(2–3), 176–184 (2015)
39. J. Fort, V. Mendez, Time-delayed theory of the neolithic transition in europe. Phys. Rev. Lett. **82**, 867 (1999)
40. L. Fortuna, M. Frasca, A. Rizzo, Chaotic pulse position modulation to improve the efficiency of sonar sensors. IEEE Trans. Instrum. Meas. **52**, 1809–1814 (2003)
41. E. Fridman, *Introduction to Time-Delay Systems*. Birkhauser (2014)
42. J. García-Ojalvo, M.B. Elowitz, S.H. Strogatz, Modeling a synthetic multicellular clock: repressilators coupled by quorum sensing. Proc. Natl. Acad. Sci. USA **101**, 10955 (2004)
43. J. García-Ojalvo, M.B. Elowitz, S.H. Strogatz, Modeling a synthetic multicellular clock: repressilators coupled by quorum sensing. Proc. Natl. Acad. Sci. USA **101**, 10955 (2004)
44. D. Ghosh, Generalized projective synchronization in time-delayed systems: nonlinear observerapproach. Chaos **19**, 013102 (2009). https://doi.org/10.1063/1.3054711
45. D. Ghosh, Stability and projective synchronization in multiple delay rössler system. Int. J. Nonlin. Sci. **7**, 207–214 (2009)
46. D. Ghosh, Projective-dual synchronization in delay dynamical systems with time-varying coupling delay. Nonlinear Dyn. **66**(4), 717–730 (2011)

47. D. Ghosh, T. Banerjee, Transitions among the diverse oscillation quenching states induced by the interplay of direct and indirect coupling. Phys. Rev. E **90**, 062908 (2014)
48. D. Ghosh, I. Grosu, S.K. Dana, Design of coupling for synchronization in time-delayed systems. Chaos **22**, 033111 (2012)
49. K. Gu, V.L. Kharitonov, J. Chen, *Stability of Time-Delay Systems* (Birkhäuser, Boston, 2003)
50. I. Gyori, P. Ladas, *Oscillation Theory of Delay Differential Equations with Applications* (Clarendon Press, Oxford, 1991)
51. A.M. Hagerstrom, T.E. Murphy, R. Roy, P. Hövel, I. Omelchenko, E. Schöll, Experimental observation of chimeras in coupled-map lattices. Nat. Phys. **8**, 658–661 (2012)
52. J. Hale, *Theory of Functional Differential Equations* (Springer, New York, 1977)
53. Q. Han, C. Li, J. Huang, Anticipating synchronization of chaotic systems with time delay and parameter mismatch. Chaos **19**, 013104 (2009)
54. Q.-L. Han, A descriptor system approach to robust stability of uncertain neutral systems with discrete and distributed delays. Automatica **40**, 1791–1796 (2004)
55. J.M. Höfener, G.C. Sethia, T. Gross, Amplitude death in networks of delay-coupled delay oscillators. arXiv: 1210.2002v1 (2012)
56. K. Ikeda, H. Daido, O. Akimoto, Optical turbulence: chaotic behaviour of transmitted light from a ring cavity. Phys. Rev. Lett. **45**, 709–712 (1980)
57. K. Ikeda, K. Matsumoto, High dimensional chaotic behavior in systems with time-delayed feedback. Physica D **29**, 223–235 (1987)
58. M. Kalecki, A macroeconomic theory of business cycle. Econometrica **3**, 327 (1935)
59. R. Karnatak, N. Punetha, A. Prasad, R. Ramaswamy, Nature of the phase-flip transition in the synchronized approach to amplitude death. Phy. Rev. E **82**, 046219 (2010)
60. S. Kilinç, M.E. Yalçin, S. Özoguz, Multiscroll chaotic attractors from a hysteresis based time-delay differential equation. Int. J. Bifur. Chaos **20**, 3275–3282 (2010)
61. A. Kim, *Functional Differential Equations*, volume 479 of Mathematics and Its Applications (Springer, Netherlands, 1999), pp. 41–59
62. K. Konishi, K. Senda, H. Kokame, Amplitude death in time-delay nonlinear oscillators coupled by diffusive connections. Phys. Rev. E **78**(5), 056216 (2008)
63. A. Koseska, E. Volkov, J. Kurths, Oscillation quenching mechanisms: amplitude vs oscillation death. Phys. Rep. **531**, 173 (2013)
64. N.N. Krasovskii, *Stability of motion* (Oxford University Press, Stanford, 1963)
65. Y. Kuang, *Delay Differential Equations with Application in Population Dynamics* (Academic Press, New York, 1993)
66. P. Kumar, A. Prasad, R. Ghosh, Stable phase-locking of an external-cavity diode laser subjected to external optical injection. J. Phys. B **41**, 135402 (2008)
67. Y. Kuramoto, D. Battogtokh, Coexistence of coherence and incoherence in nonlocally coupled phase oscillators. Nonlinear Phenom. Complex Syst. **4**, 380–385 (2002)
68. W.H. Kye, M. Choi, M. Kurdoglyan, C.M. Kim, Y.J. Park, Synchronization of chaotic oscillators due to common delay time modulation. Phys. Rev. E **70**, 046211 (2004)
69. labVIEW. National instrument. http://www.ni.com/labview/
70. M. Lakshmanan, D. V. Senthilkumar. *Dynamics of Nonlinear Tine-Delay Systems*. Springer (2010). ISSN-0172-7389
71. L.B. Le, K. Konishi, N. Hara, Design and experimental verification of multiple delay feedback control for time-delay nonlinear oscillators. Nonlinear Dyn. **67**, 1407–1418 (2012)
72. G.A. Leonov, N.V. Kuznetsov, Time-varying linearization and the perron effects. Int. J. Bifur. Chaos **17**(4), 1079–1107 (2007). https://doi.org/10.1142/S0218127407017732
73. S. Lepri, G. Giacomelli, A. Polity, F. Arecchi, High-dimensioanl chaos in delayed dynamical systems. Phys. D **70**, 135–149 (1993)
74. S. Li, X. Liao, C.L.K.W. Wong, Hopf bifurcation of a two-neuron network with different discrete time delays. Int. J. Bifur. Chaos **15**, 1589–1601 (2005)
75. Y. Li, Y. Kuang, Periodic solutions in periodic state-dependent delay equations and population models. Proc. Am. Math. Soc. **130**(5), 1345–1353 (2002)

76. X. Liao, S. Guo, C. Li, Stability and bifurcation analysis in tri-neuron model. Nonlinear Dyn. **49**, 319–345 (2007)
77. H. Lu, Y. He, Z. He, A chaos-generator: analysis of complex dynamics of a cell equation in delayed cellular neural networks. IEEE Trans. Circuits Syst. I Fundam. Theory Appl. **45**, 178–181 (1998)
78. H. Lu, Z. He, Chaotic behavior in first-order autonomous continuous-time systems with delay. IEEE Trans. Circuits Syst. I, Fundam. Theory Appl **43**, 700–702 (1996)
79. M.C. Mackey, L. Glass, Oscillation and chaos in physiological control system. Science **197**, 287–289 (1977)
80. B.P. Mann, T. Insperger, P.V. Bayly, G. Stépán, Stability of up-milling and down-milling, part 1 and part 2: experimental verification. Int. J. Machine Tools Manufacture **43**(1), 35–40 (2003)
81. N. Marwan, M.C. Romano, M. Thiel, J. Kurths, Recurrence plots for the analysis of complex systems. Phys. Rep. **438**, 237 (2007)
82. C. Masoller, Anticipation in the synchronization of chaotic semiconductor lasers with optical feedback. Phys. Rev. Lett **86**, 2782–2785 (2001)
83. C. Masoller, Anticipation in the synchronization of chaotic time-delay systems. Phys. A **295**, 301–304 (2001)
84. C. Masoller, D.H. Zanette, Anticipated synchronization in coupled chaotic maps with delays. Phys. A **300**, 359–366 (2001)
85. J. Meng, X. Wang, Robust anti-synchronization of a class of delayed chaotic neural networks. Chaos **17**, 023113 (2007)
86. C.-I. Morărescu, S.-I. Niculesdu, K. Gu, Stability crossing curves of shifted gamma-distributed delay systems. (unpublished)
87. G. Mykolaitis, A. Tamaševičius, A. Čenys, S. Bumeliené, A. Anagnostopoulos, N. Kalkan, Very high and ultrahigh frequency hyperchaotic oscillators with delay line. Chaos Solitons Fractals **17**, 343 (2003)
88. H. Nakajima, On analytical properties of delayed feedback control of chaos. Phys. Lett. A **232**, 207–210 (1997)
89. A. Namajunas, K. Pyragas, A. Tamaševičius, An electronic analog of the mackey-glass system. Phys. Lett. A **201**, 42–46 (1995)
90. S. Pal, B. Sahoo, S. Poria, Generalized lag synchronization of delay coupled chaotic systems via linear transformations. Phys. Scr. **87**, 045011 (2013)
91. M.J. Panaggio, D.M. Abrams, Chimera states: coexistence of coherence and incoherence in networks of coupled oscillators. Nonlinearity **28**, R67–R87 (2015)
92. R.K. Pathria, P.D. Beale, *Statistical mechanics* (Butterworth Heinemann third edition, 2011)
93. L. Pecora, T. Carroll, Synchronization in chaotic systems. Phys. Rev. Lett. **64**, 821–824 (1990)
94. L. Pei, Q. Wang, H. Shi, Bifurcation dynamics of the modified physiological model of artificial pancreas with insulin secretion delay. Nonlinear Dyn. **63**, 417–427 (2011)
95. T. Pereira, M. Baptista, J. Kurths, General framework for phase synchronization through localized sets. Phys. Rev. E **75**, 026216 (2007)
96. A.S. Pikovsky, M.G. Rosenblum, J. Kurths, *Synchronization: A Universal Concept in Nonlinear Sciences* (Cambridge University Press, Cambridge, 2001)
97. D. Premraj, K. Suresh, T. Banerjee, K. Thamilmaran, Control of bifurcation-delay of slow passage effect by delayed self-feedback. Chaos **27**, 013104 (2017)
98. K. Pyragas, Transmission of signals via synchronization of chaotic time-delay systems. Int. J. Bifur. Chaos **8**, 1839–1842 (1998)
99. K. Pyragas, Control of chaos via an unstable delayed feedback controller. Phys Rev Lett. **86**, 2265–8 (2001)
100. K. Pyragas, Synchronization of coupled time-delay systems: analytical estimations. Phys. Lett. A **292**, 320–324 (2002)
101. K. Pyragas, Delayed feedback control of chaos. Phil. Trans. R. Soc. A **364**, 2309–2334 (2006)
102. C. Raffel, J. Smith, Practical modeling of bucket-brigadde device circuits, in *13-th International Conference on Digital Audio Effects (DAFx-10)* (2010)

103. J.W.S. Rayleigh, *The Theory of Sound* (Macmillan and Co., London, 1877)
104. D.V.R. Reddy, A. Sen, G.L. Johnston, Time delay induced death in coupled limit cycle oscillators. Phy. Rev. Lett **80**, 5109–5112 (1998)
105. V. Resmi, G. Ambika, General mechanism for amplitude death in coupled systems. Phys. Rev. E **84**, 046212 (2011)
106. V. Resmi, G. Ambika, R. Amritkar, Synchronized states in chaotic systems coupled indirectly through a dynamic environment. Phys. Rev. E **81**, 046216 (2010)
107. R. Rocha, G.L.D. Andrucioli, R.O. Medrano-T, Experimental characterization of nonlinear systems: a real-time evaluation of the analogous chuas circuit behaviour. Nonlinear Dyn. **62**, 237–251 (2010)
108. M.C. Romano, M. Thiel, J. Kurths, I.Z. Kiss, J.L. Hudson, Detection of synchronization for non-phase-coherent and non-stationary data. Europhys. Lett. **71**(3), 466–472 (2005)
109. R. Ross, *The Prevention of Malaria* (John Murray, London, 1911)
110. M.R. Roussel, Delay-differential equations, November 22 2005
111. E. Saad, D. Prokhorov, D. Wunsch, Comparative study of stock trend prediction using time delay, recurrent and probabilistic neural networks. IEEE Trans. Neural Netw. **9**(6), 1456–1470 (1998)
112. G. Saxena, A. Prasad, R. Ramaswamy, Amplitude death: the emergence of stationarity in coupled nonlinear systems. Phys. Rep. **521**, 205–228 (2012)
113. E. Schöll, Synchronization patterns and chimera states in complex networks: interplay of topology and dynamics. Eur. Phys. J. Special Topics **225**, 891 (2016)
114. E. Schöll, H.G. Schuster, *Handbook of Chaos Control* (Wiley-VCH, Berlin, 2008)
115. A.S. Sedra, K.C. Smith, *Microelectronic Circuits* (Oxford University Press, Oxford, 2003)
116. N. Semenova, A. Zakharova, V. Anishchenko, E. Schöll, Coherence-resonance chimeras in a network of excitable elements. Phys. Rev. Lett. **117**, 014102 (2016)
117. D.V. Senthilkumar, J. Kurths, Characteristics and synchronization of time-delay systems driven by a common noise. Eur. Phys. J. Special Topics **187**, 87–93 (2010)
118. D.V. Senthilkumar, J. Kurths, M. Lakshmanan, Inverse synchronizations in coupled time-delay systems with inhibitory coupling. Chaos **19**, 023107 (2009)
119. D.V. Senthilkumar, M. Lakshmanan, J. Kurths, Phase synchronization in unidirectionally coupled ikeda time-delay systems. Eur. Phys. J. Special Topics **164**, 35–44 (2008)
120. D.V. Senthilkumar, M. Lakshmanan, J. Kurths, Phase synchronization in time-delay systems. Phys. Rev. E **74**, 035205R (2006)
121. G.C. Sethia, A. Sen, G.L. Johnston, Amplitude-mediated chimera states. Phys. Rev. E **88**, 042917 (2013)
122. E.M. Shahverdiev, Synchronization in systems with multiple time delays. Phys. Rev. E **70**, 067202 (2004)
123. E.M. Shahverdiev, S. Sivaprakasam, K. Shore, Lag synchronization in time-delayed systems. Phys. Rev. E **58**, 3067–3071 (1998)
124. A. Sharma, M.D. Shrimali, Amplitude death with mean-field diffusion. Phys. Rev. E **85**, 057204 (2012)
125. A. Sharma, M.D. Srimali, S.K. Dana, Phase-flip transition in nonlinear oscillators coupled by dynamic environment. Chaos **22**, 023147 (2012)
126. L. Shayer, S. Campbell, Stability, bifurcation, and multistability in a system of two coupled neurons with multiple time delays. SIAM J. Appl. Math. **61**, 673 (2000)
127. M. Shiino, M. Frankowicz, Synchronization in infinitely many coupled limit-cycle type oscillators. Phys. Lett. A **136**, 103 (1989)
128. J.C. Sprott, A simple chaotic delay differential equation. Phys. Lett. A **366**, 397–402 (2007)
129. S.B. Stojanovic, D.L. Debeljkovic, Simple stability conditions of linear discrete-time systems with multiple delay. Serbian J. Elect. Eng. **7**(1), 69–79 (2010)
130. W. Sun, S. Zhang, Existence and approximation of solutions for discontinuous functional differential equations. E. J. Math. Anal. Appl. **38**, 307–318 (2002)
131. R. Suresh, D.V. Senthilkumar, M. Lakshmanan, J. Kurths, Global phase synchronization in an array of time-delay systems. Phys. Rev. E **82**, 016215 (2010)

132. R. Suresh, D.V. Senthilkumar, M. Lakshmanan, J. Kurths, Transition to complete synchronization and global intermittent synchronization in an array of time-delay systems. Phys. Rev. E **86**, 016212 (2012)
133. M. Szydlowsky, A. Krawiec, The stability problem in the kaldorkalecki business cycle model. Chaos Solit. Frac. **25**, 299 (2005)
134. A. Tamaševičius, G. Mykolaitis, S. Bumeliene, Delayed feedback chaotic oscillator with improved spectral characteristics. Electron. Lett. **42**, 736–737 (2006)
135. A. Tamaševičius, T. Pyragine, M. Meskauskas, Two scroll attractor in a delay dynamical system. Int. J. Bifur. Chaos **17**, 3455–3460 (2007)
136. Y.C. Tian, F. Gao, Adaptive control of chaotic continuous-time systems with delay. Phys. D **108**, 113 (1997)
137. M.R. Tinsley, S. Nkomo, K. Showalter, Chimera and phase-cluster states in populations of coupled chemical oscillators. Nat. Phys. **8**, 662–665 (2012)
138. C. Tse, Experimental techniques for investigating chaos in electronics, in *Chaos in Circuits and Systems*, chap. 18 (World Scientific, Singapore, 2002)
139. A. Uçar, On the chaotic behaviour of a prototype delayed dynamical system. Chaos Solitons Fractals **16**, 187–194 (2003)
140. M. Villasana, A. Radunskaya, A delay differential equation model for tumor growth. J. Math. Biol. **47**, 270 (2003)
141. H.U. Voss, Anticipating chaotic synchronization. Phys. Rev. E **61**(5), 5115–5119 (2000)
142. C. Wang, K. Yang, S. Qu, Vibrational resonance in a discrete neuronal model with time delay. Int. J. Mod. Phys. B **28**, 1450103 (2014)
143. L. Wang, X. Yang, Generation of multi-scroll delayed chaotic oscillator. Electron. Lett. **42**, 1439–1441 (2006)
144. J. Wei, Bifurcation analysis in a scalar delay differential equation. Nonlinearity **20**, 2483–2498 (2007)
145. M.E. Yalçin, S. Özoguz, n-scroll chaotic attractors from a first-order time-delay differential equation. *Chaos* **17**(3), 033112 (2007)
146. M.E. Yalçin, J.A.K. Suykens, J. Vandewalle, Master-slave synchronization of lur'e with time-delay. Int. J. Bifur. Chaos **11**, 1707–1722 (2001)
147. Y. Yamaguchi, H. Shimizu, Theory of self-synchronization in the presence of native frequency distribution and external noises. Phys. D **11**, 212–226 (1984)
148. Z. Yan, A new scheme to generalized (lag, anticipated, and complete) synchronization in chaotic and hyperchaotic systems. Nonlinear Dyn. **15**, 013101 (2005)
149. C. Yao, M. Yi, J. Shuai, Time delay induced different synchronization patterns in repulsively coupled chaotic oscillators. Chaos **23**, 033116 (2013)
150. P. Yongzhen, L. Shuping, L. Changguo, Effect of delay on a predator-prey model with parasitic infection. Nonlinear Dyn. **63**, 311–321 (2011)
151. Y. Yu, The synchronization for time-delay of linearly bidirectional coupled chaotic system. Chaos Solitons Fractals **33**, 1197–1203 (2007)
152. A. Zakharova, M. Kapeller, E. Schöll, Chimera death: symmetry breaking in dynamical networks. Phy. Rev. Lett **112**, 154101 (2014)
153. X. Zhang, J. Chen, J. Peng, A new family of first-order time-delayed chaotic systems. Int. J. Bifur. Chaos **21**, 2547–2558 (2011)
154. L. Zhu, Y.-C. Lai, Experimental observation of generalized time-lagged chaotic synchronization. Nonlinear Dyn. **64**, 045205 (2001)

Index

D. Biswas and T. Banerjee, *Time-Delayed Chaotic Dynamical Systems*, SpringerBriefs in Nonlinear Circuits,
https://doi.org/10.1007/978-3-319-70993-2